Design and Control of Integrated Systems for Hydrogen Production and Power Generation

A DISSERTATION
SUBMITTED TO THE FACULTY OF THE GRADUATE SCHOOL
OF THE UNIVERSITY OF MINNESOTA
BY

Dimitrios Georgis

IN PARTIAL FULFILLMENT OF THE REQUIREMENTS
FOR THE DEGREE OF
Doctor of Philosophy

Advised by Prodromos Daoutidis

November 2013

Acknowledgments

During my graduate studies at the University of Minnesota I had the opportunity to meet, interact and work with amazing people who have contributed significantly towards my PhD completion. I would like to express my deepest gratitude and appreciation to all these people, therefore, allow me to mention some of them.

First of all, I would like to thank my advisor Professor Prodromos Daoutidis for his constant support during my graduate studies. His widespread knowledge and skills motivated me to pursue a PhD in Process Systems Engineering. Furthermore, I would like to thank Professors Jeffrey Derby, William Smyrl and Mihailo Jovanovic for being part of my PhD committee.

Many thanks to Professor Ali Almansoori for the great collaboration that we had during the ADMIRE project. Moreover, I would like to express my appreciation to all faculty at Petroleum Institute in Abu Dhabi for their hospitality during my visit.

It was a great pleasure working with exceptional colleagues. I would like to thank Dr. Sujit Jogwar, Dr. Ana Torres Rippa, Dr. Srinivas Rangaranjan, Dr. Alex Marvin, Seongmin Heo, Dr. Fernando Lima, Dr. Milana Trifkovic, Adam Kelloway, Abdulla

Malek, Nahla Al Amoodi, Michael Zachar, Mustafa Caglayan and Udit Gupta for the amazing moments we had as a group. In addition to this, I feel the need to thank some former group members of Professor Kumar's group (Dr. Scott Roberts, Dr. Shawn Dodds and Dr. Eric Vandre) with whom we shared the same office during the first years. Furthermore, I would like to thank all the employees in the department for their valuable service. Specifically I am grateful to Julie Prince who was always willing to help and assist me. Moreover, I have to mention that I am grateful to our department's IT team for their important services and fast responses to any questions I had during my PhD.

Many thanks to all the members of Hellenic Student Association (HSA) and the entire Greek community for all the beautiful moments and the nice events. Especially, I am more than grateful to all my friends for all the beautiful moments we had in Minneapolis; thus, making my life here in Minneapolis pleasant, and full of great memories.

Last but not least, I would like to express my appreciation and gratitude to my parents, my brother, my fiancee and my entire family for their unstoppable support, love and faith in everything I have done in my life. I firmly believe that without their support it would be very difficult for me to achieve my goals.

to my family

Abstract

Growing concerns on CO_2 emissions have led to the development of highly efficient power plants. Options for increased energy efficiencies include alternative energy conversion pathways, energy integration and process intensification. Solid oxide fuel cells (SOFC) constitute a promising alternative for power generation since they convert the chemical energy electrochemically directly to electricity. Their high operating temperature shows potential for energy integration with energy intensive units (e.g. steam reforming reactors). Although energy integration is an essential tool for increased efficiencies, it leads to highly complex process schemes with rich dynamic behavior, which are challenging to control. Furthermore, the use of process intensification for increased energy efficiency imposes an additional control challenge.

This dissertation identifies and proposes solutions on design, operational and control challenges of integrated systems for hydrogen production and power generation. Initially, a study on energy integrated SOFC systems is presented. Design alternatives are identified, control strategies are proposed for each alternative and their validity is evaluated under different operational scenarios. The operational range of the proposed

control strategies is also analyzed. Next, thermal management of water gas shift membrane reactors, which are a typical application of process intensification, is considered. Design and operational objectives are identified and a control strategy is proposed employing advanced control algorithms. The performance of the proposed control strategy is evaluated and compared with classical control strategies. Finally SOFC systems for combined heat and power applications are considered. Multiple recycle loops are placed to increase design flexibility. Different operational objectives are identified and a nonlinear optimization problem is formulated. Optimal designs are obtained and their features are discussed and compared.

The results of the dissertation provide a deeper understanding on the design, operational and control challenges of the above systems and can potentially guide further commercialization efforts. In addition to this, the results can be generalized and used for applications from the transportation and residential sector to large–scale power plants.

Contents

List of Tables

List of Figures

CHAPTER 1

Introduction

The extensive use of fossil fuels for power generation for almost a century has evolved into a severe threat for the environment. Recent reports have provided evidence of climate change which is mainly attributed to the increasing anthropogenic greenhouse gas emissions (GHG) in the atmosphere [7, 8]. CO_2 is considered the major GHG emission. Although CO_2 emissions have remained almost constant in the last decade in economically developed countries [8, 9, 10] (mainly due to governmental regulations on greenhouse gas emissions and tax credits for encouraging investments in renewable energy resources), the world's total CO_2 emissions exhibit an increasing trend [7, 10] mainly driven by the emerging economies (e.g. Brazil, India, China). In addition to this, the projected increase in the world's population is expected to result in higher demand for power [11, 12]. It is evident that the CO_2 emissions mitigation and the growing demand for energy constitute major factors of the global energy landscape.

Fossil fuel–based power generation accounts for approximately 85% of the produced energy in US (data refer to 2010 [8]) and 82% of the world's produced energy [13]. Coal and natural gas are mainly used for electricity generation for residential, commercial or industrial usage, while oil derivatives constitute the main energy carrier in the transportation sector. Large–scale conventional power plants suffer from relatively low energy efficiencies as shown in Figure 1.1 since their associated fuel's chemical energy undergoes several transformations to finally generate electricity. Furthermore, their cen-

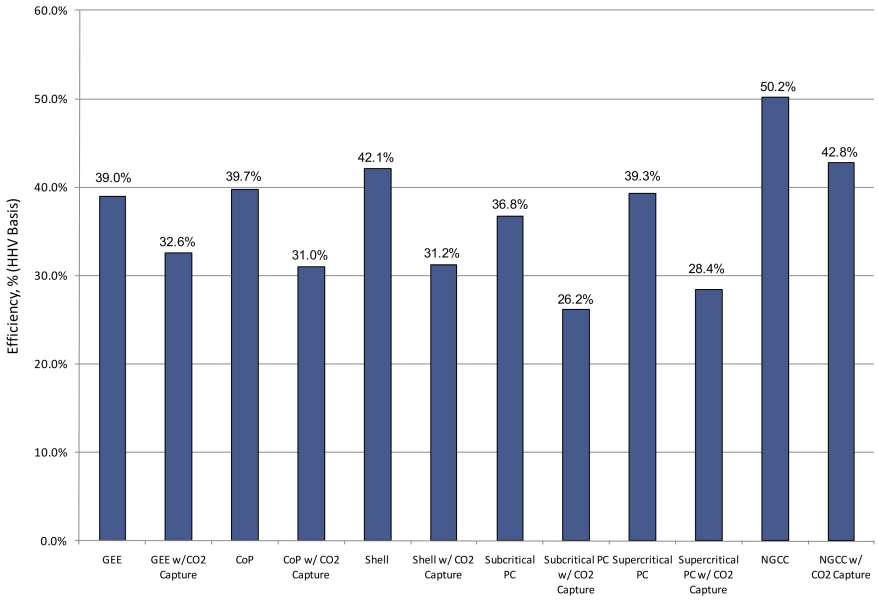

Figure 1.1: Plant efficiencies for coal and natural gas–fired (conventional and integrated with CO_2 capture units) power plants (adopted from DOE–NETL Report [3])

tralized nature requires a high voltage and long transmission grid in order to distribute the electricity to the consumers. Efficiency losses due to the distribution and transmission of electricity in the grid (average of 7% efficiency loss for the U.S according to the U.S Energy Information Administration (EIA) [14]) decrease further the overall energy efficiency. Large–scale conventional power plants also face efficiency challenges due to

variations in power demand (e.g. part–load operation results in significantly lower efficiencies [15]), while high energy demands impose further limitations in the electricity distribution grid. On the other hand, the vast majority of energy in the transportation sector is generated through internal combustion engines with an efficiency of less than 30% [16]. Therefore, future energy systems for power generation should be more efficient and flexible (e.g. allowing for decentralized electricity generation) in order to minimize the environmental impact.

In the following subsections we briefly discuss the main themes of the thesis, providing a broad motivation for the results to be presented.

1.1 Hydrogen: towards carbon–free power generation

Hydrogen has attracted a lot of attention as a potential fuel alternative in power generation. Its zero carbon emission during oxidation makes hydrogen an attractive option for satisfying environmental regulations and mitigating greenhouse gas emissions.

Hydrogen is currently used as a feedstock in the chemical and petrochemical industry [17]. The majority of hydrogen is produced from fossil fuels (e.g. through steam reforming of hydrocarbons) while a small but increasing percentage of hydrogen production is based on renewable energy resources (e.g. biomass, solar) [18, 19]. Despite its advantages, its low mass density at atmospheric conditions requires high pressure compression in order to achieve a proper energy content per unit volume [20]. H_2–fed vehicles are a representative example employing high pressure (e.g. 5000 psi [21]) hydrogen storage in tanks. In addition to this, given the remote location of the H_2 fueling stations and the lack of a well developed hydrogen infrastructure [22], this option results in high capital and operational costs. An alternative option involves the *in–situ* hydrogen production which eliminates any need for storage or transportation [23, 24, 25].

In–situ hydrogen production in energy systems requires an additional process unit to be integrated with the primary power generation unit which is usually referred to as *fuel processor*. Integrated energy systems involving *in–situ* hydrogen production and power generation lead to complex process schemes which are challenging to design, operate and control [24].

1.2 Fuel Cells: an alternative energy conversion unit

Fuel cells are electrochemical devices similar to batteries which, unlike conventional power systems, convert the chemical energy directly into electricity, thus resulting in higher energy efficiencies. Fuel cells consist of three major compartments: the anode, the electrolyte and the cathode. The electrolyte is a proton or ion conductive medium (liquid or solid). The fuel and the oxidant are fed in the anode and cathode respectively, where electrochemical reactions take place. In the anode, electrons are released and travel through an external circuit towards the cathode generating electricity. Heat is also produced as a byproduct of the electrochemical reactions. The ability of fuel cells for continuous operation as long as fuel is supplied differentiates them from conventional batteries and makes them promising alternatives for power generation.

Different types of fuel cells have been developed; these are classified based on their operating temperature in low, intermediate and high temperature fuel cells. Representative types of fuel cells for each category include the Polymer Exchange Membrane (PEM) fuel cells, Phosphoric Acid Fuel Cells (PAFC), Molten Carbonate Fuel Cells (MCFC) and Solid Oxide Fuel Cells (SOFC). Their main features are illustrated in Table 1.1, where CHP denotes Combined Heat and Power. Apart from their different operating temperature, fuel cells exhibit different features in terms of materials selection, electrolyte conductivity and fuel flexibility. A comparative analysis of the basic

Table 1.1: Main characteristics of different types of fuel cells [1, 2]

Fuel Cell	PEM	PAFC	MCFC	SOFC
Operating Temperature	40–80^{o}C	150–200^{o}C	600–700^{o}C	600–1000^{o}C
Electrolyte	Polymeric Membrane	Phosphoric Acid	Molten Carbonates	Ceramics
Applications	Portable Transportation Distributed generation	Distributed generation CHP	Stationary Distributed generation CHP	Stationary Distributed generation CHP

features of PEM and SOFC fuel cells, which are considered to be closer to large–scale commercialization than the other types of fuel cells, reveals their potential range for different applications. PEM fuel cells are low temperature fuel cells employing a proton conductive solid (e.g polymeric membrane) electrolyte, exhibiting high power densities and quick start up responses. However, their slow kinetics at the cathode results in elevated capital cost for noble metals (e.g. Pt) in the electrodes [26]. In addition to this, low temperature PEM fuel cells require high–purity hydrogen as a fuel, since they are sensitive to fuel impurities (e.g. CO) which can potentially poison the polymeric membrane resulting in a performance degradation [27]. Apart from the above mentioned challenges, water management in the cathode is a major issue in low–temperature PEM fuel cells. To alleviate the above challenges, high temperature (>100^{o}C) PEM fuel cells have attracted a lot of attention since they have demonstrated a higher tolerance to fuel impurities, potential for lower capital cost through the use of non–platinum catalyst and easier water management [28, 29]. Despite their attractive features, high operating temperatures cause problems related to membrane dehydration and materials degradation [30, 31]. On the other hand, SOFC fuel cells require expensive ceramic materials in order to tolerate the high operating temperatures while they exhibit a high fuel flexibility [27]. Their high fuel flexibility allows their integration with conventional (e.g. coal) power plants and internal combustion engines as an auxiliary unit [32]. Furthermore,

their potential for co–generation of heat and power makes them an attractive option for CHP applications and promising for energy integration with energy intensive processes such as steam reformers.

The first application of fuel cells was in the aerospace industry during the mid–60s and 70s [33]. However, the growing need for highly efficient power generation has brought them to the forefront of power generation. Several companies have manufactured and commercialized fuel cells for residential and decentralized stand–alone applications ranging from 5 kW to MW–scale fuel cell modules. Some representative fuel cell companies include: Ballard (PEM), ClearEdge Power (PEM–PAFC), Fuelcell Energy (MCFC), Bloomenergy (SOFC) and Siemens Westinghouse (SOFC). In addition to this, the automotive industry has demonstrated high interest in fuel cells as a potential alternative to internal combustion engines and promising for integration with the existing technology in hybrid vehicles [34]. Several prototype vehicles have been manufactured while a small number of commercialized vehicles are available in selected areas around the world (e.g. South California, Japan)[21]. A complete list with more details on the technical specifications of different fuel cell vehicles can be found in [21].

Although high temperature (1000^oC) SOFC fuel cell systems have been already commercialized, their high capital cost and limited lifetime has motivated research and development of intermediate temperature SOFC fuel cell systems. Given the reduced ionic conductivity of the electrolyte due to the lower operating temperature, different cell configurations (e.g. anode–supported) have been demonstrated to reduce the electrolyte resistance and achieve a sufficient power density. Given the SOFC potential for energy integration, process systems analysis is essential in such integrated energy systems in order to determine design limitations, operational feasibility and controllability.

1.3 Process intensification: re–engineering process energy systems

Process intensification emerged in the early 80's, driven by the need for increased process efficiencies in the chemical industry [35]. According to [36]:

> *'Any chemical engineering development that leads to a substantially smaller, cleaner, safer and more energy efficient technology is process intensification'.*

Typical examples of processes exhibiting process intensification features include reactive and hybrid distillation units, reactor heat exchangers, micro–reactors, spinning disk reactors and rotating bed reactors [35, 37].

Power plants show similarities to conventional chemical plants since both convert the feedstock to end products through a series of processes. Tighter policies in CO_2 emissions and the prospect of zero carbon emissions power generation has motivated the use of carbon capture technologies. Pre– and post–combustion carbon capture integration has been proposed using either physical solvent or amine–based absorption units. Despite their different features, both technologies are energy intensive due to the large amount of solvent regeneration. As a result the overall efficiency drops as shown in Figure 1.1.

Membrane reactors have been of great interest since they allow for pre–combustion process intensification in conventional power plants. A typical example is the high–purity hydrogen generation unit for carbon–free coal–based power generation. This unit consists of two packed–bed water gas shift (WGS) reactors where coal–derived syngas is upgraded to hydrogen and carbon dioxide. CO_2 is captured in a conventional carbon capture unit while the hydrogen is fed to the power generation unit (Figure 1.2). The use of a WGS membrane reactor allows for simultaneous high–purity hydrogen production and CO_2 capture in a single unit, as shown in Figure 1.2. Membrane reactors

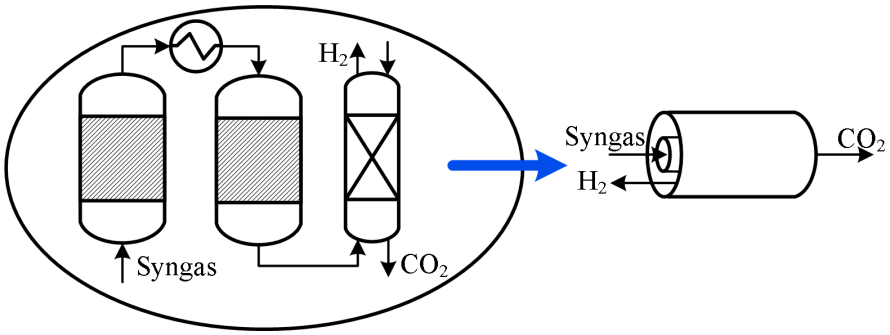

Figure 1.2: An illustration of process intensification in high–purity hydrogen generation unit.

can also be easily scaled–up to multitubular modules and demonstrate a high level of compactness. In addition to this, the integration of membranes with equilibrium limited reactions, leading to a single reaction–diffusion unit operation, substantially enhances the performance of the process intensified unit compared to conventional packed–bed reactors and can potentially lead the reactions to completion [38].

Although process intensification is advantageous in terms of cost, energy efficiency and process safety, there have been concerns and open issues on the operability, dynamics and control of process intensified units [39, 40]. Additionally, membrane reactors involving exothermic equilibrium reactions intensify the existence of large temperature gradients which can potentially deteriorate both the catalyst's and membrane's performance. Given the frequent changes in operating conditions along with the process complexity, thermal management of membrane reactors is essential in order to alleviate any potential risk for performance degradation and process safety. In addition, membrane reactors exhibit complex dynamic features requiring advanced process control strategies in order to ensure a safe transition between different operating conditions.

1.4 Combined Heat and Power Systems: transforming the energy market

In addition to the development of alternative energy conversion units (e.g. fuel cells), the potential of capturing and transforming the waste heat either into power or useful heat for heating/cooling purposes has stimulated the development of cogeneration units also known as combined heat and power (CHP) systems [41]. Given the advantageous features of SOFC fuel cells for both large–scale and decentralized power plants, SOFC–based CHP systems are promising for very high overall efficiencies [42, 43] and high grade heat generation [44, 45]. In addition to this, they offer energy reliability mitigating any risk for power outages, increase the robustness of the energy infrastructure by decreasing the load in the transmission grid [46], and limit the investment costs for new expansions of the transmission network [47]. Thus SOFC–based CHP plants are considered an attractive option for residential [48] and commercial applications [49].

The total energy consumption in the residential and commercial sectors corresponds to electricity, heating, and cooling. Current technologies used for heating and cooling are either gas–fired or electric–fired [50]. Although new, more efficient constructions, involving better insulation materials, have resulted in a decrease of the demand for heating/cooling [43], its contribution to the total energy consumption remains significant (48% in 2009 [51]).

Most of the design analysis in CHP has focused on maximizing the electrical or overall efficiency. Given the volatile demand for heat and power in residential and commercial sectors, design flexibility is considered a key factor in CHP plants [52]. To analyze design flexibility, the heat–to–power ratio has emerged as an important design and operational variable [53]. In addition, the use of material recycles in CHP plants has been proposed as an option to improve designs and performance [54, 55].

The effect of recycle ratios has been mainly analyzed using sensitivity analysis [55, 56]. However, introducing more design variables increases the complexity of the CHP plants. Although sensitivity analysis is usually the first stage of analyzing the impact of one or more design variables to the plant, optimization tools are essential for determining the optimal design configuration under different operational modes (e.g. maximum electrical efficiency and maximum heat to power ratio) given specified operational and safety–related constraints.

1.5 Thesis outline

The thesis aims to address operational challenges and analyze design alternatives for highly efficient large–scale and decentralized fuel cell–based power generation. It focuses mainly on energy systems employing SOFC and process intensification technologies for simultaneous hydrogen production and carbon capture.

In chapter 2, the SOFC fundamental features and principles of operation are discussed. Chapter 3 addresses the notion of energy integration in energy systems consisting of a fuel processor and a SOFC. Two energy integrated configurations are analyzed. A control strategy is proposed for each design alternative and its performance is evaluated using linear multi–loop controllers. Furthermore, an overall assessment of the operability of each design is also performed.

The use of membrane reactors as a process intensification technology for simultaneous hydrogen production and pre–combustion carbon capture in energy systems is considered in Chapter 4. Issues associated with their thermal management are identified and different control strategies are proposed using model–based controllers.

Chapter 5 discusses process design challenges in SOFC–based CHP plants under different operational modes. The role of material recycles in SOFC–based CHP plants

is discussed and an optimization problem is formulated in order to propose optimal designs for each operational mode. In the last chapter, (Chapter 6) the conclusions of this thesis are summarized and future directions for continuation of this work are also briefly mentioned.

CHAPTER 2

Solid Oxide Fuel Cells

Overview: The basic structure and fundamentals on the operation of a Solid Oxide Fuel Cell single cell are addressed. A brief description on different cell geometries and configurations is presented. Current technologies allowing for fuel flexibility are described. Their main features and challenges are also discussed.

2.1 Basic features and fundamental operation

The basic structure of a single SOFC is illustrated in Figure 2.1. The oxidant (e.g. O_2) is fed in the oxidant channel wherein it diffuses to the porous cathode (electrode) and electrochemically reacts with electrons, supplied through an external electric circuit, producing oxygen ions:

$$\frac{1}{2}O_2 \; + \; 2e^- \rightarrow O^{2-} \tag{2.1}$$

The produced oxygen ions migrate through the ionic conductive electrolyte to the porous anode (electrode) participating in the fuel oxidation reaction forming water vapor and releasing electrons:

$$H_2 \; + \; O^{2-} \rightarrow H_2O \; + \; 2e^- \tag{2.2}$$

Both reactions take place at the interface of the electrode, the electrolyte and the gas phase known as triple phase boundary (TPB) point. The continuous movement of electrons from the anode towards the cathode generates electricity (Figure 2.1) while heat is released based on the following overall reaction:

$$H_2 \; + \; \frac{1}{2}O_2 \rightarrow H_2O \qquad\qquad \Delta H^o_{298\ K} = -241.83 \;\; \text{kJ/mol}$$

Both the electrodes and the electrolyte are solid materials offering advantages in terms of design, manufacturing and compactness. The solid nature of the electrolyte counterbalances issues associated with complex electrolyte management and corrosion conditions which typically occur in fuel cells with highly corrosive liquid electrolytes (e.g. PAFC and MCFC) [33]. In addition, SOFCs show a high tolerance to fuel impurities and a large fuel flexibility making them promising for integration with a variety of different technologies such as coal/biomass gasification and hydrocarbon steam reforming.

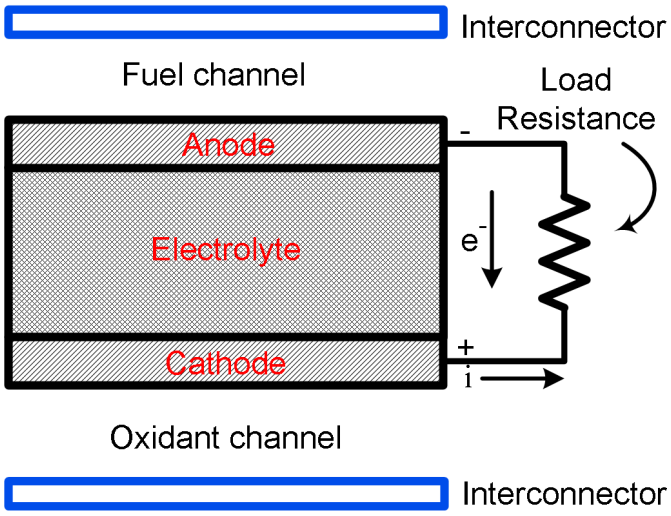

Figure 2.1: Basic structure of a SOFC single cell

The ability of SOFCs to electrochemically oxidize CO:

$$CO \ + \ O^{2-} \rightarrow CO \ + \ 2e^{-} \tag{2.3}$$

is a characteristic example of improved tolerance to impurities and fuel flexibility. Usually, CO exists in syngas produced either in gasification [57] or steam reforming units [58] and has been considered the major poisoning chemical compound in PEM fuel cells.

The SOFC high operating temperature results in low activation energies and high reaction rates at both electrodes, alleviating the need for expensive noble metals [33, 59] for the electrodes to promote the reaction rates. Furthermore, internal reforming of hydrocarbons is considered a unique feature of SOFC, where endothermic steam reforming reactions are coupled (either directly or indirectly [60, 61]) with exothermic electrochemical reactions with potential for higher efficiencies and reduced cooling requirements [62].

On the other hand, the SOFCs high operating temperature imposes several challenges including issues associated with carbon formation though the Boudouard and cracking reactions:

$$2CO \rightleftharpoons CO_2 + C \tag{2.4}$$

$$CH_4 \rightleftharpoons 2H_2 + C \tag{2.5}$$

leading to anode deactivation [63]. To prevent carbon deposition in the anode electrode, steam is fed along with fuel at the inlet of the anode. Given the high reaction rates at the anode, the presence of steam allows the CO to be converted, through the water gas shift reaction, to CO_2 and H_2 much faster than its associated electrochemical reaction [33]. Therefore, it is usually assumed that H_2 is the only electrochemically active compound in a SOFC [64, 65, 66]. However, there have been studies in the literature where both CO and H_2 are electrochemically oxidized [67, 68]. In terms of improving the lifetime and making SOFCs more economically attractive and competitive to other power generation technologies, substantial efforts have focused on decreasing their operating temperature (intermediate temperature SOFC), allowing for cheaper materials and reduced thermal stresses. In the following sections, a discussion of different SOFC designs is presented.

2.2 SOFC stack design configurations

A SOFC stack consists of a number of single cells connected in series in order to scale up the output power. Two main SOFC stack design configurations have been developed: the planar (Figure 2.2) and tubular (Figure 2.3). Advantages of planar configuration include high power densities and reduced fabrication cost while the need for high–temperature gas tight seals and large thermal stresses constitute common disadvantages. On the other hand, the tubular configuration eliminates the need for high–temperature

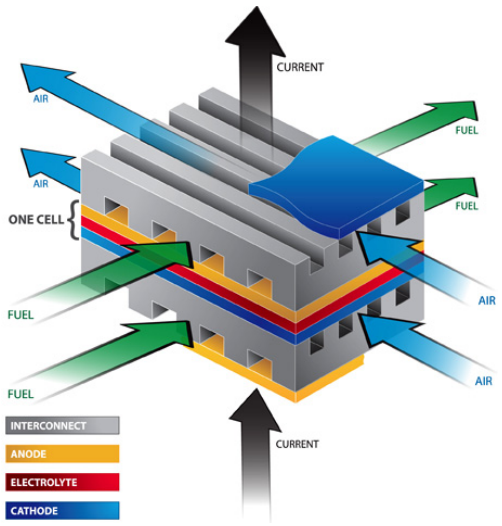

Figure 2.2: Planar SOFC configuration (adopted from [4])

gas tight seals and features a improved lifetime. However, the large ohmic losses due to the tubular geometry lead to lower power densities [69].

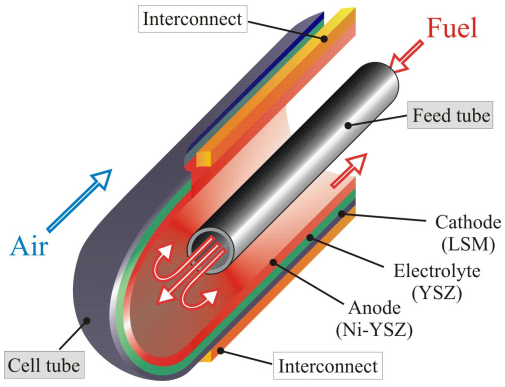

Figure 2.3: Tubular SOFC configuration (adopted from [5])

In addition to the different SOFC geometries, different cell configurations are also available including electrolyte– and electrode–supported configurations. Electrolyte–supported cell configurations include a thick electrolyte and thin electrodes leading to low activation and concentration polarizations and high ohmic polarizations. In terms of

electrode–supported SOFCs, anode–supported cell configurations are favored for planar geometries while the cathode–supported configuration has been used in tubular SOFCs [70]. The thin electrolyte in the electrode–supported SOFCs allows for a reduced operating temperature which is beneficial in terms of materials cost and lifetime of the stack [71]. Based on this unique feature, anode–supported planar SOFCs have attracted a lot of attention as a promising option for lower operating temperature and high power densities.

2.3 Fuel flexibility

SOFCs exhibit a wide range of fuel flexibility making them promising candidates for the entire spectrum of applications for power generation. Typical options for hydrocarbon–fed SOFCs include: a) internal reforming, b) external reforming and c) direct oxidation of hydrocarbons.

Internal reforming constitutes a major feature of SOFCs which distinguishes them from low temperature fuel cells. The option of coupling a highly endothermic reforming reaction with an exothermic electrochemical reaction results in a process intensified SOFC unit with increased process efficiencies and no need for an external reforming unit. As mentioned above, two types of internal reforming are available, direct and indirect internal reforming. Direct internal reforming involves both physical and thermal contact of the species within the anode while indirect internal reforming allows only for thermal contact between the reforming and anode channel. Although indirect internal reforming is less efficient than direct internal reforming, it provides increased controllability of the reforming reaction [72].

External reforming is achieved by integrating either steam reforming, partial oxidation or autothermal reforming units upstream to the SOFC. Steam reforming units

lead to high yields of hydrogen however they require reliable thermal management in order to drive the endothermic reforming reaction [69]. On the other hand, partial oxidation units exhibit fast transient responses due to the exothermic nature of the partial oxidation reaction [69]. Oxygen, required for the partial oxidation reaction, is usually supplied through the use of air. As a result, large amount of nitrogen is fed to the partial oxidation reactor leading to lower hydrogen concentrations at the outlet compared to a steam reforming unit. The effect of employing either a partial oxidation or a steam reforming reactor on a propane–fed SOFC was analyzed in [73]. The study showed that the nitrogen dilutes the concentration of hydrogen at the anode of the SOFC leading to a lower operating voltage and hence a lower performance. Autothermal steam reformers are process intensified units including both the steam reforming and the partial oxidation reaction within the same process unit. Autothermal reforming units adopt the advantages of the partial oxidation unit and have a higher yield of hydrogen compared to the partial oxidation unit [69]. However, the combination of highly exothermic and highly endothermic reactions exhibit complex dynamic behavior and requires sophisticated control algorithms for proper thermal management [74].

Direct oxidation of hydrocarbons within the SOFC has attracted a lot of attention as an alternative to hydrocarbon steam reforming. The operation of SOFCs under direct electrochemical oxidation is expected to make them more attractive for transportation and distributed power generation [75]. The operation of direct oxidation SOFCs has been analyzed for several types of fuels (e.g. methane, ethane, n–butane, diesel) [75, 76, 77, 78]. The option of direct electrochemical oxidation alleviates the need for diluting fuels with steam and decreases the complexity of the entire SOFC system [79]. Issues associated with carbon formation at high temperature [78, 77] and poor performance at low temperatures [77] have motivated a lot of research on alternative anode materials.

CHAPTER 3

Energy Integrated Solid Oxide Fuel Cell Systems: Design and Control Analysis*

Overview: Energy integrated SOFC systems are promising for highly efficient and environmentally friendly power generation. In this chapter, the design and operation of energy integrated SOFC systems employing an external fuel processor are analyzed. Two design configurations are considered: one where the hot effluent streams from the fuel cell are used directly for energy integration, and another where the hot effluent streams are mixed and combusted in a catalytic burner before the energy integration. A comparative evaluation of the two configurations is presented in terms of their

design, open-loop dynamics and their operation under linear multi–loop controllers. In addition, a sensitivity analysis is performed where the effect of the fuel processor design parameters (steam-to-carbon (S/C) ratio and operating temperature) on the design, dynamics and control of the entire SOFC system is analyzed.

3.1 Introduction

Recognizing the need for efficient power generation units, there has been an increasing interest in developing fuel cell systems for stationary and transportation applications (see *e.g.* [81, 82, 83, 84, 85, 86, 87] for excellent overviews on recent developments and opportunities in modeling and control of fuel cell systems). Given the issues associated with the storage and transportation of hydrogen, *in situ* production of hydrogen from a hydrocarbon fuel, coupled with a H_2-fed SOFC, presents a promising approach for power generation.

Two approaches have been proposed to this end. One of the approaches uses an *external* fuel processor [88, 89, 90, 55] to generate a hydrogen-rich stream which is then fed to the fuel cell while the other approach uses the principle of *internal* reforming [55, 91]. In this analysis, we focus on the approach employing an external fuel processor (e.g. steam reformer) as it offers more opportunities for integration and control design.

A power system consisting of an external steam reformer and a fuel cell exhibits a lower overall efficiency, since additional energy is required to drive the endothermic reforming reactions. However, given the SOFC high operating temperature (800 ^{o}C-1000 ^{o}C), the hot streams leaving the SOFC show potential for energy integration by supplying energy to the endothermic reformer, and thereby improving the overall efficiency. Different integration strategies for SOFC energy systems have been proposed

(see e.g. [92] which reviews most of these strategies). These include hybrid integration strategies with direct thermal coupling [93, 94], indirect thermal coupling [95] as well as fuel coupling [96], and advanced integration strategies using gas/humid air/steam turbines [97, 98, 99, 100]. Some of these strategies directly (without mixing the anodic and cathodic stream) use the hot SOFC effluent for energy recovery (e.g. [101, 102]), while others use a catalytic burner to further recover energy from the unreacted fuel and utilize this stream for energy integration (e.g. [93, 90]). While each of these approaches has obvious advantages/disadvantages in terms of capital and operating costs, compatibility with downstream processes, and environmental impact, they also offer different opportunities and challenges in terms of overall integrated system design, dynamics and control. This is a rather untouched subject in the literature. Motivated by this, in this chapter we compare (and contrast) these two approaches at the design and operational stages. The results of this analysis can guide the selection of a particular approach. To this end, we consider a generic SOFC energy system with an external methane steam reformer. Energy recovery is achieved by designing a heat exchanger network (HEN). Through open-loop simulations under imposed step changes in the current, the dynamic behavior of each of the configurations is analyzed. Linear multi-loop control strategies are proposed for each case and the operational characteristics are compared through closed-loop simulations.

The structure of the chapter is as follows. The modeling details for the fuel cell and the reformer are presented in section 3.2. The selection of operating points for each of these units based on steady state analysis is presented in section 3.3. The design, dynamics and control aspects of the energy integrated configurations are analyzed in sections 3.4, 3.5 and 3.6, respectively. The impact of steam reformer design parameters on the design and control of the entire energy integrated configuration is addressed in section 3.7.

3.2 Integration of SOFC and external steam reformer

A generic SOFC energy system employing an external methane steam reformer (SR) is shown in Figure 3.1. As the reformer and the fuel cell operate at a high temperature,

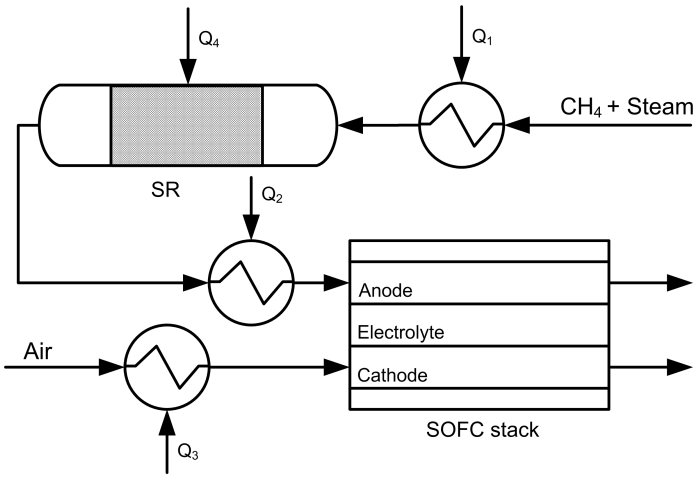

Figure 3.1: Generic design structure of the SOFC energy system

three heat transfer units are required to heat the methane steam mixture, fuel cell anode and cathode inlet streams. Furthermore, energy is required for sustained hydrogen production in the endothermic steam reformer. In the following subsections, we present the modeling details for the fuel cell and the reformer which are the major operation units of the system.

3.2.1 SOFC Mathematical Model

The open-circuit voltage that can be generated by the fuel cell is given by the Nernst equation:

$$E_{OCV} = E_o(T_{FC}) + \frac{RT_{FC}}{2F}\ln\left(\frac{p_{FC,H_2}\cdot p_{FC,O_2}^{0.5}}{p_{FC,H_2O}}\right) \tag{3.1}$$

where $E_o(T_{FC})$ is the temperature dependent standard potential [33], p_i denotes the partial pressures of each species i at the anode, T_{FC} is the temperature of the fuel cell and F is the Faraday constant. However, when connected in a circuit, the output voltage of the fuel cell decreases due to the existence of irreversible losses (called polarizations). The output voltage of the fuel cell delivered to the load is given by the following equation:

$$V_{FC} = E_{OCV} - \eta_{act} - \eta_{ohm} - \eta_{conc} \tag{3.2}$$

where $\eta_{act},\ \eta_{ohm},\ \eta_{conc}$ represent the activation, ohmic and concentration polarizations respectively. Activation polarization is described as the energy barrier that should be overcome by the reacting species. It is calculated using the Bulter-Volmer equation [103]:

$$I = I_o \cdot \left\{ exp\left(\frac{\alpha n F \eta_{act}}{RT_{FC}}\right) - exp\left(-(1-\alpha)\frac{nF\eta_{act}}{RT_{FC}}\right)\right\} \tag{3.3}$$

where I_o is the apparent exchange current (calculated following [104]) and α the transfer coefficient. The voltage drop due to the resistance in the flow of electrons and ions can be described by the ohmic polarization which is determined by Ohm's law as shown below:

$$\eta_{ohm} = I \cdot (R_{an} + R_{el} + R_{ca} + R_{int}) \tag{3.4}$$

where R_i is the resistance of each compartment (calculated from [105]) and the subscripts (an, el, ca, int) refer to the anode, the electrolyte, the cathode and the interconnector. Moreover, concentration polarization represents the voltage drop due to the concentration gradients between the bulk gases and the triple phase boundary point, the interface between the electrolyte and the electrode where the electrochemical reactions occur. It

is calculated from the following equation:

$$\eta_{conc} = \frac{RT_{FC}}{2F} ln\left(\frac{I_L}{I_L - I}\right) \tag{3.5}$$

where I_L is the limiting current in the fuel cell. The output voltage and the power for the entire SOFC stack are given below:

$$V = N \cdot V_{FC} \tag{3.6}$$

$$P = I \cdot V \tag{3.7}$$

where N is the number of individual cells in the stack.

We now move to the material and energy balance equations for the fuel cell. The objective of this study is to analyze the system-wide characteristics of energy integrated SOFC systems. Recent studies have shown, through experimental validation, that lumped parameter models are sufficiently accurate for such systems-level analysis and control [106]. Numerous other papers also employ lumped parameter models for analysis and control of SOFC systems (see e.g. [98, 88, 107]). Therefore, we have used such a lumped parameter model to describe the dynamics of the fuel cell. It is assumed that there is no interaction between each individual cell. Therefore, the inlet anode and cathode flows are split into N streams. In addition, the model assumes constant pressure and physical properties, ideal gas behavior and adiabatic operation. The species and energy balances take then the following form:

$$\frac{dn_{FC,H_2}}{dt} = \dot{n}_{FC,H_2,in} - \dot{n}_{FC,H_2} - \frac{I}{2F} \tag{3.8}$$

$$\frac{dn_{FC,H_2O}}{dt} = \dot{n}_{FC,H_2O,in} - \dot{n}_{FC,H_2O} + \frac{I}{2F} \tag{3.9}$$

$$\frac{dn_{FC,O_2}}{dt} = \dot{n}_{FC,O_2,in} - \dot{n}_{FC,O_2} - \frac{I}{4F} \tag{3.10}$$

$$\frac{dT_{FC}}{dt} = \frac{1}{\rho_{SOFC} Cp_{SOFC} V_{SOFC}} \cdot (\dot{Q}_{fuel,in} - \dot{Q}_{fuel,out} + \dot{Q}_{air,in} - \dot{Q}_{air,out} - \dot{n}_{H_2}^{reacted} \cdot \Delta H_{FC}^{rxn} - I \cdot V_{FC}) \quad (3.11)$$

$$\dot{n}_{H_2}^{reacted} = \frac{I}{2F} \quad (3.12)$$

$$\dot{Q}_i = \sum_j \dot{n}_j \; Cp_j \; (T_i - T_{ref}) \quad (3.13)$$

where the subscripts (i) and (j) refer to the corresponding streams and components while (FC) denotes the fuel cell and $\dot{Q}_i$ represents the enthalpy flow. Eq. (3.12) represents Faraday's law.

3.2.2 SR Mathematical Model

A methane steam reformer is used to convert methane into a hydrogen-rich stream. This is accomplished through the following two catalytic reactions:

$$\text{Reforming reaction: } CH_4 + H_2O \rightleftharpoons CO + 3H_2 \qquad \Delta H^o_{298} = 206.10 \text{ kJ/mol} \quad (3.14)$$

$$\text{WGS reaction: } CO + H_2O \rightleftharpoons CO_2 + H_2 \qquad \Delta H^o_{298} = -41.15 \text{ kJ/mol} \quad (3.15)$$

Note that even though the first reaction is endothermic and the second is exothermic, the net system of reactions is endothermic, requiring external energy input for sustained hydrogen production. Here, we model the reformer as a well-mixed reactor with a heating jacket. Assuming constant pressure, constant physical properties and ideal gas behavior, the species mass balances take the form:

$$\frac{dn_{SR,CH_4}}{dt} = \dot{n}_{SR,CH_4,in} - \dot{n}_{SR,CH_4} - m_{cat} \cdot r_1 \quad (3.16)$$

$$\frac{dn_{SR,H_2O}}{dt} = \dot{n}_{SR,H_2O,in} - \dot{n}_{SR,H_2O} - m_{cat} \cdot (r_1 + r_2) \quad (3.17)$$

$$\frac{dn_{SR,CO_2}}{dt} = \dot{n}_{SR,CO_2,in} - \dot{n}_{SR,CO_2} + m_{cat} \cdot r_2 \tag{3.18}$$

$$\frac{dn_{SR,CO}}{dt} = \dot{n}_{SR,CO,in} - \dot{n}_{SR,CO} + m_{cat} \cdot (r_1 - r_2) \tag{3.19}$$

$$\frac{dn_{SR,H_2}}{dt} = \dot{n}_{SR,H_2,in} - \dot{n}_{SR,H_2} + m_{cat} \cdot (3r_1 + r_2) \tag{3.20}$$

where m_{cat} is the mass of the catalyst and r_i is the rate of each reaction. The reaction rate expressions are obtained based on a Langmuir-Hinshelwood reaction mechanism as proposed in [108]. The energy balances for the reactor and the jacket have the following form:

$$\frac{dT_{SR}}{dt} = \frac{(\dot{Q}_{fuel,in} - \dot{Q}_{fuel,out} - m_{cat}\,(r_1 \Delta H_1^{rxn} + r_2 \Delta H_2^{rxn}) + UA_{SR}\Delta T_{LM})}{(\varepsilon \rho_g C p_g + (1-\varepsilon)\rho_{cat} C p_{cat})\, V_{SR}} \tag{3.21}$$

$$\frac{dT_{SR,HOT}}{dt} = \frac{\left(\dot{Q}_{SR,HOT,in} - \dot{Q}_{SR,HOT,out} - UA_{SR}\Delta T_{LM}\right)}{MCp_{SR,HOT}} \tag{3.22}$$

where the subscripts (g), (cat) refer to the gas and catalyst properties, V_{SR} is the volume of the steam refomer, ε is the void fraction, UA_{SR} is the product of the overall heat transfer coefficient and the heat exchange area and ΔT_{LM} is the mean logarithmic temperature difference.

3.3 Steady state analysis

In what follows, a steady state analysis is performed for the SOFC and the reformer in order to select the operating points for these units. This will provide a starting point for the design of the integrated SOFC energy system.

3.3.1 Solid oxide fuel cell

The steady state values of the output voltage, output power and the cell temperature as a function of the current are shown in Figure 3.2. It is desirable to operate the SOFC close to the highest power production point with high fuel utilization (U_F). The fuel utilization represents the fraction of the incoming hydrogen that is electrochemically converted in the fuel cell. We selected the operating point corresponding to a current of 60.3 A. At this point, the power delivered by the fuel cell is 16.4 kW (99% of the maximum power), the output voltage is 272 V and the fuel cell temperature is 1162.6 K.

3.3.2 Methane Steam reformer

It is desired to operate the steam reformer at a temperature where a stream rich in hydrogen is produced with a high methane conversion [98]. We first explored the effect of the steam-to-carbon (S/C) ratio on methane conversion. Figure 3.3(a) shows the variation of methane conversion with respect to reformer temperature for various values of S/C ratios. High S/C values show enhanced methane conversion, however, at the cost of additional heating load. We selected S/C = 4 for this study. Figure 3.3(b) shows the steady state profiles for various species at the outlet of reformer as a function of operating temperature. Note that the hydrogen mole fraction shows a maximum for a reformer temperature close to 980 K. We selected the operating point to be 932.3 K. For this state, the methane conversion is 92.6% and the reformate gas contains approximately 49% hydrogen.

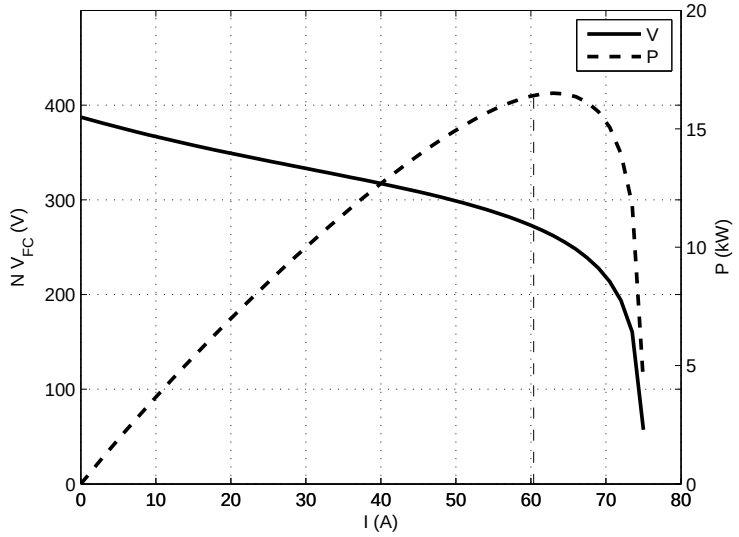

(a)

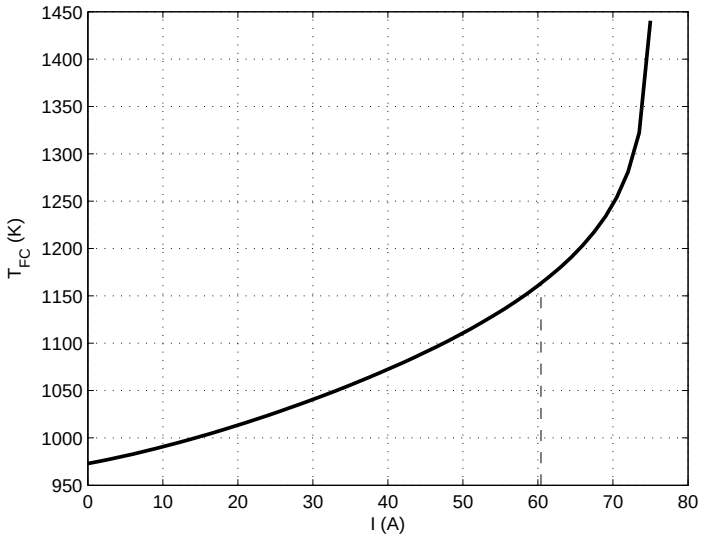

(b)

Figure 3.2: SOFC steady states of the voltage, power and temperature as a function of the current.

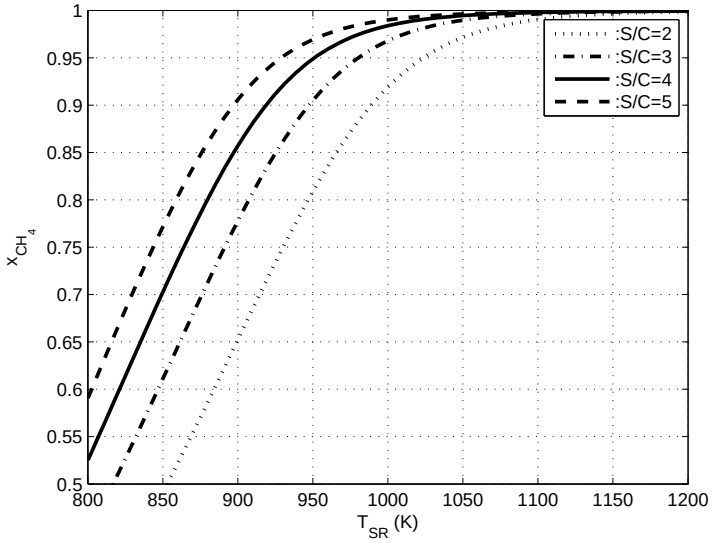

(a)

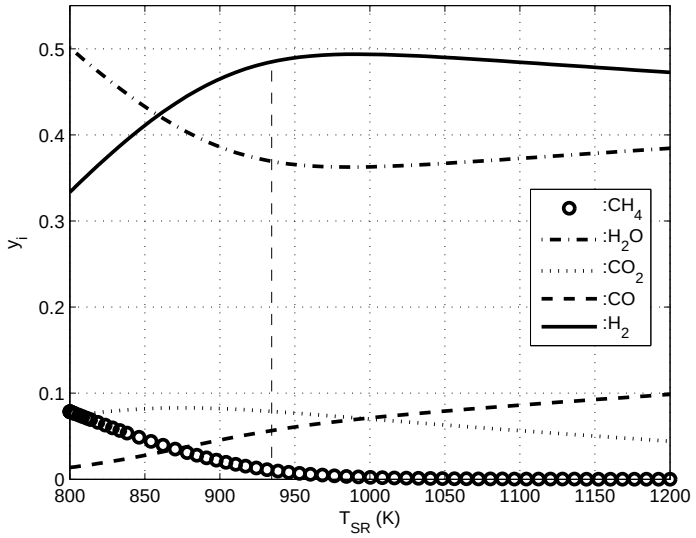

(b)

Figure 3.3: Steam reformer methane conversion at different S/C ratios and mole fraction steady states as a function of the reformer temperature.

3.4 Energy integration

The system in Figure 3.1 requires four external energy inputs. On the other hand, the SOFC exit streams leave at a high temperature thus, showing a potential for energy integration. Motivated by the previously proposed integration strategies [101, 102, 90, 93], two integration alternatives were considered: in the first, the hot anodic and cathodic exit streams from the fuel cell are used directly as two hot streams, while in the other, the anodic and cathodic streams are mixed together and are combusted in a catalytic burner to generate a single hot stream.

As a first step in the design of the energy integrated systems, we used pinch analysis [109]. Pinch analysis indicated that external hot utility is required for the first system while the second system is self sustaining. Pinch analysis also indicated the absence of a pinch point for both the cases, thus allowing for a variety of possible design alternatives [110].

- *Design of integrated configuration based on alternative 1*: Most of the existing configurations [101, 102] following this alternative focus only on the fuel cell and do not incorporate any fuel processing unit. In this study we incorporated such a fuel processing unit and we designed the heat exchanger network with the objective of achieving the minimum external utility predicted by the pinch analysis. The resulting integrated configuration is depicted in Figure 3.4. The cathode outlet stream provides energy to the steam reformer (SR) and then it is then split into two streams. One preheats the air in HE_7, while the other supplies energy for preheating methane in HE_4, water in HE_1 and steam in HE_3. The anode outlet stream covers the heating requirement of the anode inlet in HE_6. Then, it preheats the fuel mixture to the required reformer inlet temperature in HE_5 and then supplies the required energy for steam generation in HE_2. An external hot utility

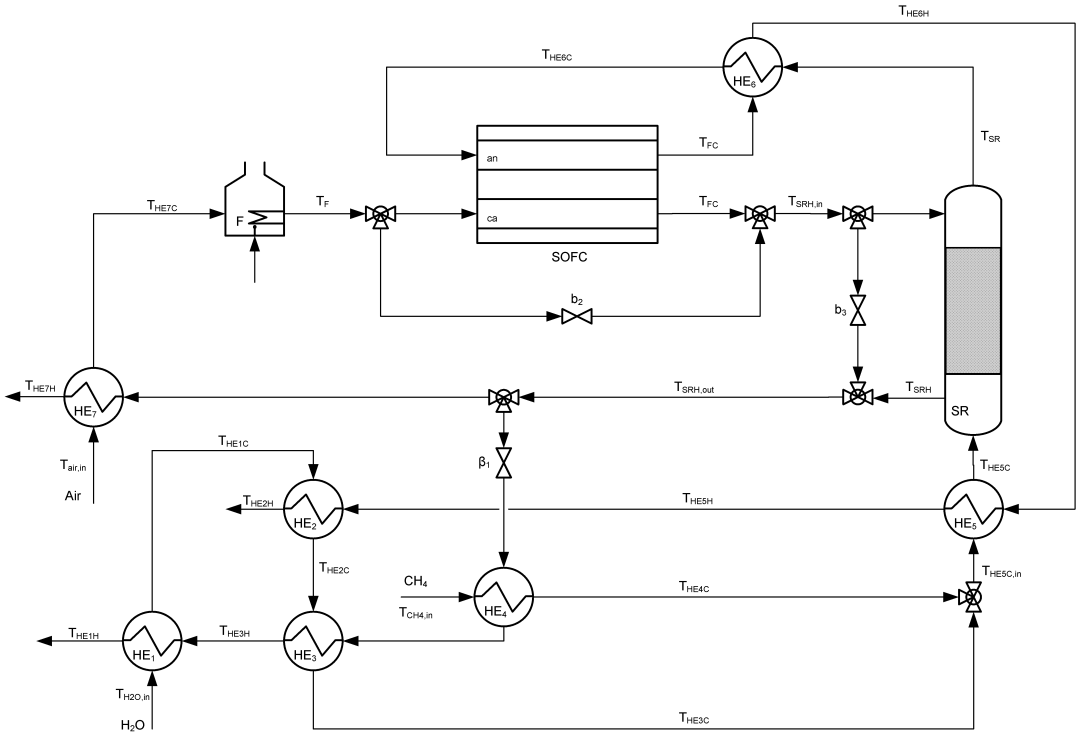

Figure 3.4: Energy integrated SOFC system - Configuration 1

is supplied to the furnace in order to heat the air to the required temperature. The resulting energy requirement (see Table 3.1) in this configuration is exactly the one predicted by the pinch analysis.

- *Design of integrated configuration based on alternative 2*: In this case, we used the integrated configuration proposed in [90] as a basis and achieved further recovery and recycle of energy, specifically through the addition of heat exchangers (1-3), (5) and (7) as shown in Figure 3.5. The anodic and cathodic outlet streams are fed to a catalytic burner, where the complete combustion of methane, carbon monoxide and unreacted hydrogen takes place. The required air is supplied by the SOFC cathodic stream. The high temperature stream leaving the burner heats the air in

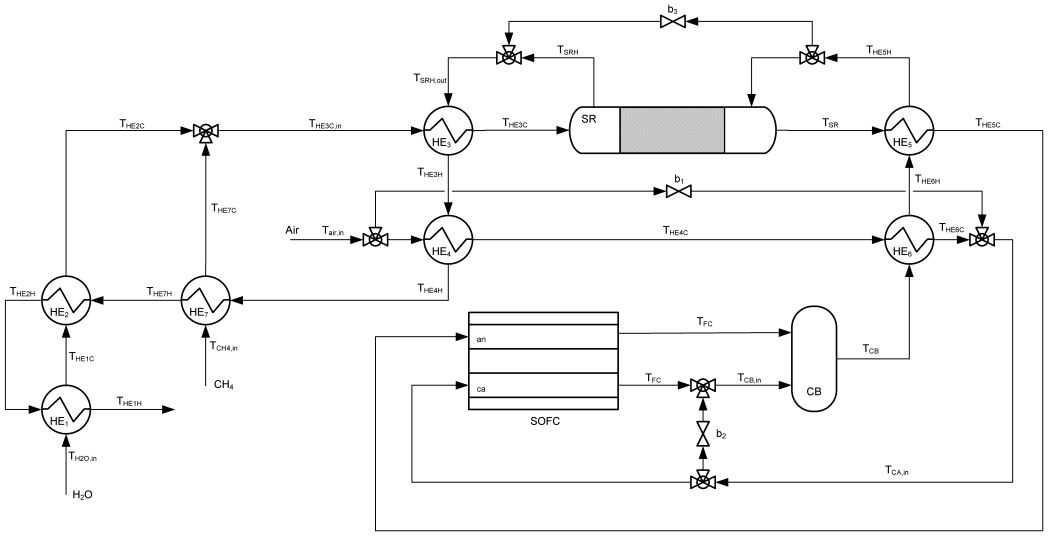

Figure 3.5: Energy integrated SOFC system - Configuration 2

HE_6 and provides energy to the anode inlet stream in HE_5. Then, it passes through the steam reformer (SR) in order to cover its endothermic demand. Leaving the reformer, the hot stream heats the fuel mixture to the temperature required by the reformer in HE_3 and then preheats the air stream in HE_4. Afterwards, it provides energy for both the preheating of the methane in HE_7 and the steam generation in HE_2 and HE_1.

Both configurations use seven process-to-process heat exchangers. While the first configuration uses a furnace (*external* energy source), the other uses a combustion unit (*internal* energy source). Bypasses b_2 and b_3 are placed to improve the controllability of the first configuration, while bypasses b_1, b_2 and b_3 are placed in the second configuration for the same reason. Tables 3.1 and 3.3-3.6 present the parameters that have been used for both configurations. Note that the same operating points (as selected in the previous section) are used for the fuel cell and the reformer. The composition and the total molar flow rate at the outlet of each major process are tabulated in Table 3.2.

Table 3.1: General parameters

Parameter	Value	Parameter	Value
N	384	P_{FC} (kPa)	101.3
V (V)	272	P_{SR} (kPa)	150.0
I (A)	60.3	Q_F (kW)	4.347
P (kW)	16.4	x_{CH_4}	0.926
S/C	4	$\dot{n}_{SR,in}$ (mol/s)	0.225
U_F	0.8	$\dot{n}_{air}$ (mol/s)	2.111
Configuration 1		Configuration 2	
β_1	0.09	b_1	0.10
b_2	0.10	b_2	0.10
b_3	0.10	b_3	0.10

The temperatures at each stream arising from the energy integration are tabulated in Table 3.7.

Table 3.2: Stream composition at the outlet of each major process

	SR	SOFC	CB
y_{CH_4}	0.011	0.011	0
y_{H_2O}	0.368	0.757	0.116
y_{CO}	0.054	0.054	0
y_{CO_2}	0.081	0.081	0.019
y_{H_2}	0.486	0.097	0
y_{O_2}	-	0.184	0.151
y_{N_2}	-	0.816	0.714
$\dot{n}_{total}$ (mol/s)	0.308	-	2.336
$\dot{n}_{an,total}$ (mol/s)	-	0.308	-
$\dot{n}_{ca,total}$ (mol/s)	-	1.840	-

3.5 Open-loop analysis

We next studied the dynamic response of each of these configurations. We considered a scenario where current changes are imposed which may be caused by power changes.

Table 3.3: Physical properties of each component

Component	ρ_i (kg/m^3)	Cp_i (J/mol/K)
CH_4	0.717	58.381
H_2O (g)	0.804	38.459
H_2O (l)	1000	75.327
CO	1.250	31.374
CO_2	1.977	49.561
H_2	0.089	30.236
O_2	1.429	32.582
N_2	1.251	31.394

Table 3.4: UA values for heat exchangers and steam reformer

UA_i (W/K)	Configuration 1	Configuration 2
SR	51.42	67.10
HE_1	24.45	8.09
HE_2	49.05	104.80
HE_3	15.36	11.62
HE_4	2.31	108.10
HE_5	4.63	3.23
HE_6	2.31	58.37
HE_7	1170	3.91

3.5.1 Small step increase in the current

Figure 3.18 shows the response of key variables for a step in the current from 60.3 A to 62 A. The increase in current causes an instantaneous increase in the amount of hydrogen reacted in the fuel cell (Eq. 3.12). This is reflected in the corresponding increase in the fuel utilization and the decrease in the burner temperature (less fuel for combustion) for the second configuration. The increased hydrogen consumption also results in increased fuel cell temperature, however over a longer horizon. Yet, the impact of the disturbance is different for the two configurations. The rise in the reformer temperature is much larger for configuration 1 than configuration 2. This

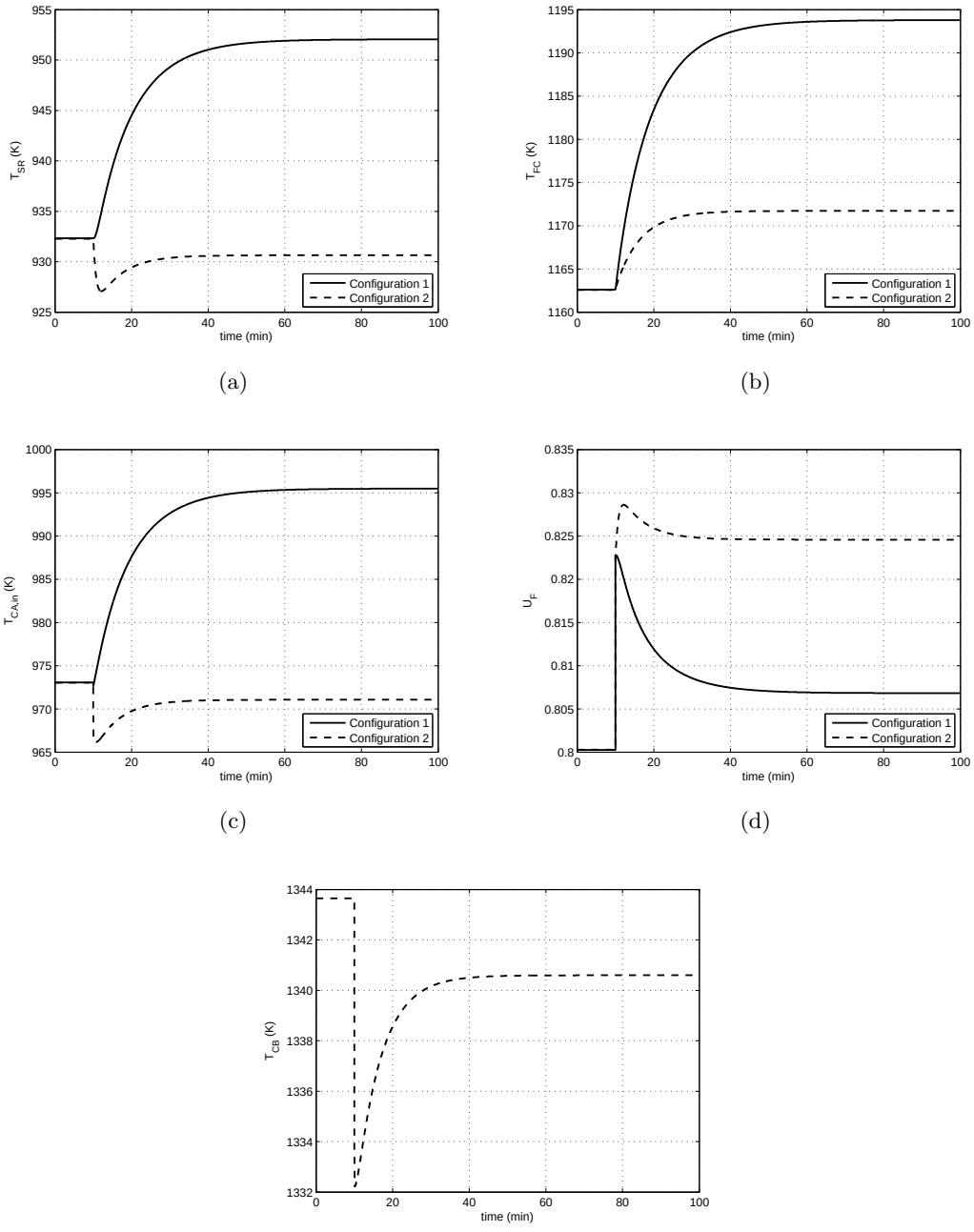

Figure 3.6: Open-loop simulation under a small step in the current from 60.3 A to 62 A

Table 3.5: MCp values used in the case study

MCp_i (J/K)	Configuration 1	Configuration 2
SRH	26.45	36.54
F	35.31	-
CB	-	36.54
$HE_{1,HOT}$	2.61	36.54
$HE_{2,HOT}$	0.19	36.54
$HE_{3,HOT}$	2.61	36.54
$HE_{4,HOT}$	2.61	36.54
$HE_{5,HOT}$	5.84	36.54
$HE_{6,HOT}$	5.84	36.54
$HE_{7,HOT}$	26.46	36.54
$HE_{1,COLD}$	857.89	857.89
$HE_{2,COLD}$	3.52	3.52
$HE_{3,COLD}$	3.52	4.74
$HE_{4,COLD}$	1.30	26.48
$HE_{5,COLD}$	4.74	5.36
$HE_{6,COLD}$	5.36	26.48
$HE_{7,COLD}$	35.31	0.86

Table 3.6: Detailed parameters used in the case study

Parameter	Value	Parameter	Value
L (m)	0.1	V_{SR} (L)	3.3
W (m)	0.1	ρ_{cat} (kg/m^3)	2335
A (cm^2)	100	ε	0.4
ρ_{SOFC} (kg/m^3)	4200	Cp_{cat} (J/kg/K)	444
Cp_{SOFC} (J/kg/K)	640	ΔH_{FC}^{rxn} (kJ/mol)	-241.83
τ_{an} (mm)	1	ΔH_{1}^{rxn} (kJ/mol)	206.10
τ_{el} (μm)	8	ΔH_{2}^{rxn} (kJ/mol)	-41.15
τ_{ca} (μm)	50	τ_{int} (mm)	1

is due to the fact that the inlet temperature for configuration 1 is higher than the nominal value, while for the second configuration, it is lower than the nominal value. The responses of the reformer temperature and the cathode inlet temperature show striking differences between the two configurations. In configuration 1, the increase

Table 3.7: Stream temperatures for each configuration

Configuration 1				Configuration 2			
Temperature	(K)	Temperature	(K)	Temperature	(K)	Temperature	(K)
$T_{CH_4,in}$	298.0	T_{HE5H}	1001.4	$T_{CH_4,in}$	298.0	T_{HE5C}	973.0
$T_{H_2O,in}$	298.0	T_{HE5C}	822.9	$T_{H_2O,in}$	298.0	T_{SR}	932.3
$T_{air,in}$	298.0	T_{SR}	932.3	$T_{air,in}$	298.0	T_{SRH}	950.1
T_{HE1C}	373.0	T_{SRH}	981.5	T_{HE1C}	373.1	$T_{SRH,out}$	963.8
T_{HE1H}	308.2	$T_{SRH,out}$	997.6	T_{HE1H}	457.3	T_{FC}	1162.6
T_{HE2C}	373.4	T_{FC}	1162.6	T_{HE2C}	515.7	T_{HE6H}	1092.9
T_{HE2H}	383.0	T_{HE6H}	1125.3	T_{HE2H}	470.6	T_{HE6C}	1048.0
T_{HE3C}	669.3	T_{HE6C}	973.0	T_{HE3C}	823.0	T_{HE7H}	579.2
T_{HE3H}	481.7	T_{HE7H}	306.8	T_{HE3H}	925.6	T_{HE7C}	520.0
T_{HE4C}	669.3	T_{HE7C}	907.9	T_{HE4C}	729.0	$T_{CB,in}$	1143.1
$T_{HE5C,in}$	669.3	T_F	973.1	T_{HE4H}	586.8	$T_{HE3C,in}$	516.9
T_{HE4H}	831.2	$T_{SRH,in}$	1143.1	T_{HE5H}	1087.1	$T_{CA,in}$	973.0
						T_{CB}	1343.7

in the fuel cell temperature increases the reformer temperature and the cathode inlet temperature in the same fashion. In the case of configuration 2, the increased current triggers opposing forces in the burner (increase the inlet temperature and decrease the temperature rise) resulting in an inverse response. For the magnitude of current change considered here, the net effect is the reduction in burner temperature below the nominal value. This drives similar responses in the reformer temperature and cathode inlet temperature. Thus configuration 2 is less sensitive to the current disturbance than configuration 1.

3.5.2 Large step increase in the current

We now subject the system to a large disturbance in current. Figure 3.19 shows the open-loop response of key variables for a step in the current from 60.3 A to 70 A. The responses for the first configuration indicate an open-loop instability triggered by the change in the operating region of the steam reformer. More precisely, the increase in the current causes an increase in the reformer temperature. This increases the hydrogen production rate supplying more fuel to the fuel cell. However, when the reformer temperature reaches to a point beyond the maximum hydrogen production (see Figure 3.3(b)), any further increase in reformer temperature decreases hydrogen production and hence, reduces the fuel supply to the cell. This drives the cell towards fuel starvation conditions, resulting in higher temperatures.

In the case of the second configuration, the system reaches a new steady state with responses similar to the case of a small current step. However, in this case, the catalytic burner temperature is higher than the nominal value, resulting in similar higher value in the reformer temperature. Note that the temperature increase in the steam reformer is quite small to trigger any instability. This again shows the ability of this configuration to maintain open-loop stability.

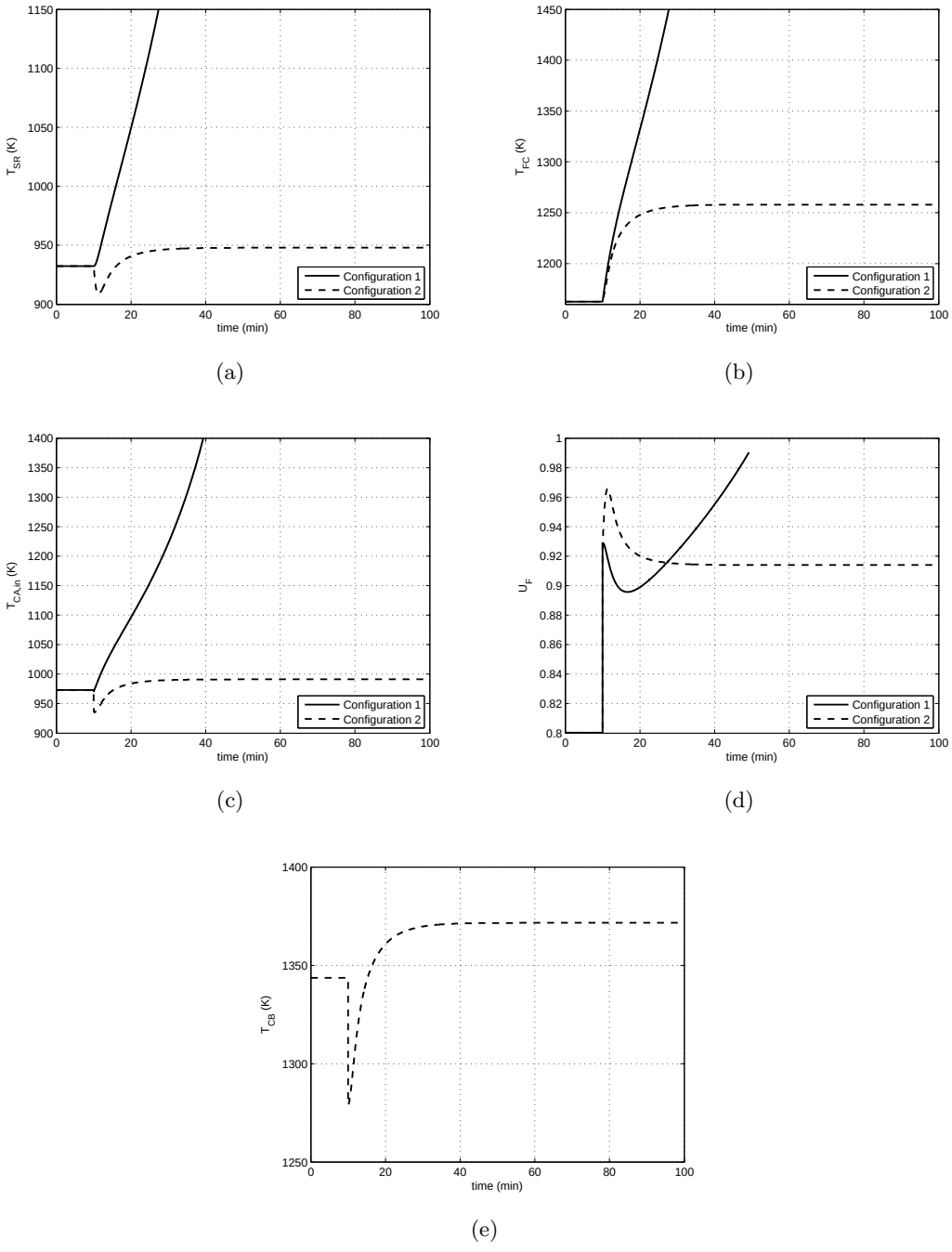

Figure 3.7: Open-loop simulation under a large step in the current from 60.3 A to 70 A

Remark 3.5.1 *Both open-loop simulation scenarios discussed above were performed for an increase in the current drawn from the SOFC. In the case of a decrease in the applied current, both configurations give stable open-loop responses even for large steps in the current (plots not included).*

3.6 Control design

3.6.1 Closed-loop analysis

In this paper we focus on the control problem only on the chemical side of the SOFC energy system. As chemical side of a SOFC system we refer to the part of the SOFC system which includes only the electrochemical phenomena taking place inside the SOFC, without including any power conditioning unit after the SOFC. The corresponding control objectives considered involve:

1. *SOFC temperature*: The SOFC is an exothermic system. An increase in the SOFC temperature shows potential for material damages while a decrease drops the ionic conductivity of the electrolyte. Thus, there is a need to regulate the SOFC temperature. In this case, the SOFC temperature is controlled by manipulating the air inlet flow rate via the bypass b_2.

2. *Reformer temperature*: The reformer temperature affects the hydrogen production and hence, the stability, the performance, and the power production level of the entire energy system. We therefore control the reformer temperature through the jacket stream flow rate via the bypass b_3.

3. *Fuel utilization*: High fuel utilization values (> 0.95) lead to fuel starvation which can damage the anode [90]. Also, low fuel utilization values reflect inefficient

operation. Motivated by this, fuel utilization is controlled in the system by manipulating the fuel inlet flow rate ($\dot{n}_{fuel}$).

4. *Cathode inlet temperature*: In order to maintain a desired operating point of the SOFC (especially the SOFC temperature), the cathode inlet temperature is also controlled. In the first configuration, it is controlled by manipulating the furnace heat duty while in the other configuration, it is controlled via the bypass (b_1).

Proportional integral (PI) controllers were implemented to realize the above control strategy. Initially, the Ziegler-Nicholds tuning technique was followed with the ultimate gain (K_u) and the ultimate period (P_u) obtained through the autotuning (ATV) method [111]. The controller parameters calculated from the above procedure resulted in aggressive control action leading to unstable closed-loop behavior (plots not included in the chapter). Therefore, we detuned the controllers to get a smoother and stable closed-loop response as well as similar settling times. The parameters obtained are presented in Table 3.8. The same controller parameters were used in both the configurations, except for the cathode inlet temperature control loop. In this loop, the same time constant but a different controller gain has been used since the manipulated variable is different in the two configurations.

Table 3.8: Controller parameters for both configurations (K: controller gain, τ_I: integral time constant)

K_{FC} (K^{-1})	$4 \cdot 10^{-3}$	$\tau_{I,FC}$ (s)	200
K_{SR} (K^{-1})	$5 \cdot 10^{-2}$	$\tau_{I,SR}$ (s)	100
K_{UF} (mol/s)	$1 \cdot 10^{-2}$	τ_{I,U_F} (s)	10
K_{Ca} (K^{-1})	$5 \cdot 10^{-4}$	$\tau_{I,Ca}$ (s)	80
K_F (W/K)	20	$\tau_{I,F}$ (s)	80

3.6.2 Closed-loop simulations

We compared the closed-loop performance of both configurations under a small and a large current step increase (similar to the steps applied in the sections 3.5.1 and 3.5.2). We also identified the operating ranges for each of the configurations. Note that the operating range here is defined as the range of achievable current for which no bypasses are saturated.

Small step increase in current

A step change from 60.3 A to 62 A in the current is applied and the evolution of the controlled variables along with their manipulated variables is presented in Figures 3.8 and 3.9. As the step in the current is applied, hydrogen consumption in the fuel cell increases, thereby causing an increase in the fuel utilization. The fuel utilization controller increases the fuel flow into the system, in order to increase the hydrogen production and hence, to decrease and bring the fuel utilization back to the set point. The increasing current also causes the SOFC temperature to rise, therefore the SOFC temperature controller reduces the bypass ratio to reduce the SOFC temperature. The increase in the fuel inlet flow leads to higher energy demand required by the reformer. According to this, we expect the controller to decrease the bypass on the reformer hot stream in order to provide more energy to the reformer. This is the case for the first configuration. However, the controller corresponding to the second configuration increases the bypass ratio. This action reveals a surplus of energy in the reformer jacket-side inlet stream compared to its nominal value. This contrasting behavior comes from the different types of heating streams used in the reformer jacket. In the first configuration, the cathode exit stream (consisting of oxygen and nitrogen) supplies the energy to the reformer. The flow rate of this stream remains almost constant (slight

decrease in oxygen flow occurs due to electrochemical reactions) during the operation. Thus the increased heating demand of the reformer causes a decrease in the bypass ratio b_3. On the other hand, the other configuration uses a mixture of anodic and cathodic streams in the reformer jacket. The flow rate of this stream changes almost in accordance with the change in the reformer inlet flow. The surplus of energy comes from the increased burner temperature.

The second configuration exhibits higher overshoots compared to the first configuration. This difference again comes from the different nature of the heating streams used in the reformer jacket. The cathode exit stream (with controlled temperature) introduces a negligible disturbance into the reformer in the first configuration, as compared to the burner temperature (with uncontrolled temperature) in the second configuration.

Large step increase in current

In section 3.5.2 we showed that the open-loop response of the first configuration is driven to instability while the second configuration remains stable under a large step increase in the current. In this section, we perform a closed-loop simulation of the above configurations under the same large disturbance (60.3 A to 70 A) and we show the capability of the proposed control scheme to stabilize the open-loop unstable system.

According to the closed-loop responses (Figures 3.10 and 3.11), the first configuration remains stable under the imposed large disturbance. Stability is achieved since the reformer temperature controller keeps the operating temperature away from the the maximum hydrogen production point (see Figure 3.3(b)). Note that both the SOFC and reformer bypasses are saturated resulting in small offsets in the SOFC and reformer temperatures. The second configuration remains stable even if the temperature bypass is saturated causing an offset in the SOFC temperature.

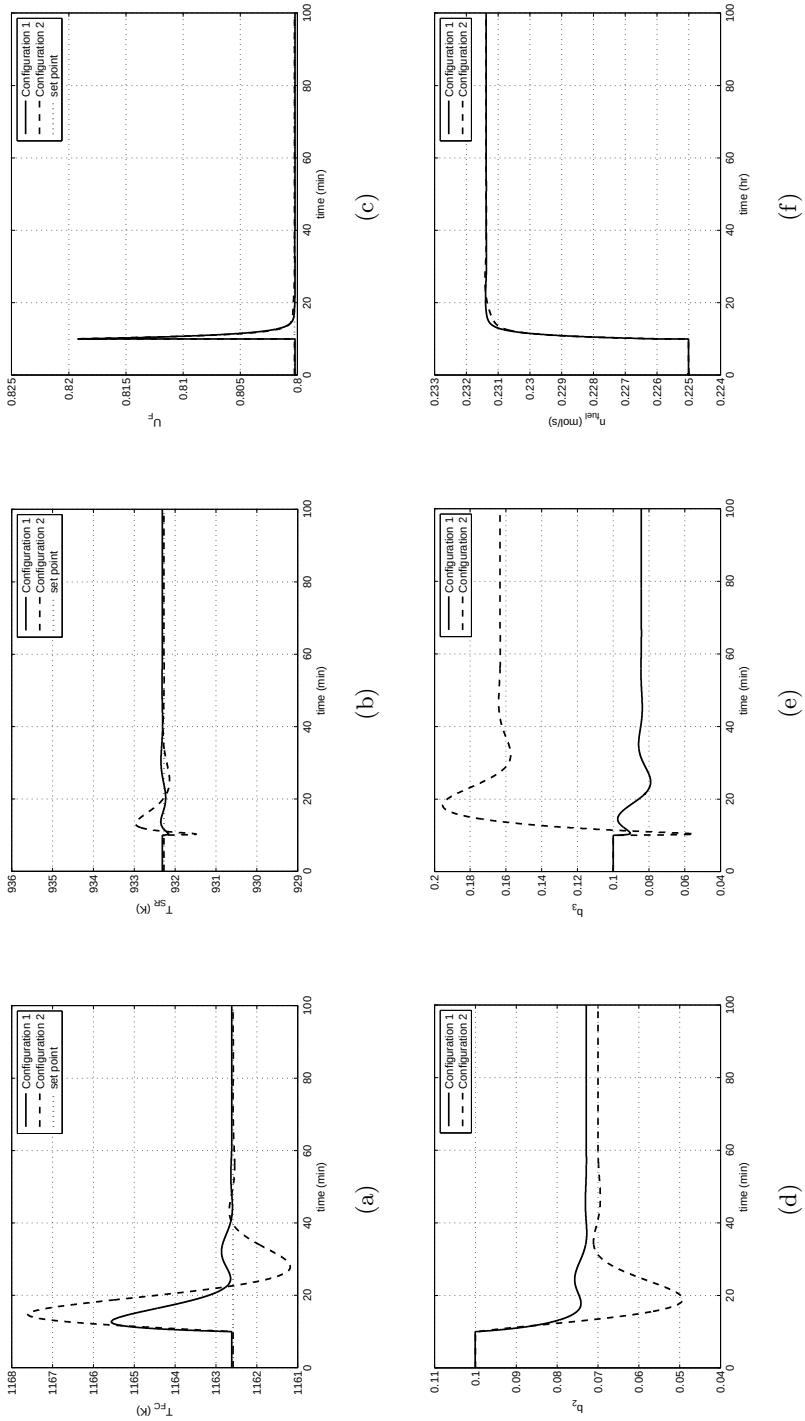

Figure 3.8: Closed-loop responses for both configurations under a current step increase from 60.3 A to 62 A.

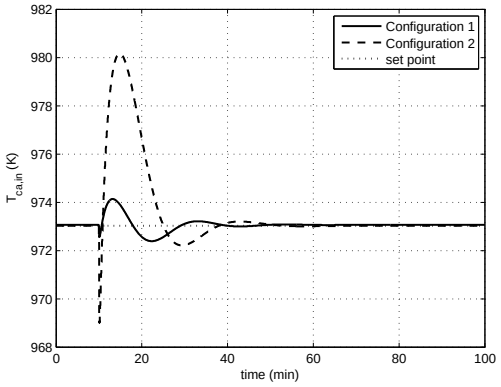

(a)

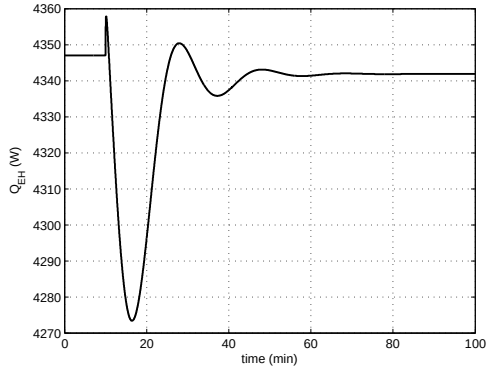

(b)

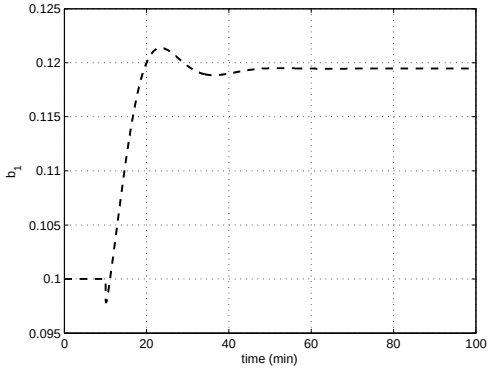

(c)

Figure 3.9: Closed-loop responses for both configurations under a current step increase from 60.3 A to 62 A.

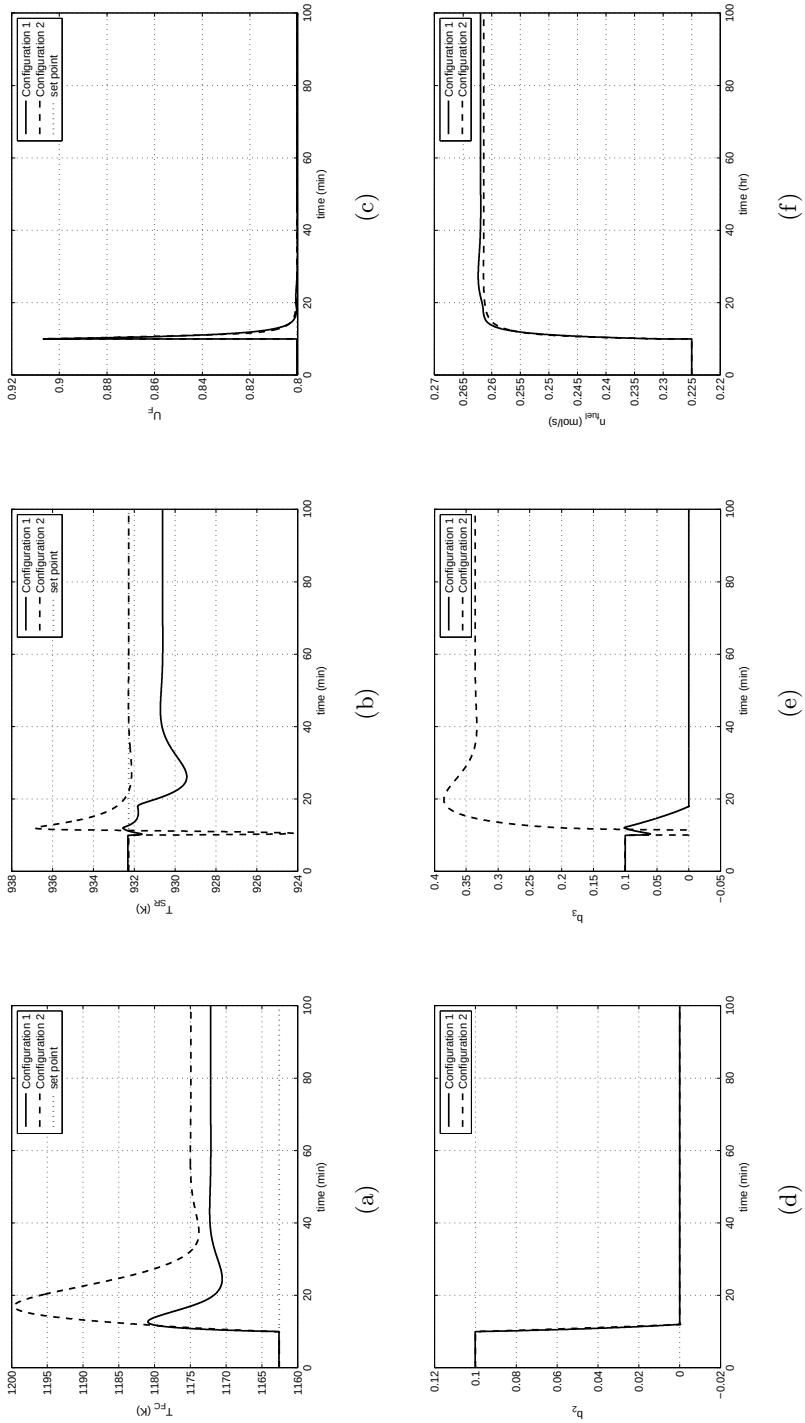

Figure 3.10: Closed-loop responses for both configurations under a current step increase from 60.3 A to 70 A

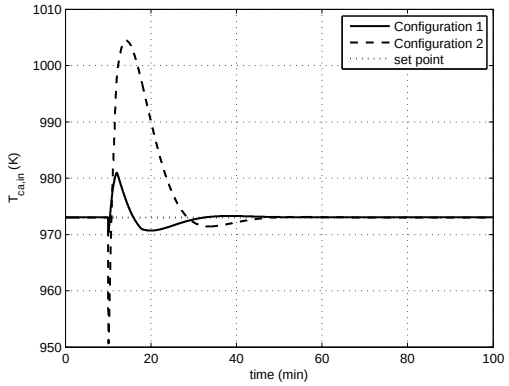

(a)

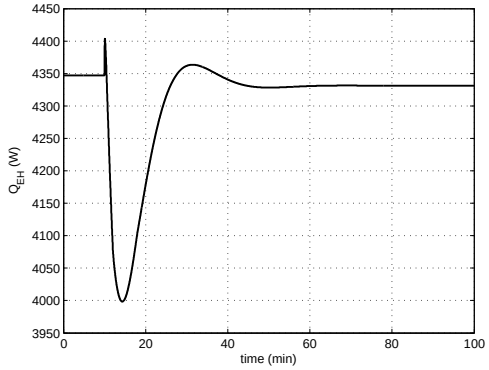

(b)

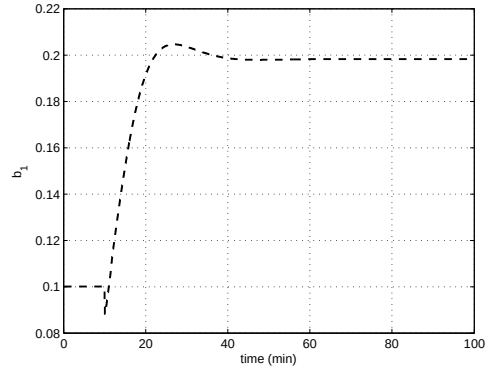

(c)

Figure 3.11: Closed-loop responses for both configurations under a current step increase from 60.3 A to 70 A

Operating range investigation

In this section, we impose positive and negative changes in current (Figure 3.12) in order to identify the operating range for both the configurations. The controlled and corresponding manipulated variables are presented in Figures 3.13 and 3.14. The first configuration shows a broader operating range (I $\leq$ 66.5 A) compared to the second configuration (58 A $\leq I <$ 66.5 A).

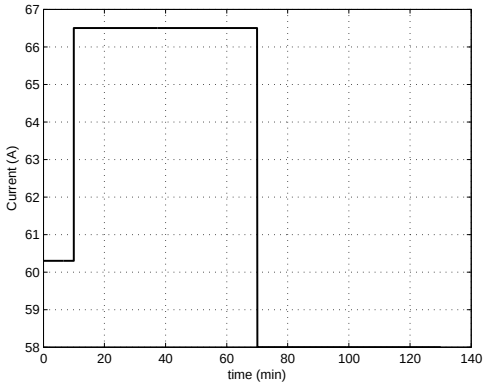

Figure 3.12: Current changes imposed to analyze the operating range for both configurations

During the first step increase in the current, the first configuration is very close to saturation while the second configuration shows a bypass (b_2) saturation (Figure 3.13(d)) resulting in an offset in the SOFC temperature. As the current decreases there is no operational and controllability limitation for the first configuration since less energy is required, and hence the controllers increase the bypasses. However, in the second configuration there is a decrease in the reformer bypass (b_3), leading to saturation (Figure 3.13(e)). Note that under saturation conditions the systems remain operable (but not controllable) showing offsets from the set point.

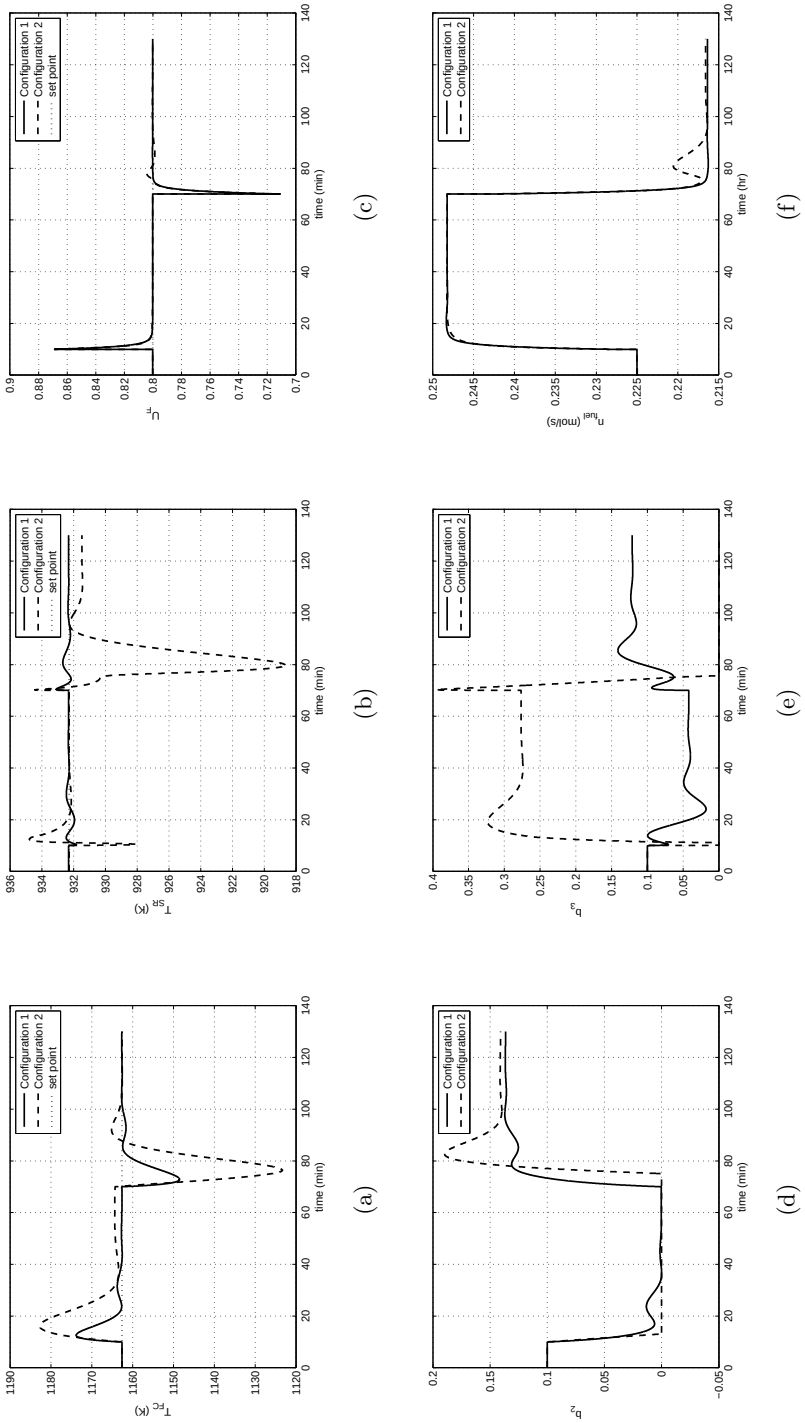

Figure 3.13: Closed-loop responses under the current step changes considered in this analysis (Figure 3.12)

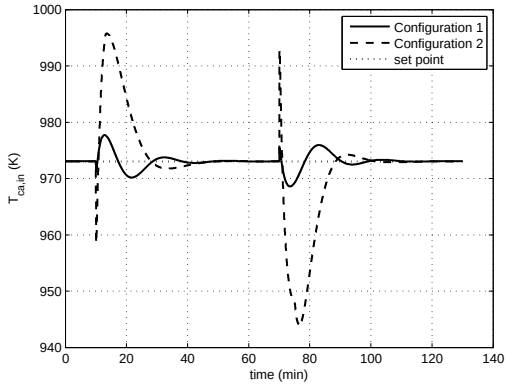

(a)

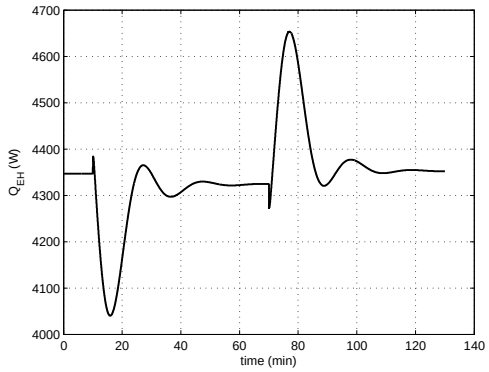

(b)

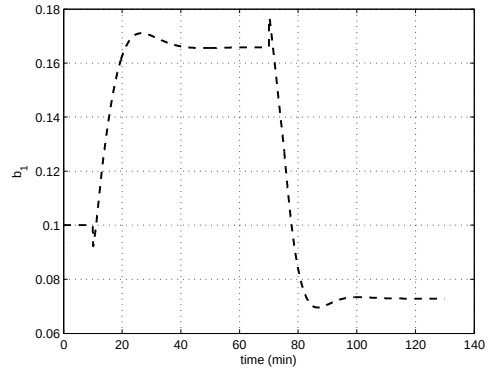

(c)

Figure 3.14: Closed-loop responses under the current step changes considered in this analysis (Figure 3.12)

3.7 Sensitivity analysis

The design of the external fuel processor is a key parameter in energy integrated SOFC systems since it affects not only the power generation through the hydrogen production, but also the energy integration through the amount of energy required by the endothermic reaction. Therefore, in this section the impact of the steam reformer design parameters on the design, operation and control of the entire energy integrated system is analyzed for configuration 1 (Figure 3.4). The selection of this configuration is motivated by the interesting dynamic features (e.g. open-loop instability) that it exhibits.

3.7.1 Impact of steam reformer design parameters on steady state design

(a) *Effect of S/C ratio on the steam reformer performance*

The steady state mathematical model representing the steam reformer is numerically solved for different operating temperatures and S/C ratios. Figure 3.15 depicts the corresponding steady states of hydrogen mole fraction at different operating temperatures and S/C ratios. The hydrogen mole fraction shows a decreasing trend as the S/C increases. It should be mentioned that higher S/C ratios also cause a rise in the total molar flow rate at the outlet of the steam reformer since the reaction equilibrium are shifted to the right hand side. For all the S/C ratios, the reformate is a stream rich in hydrogen and hence, a suitable fuel stream for SOFC systems. The effect of the steam reformer operating temperature on the hydrogen production reveals an interesting behavior. The hydrogen mole fraction shows a maximum such that the slope at a lower temperature than the maximum is higher than that at a higher temperature. This can be attributed to the interplay between a highly endothermic reaction coupled with a

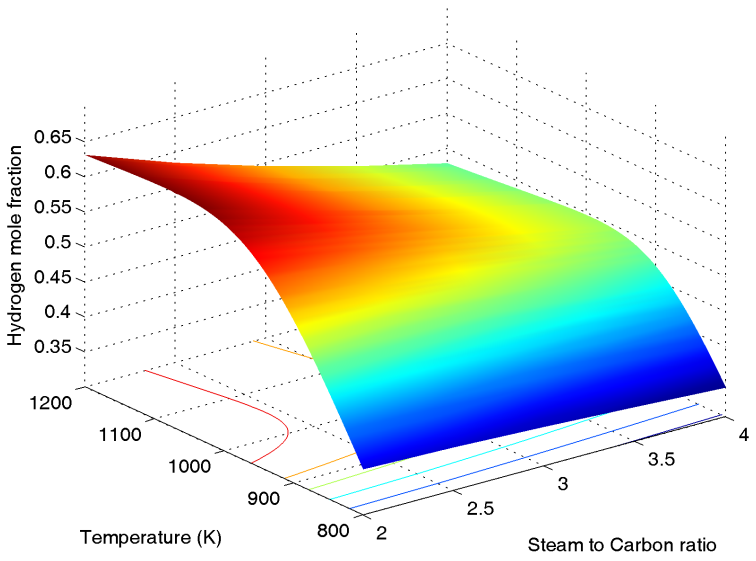

Figure 3.15: Steady states of hydrogen mole fraction as a function of the operating temperature and S/C ratio

mildly exothermic reaction. According to Figure 3.16, the temperatures for maximum hydrogen production are approximately 995, 1025 and 1080 K. In the same figure, it can be noted that the slope of the hydrogen mole fraction after the maximum point decreases as the S/C ratio decreases. Although hydrogen production shows a maximum point, methane conversion (shown in Figure 3.17) shows an increasing trend along with both the operating temperature and the S/C ratio. According to Figure 3.17, the increase in both the operating temperature and the S/C ratio favors the methane conversion since both of these parameters shift the reaction equilibrium to the right. In general, it is desired to operate the steam reformer at an operating point which provides a high methane conversion [98] and a hydrogen production close to its maximum production point.

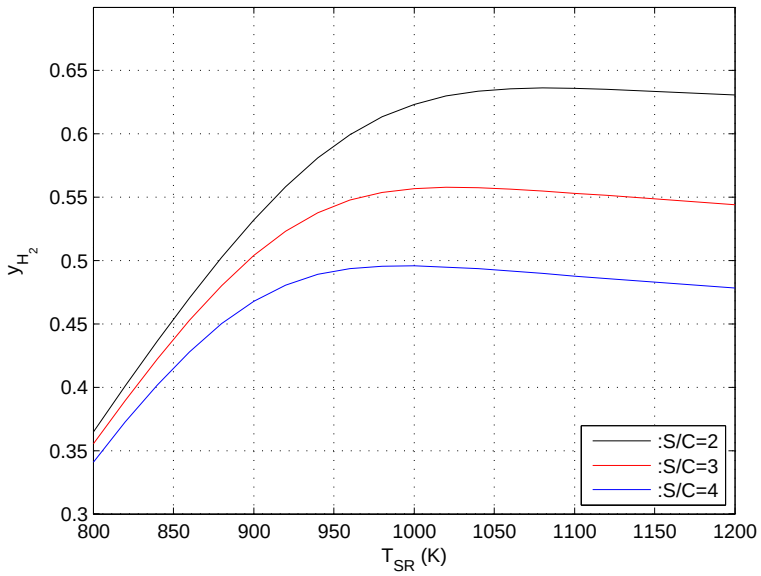

Figure 3.16: Projection of hydrogen mole fraction steady states as a function of the operating temperature at different S/C ratios

(b) *Effect of S/C ratio on the entire SOFC system steady state*

In order to provide an adequate level of comparison between the different S/C ratio cases, we maintain the same fuel utilization (U_F). To achieve a constant fuel utilization under constant current operation, the hydrogen production at the steam reformer should be fixed. Therefore, in order to provide a comparison level for the steam reformer, we chose the operating point for the steam reformer to provide same methane conversions. As a result, we compared the steady state characteristics under the same fuel utilization and the same methane conversion. In the following table (Table 3.9), the corresponding values of various process variables are tabulated.

The results show that with a decrease in the S/C ratio, more fuel and a higher operating temperature is required in order to maintain the same fuel utilization and similar methane conversion. Both the higher operating temperature and the increased

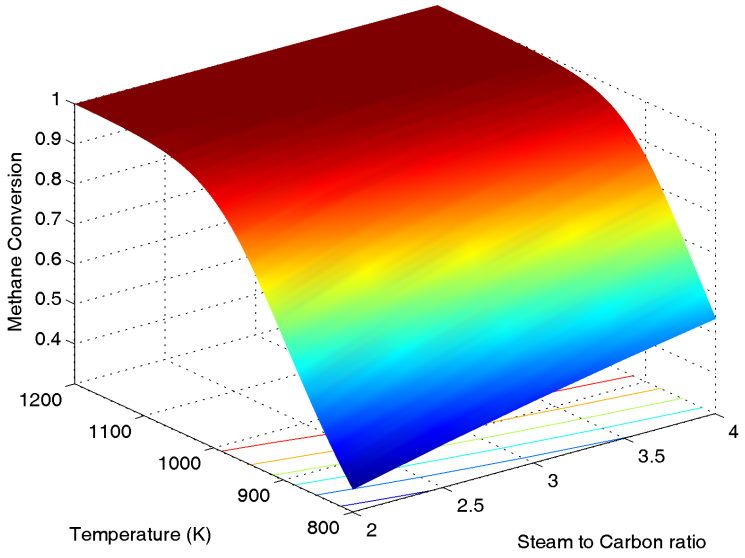

Figure 3.17: Steady states of methane conversion as a function of the operating temperature and S/C ratio

fuel flow rate are reflected directly on the amount of energy is required by the steam reformer ($\dot{Q}_{SR}$); increasing S/C ratio reduces the required amount of energy to drive the steam reforming reactions, since high S/C ratios move the equilibrium to the right as mentioned above.

Although the same fuel utilization and similar methane conversion are maintained in all the cases, the SOFC operating temperature differs slightly due to the different mixture compositions at the outlet of the steam reformer. The difference in both the reformate composition and the SOFC operating temperature leads to a deviation in the voltage produced by the SOFC.

Although the required energy of the steam reformer is inversely proportional to the S/C ratio, the total amount of energy ($\dot{Q}$) that should be supplied shows an opposite trend. The main reason for these two opposite phenomena is the rise in the amount of

Table 3.9: Steady state characteristics for different S/C ratios

	S/C = 2	S/C = 3	S/C = 4
$\dot{n}_{CH_4}$ (mol/s)	0.0494	0.0467	0.0450
U_F	0.8	0.8	0.8
T_{SR} (K)	1005.0	962.0	932.3
T_{FC} (K)	1168.3	1163.8	1162.6
V_{FC} (V)	0.7265	0.7167	0.7084
x_{CH_4} (%)	92.67	92.62	92.61
$\dot{Q}$ (kW)	2.355	3.196	4.347
$\dot{Q}_{SR}$ (kW)	11.044	10.072	9.432

water. The extra energy which is required for the vaporization of the extra amount of water dominates and hence, a higher amount of energy is required as external utility.

3.7.2 Impact of steam reformer design parameters on open–loop behavior

We now move on to the open-loop simulations under small and large current changes. It should be noted that the energy integrated SOFC system corresponding to S/C equal to three and four, can be represented by the same configuration as shown in Figure 3.4. However, for the case of the S/C equal to two, in order to design a heat exchanger network which will minimize the external utility, the hot effluent streams at the outlet of the SOFC should be thermally mixed. This requires a more complicated design which is outside the scope of this analysis.

(a) *Open–loop behavior under a small step increase in current*

A small step increase in the current is considered and the open-loop simulations for S/C=3 and S/C=4 are compared. Figure 3.18 depicts the corresponding responses.

As the current increases, more hydrogen is electrochemically oxidized inside the SOFC leading to a temperature rise (Figure 3.18(b)) and an instantaneous increase in

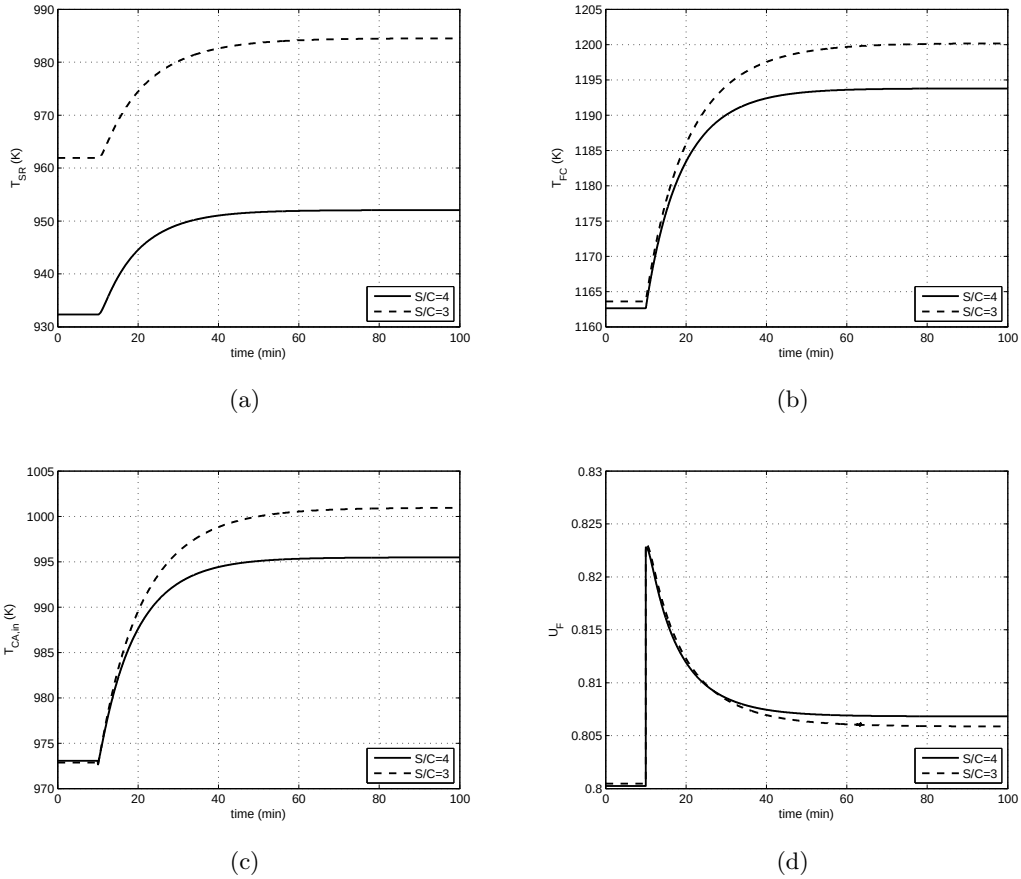

Figure 3.18: Open–loop responses under a small step in the current

the fuel utilization (Figure 3.18(d)). The higher SOFC temperature increases both the steam reformer (Figure 3.18(a)) and the cathode inlet (Figure 3.18(c)) temperatures due to the energy integration with the cathodic hot effluent stream. As a result, the higher steam reformer operating temperature leads to more hydrogen production which is captured by the gradual decrease in U_F (Figure 3.18(d)).

Note that the open-loop responses for both the S/C ratios show similar behavior. In spite of the different initial and final steady state values, we can conclude that the S/C ratio does not drastically affect the open loop dynamics of the system.

(b) *Open–loop behavior under a large step increase in current*

We next analyze the response of the entire SOFC system for a large step increase in the current. Figure 3.19 depicts the corresponding responses.

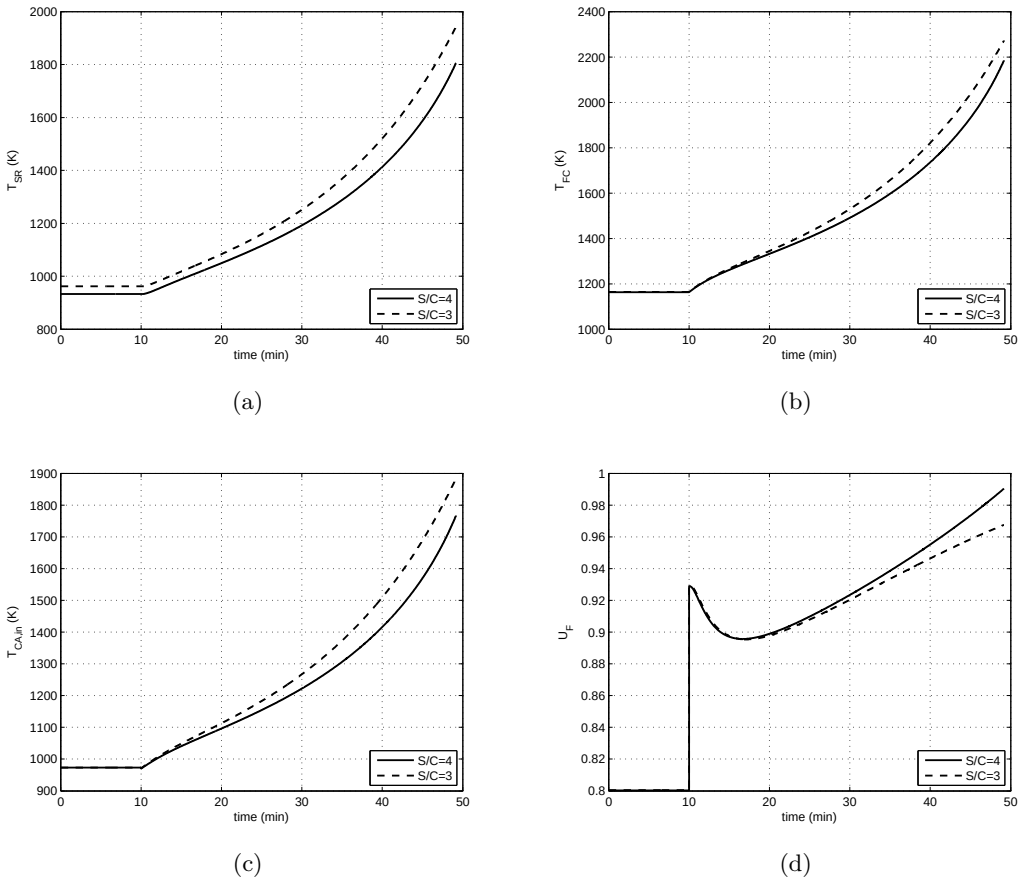

Figure 3.19: Open-loop behavior under a large step in the current

The SOFC system is driven to instability in both cases under a large step increase in the current. The large increase in the current results in a high SOFC temperature which leads to an increased steam reformer operating temperature. However, the rise in the steam reformer temperature moves its operating point to the right side of the maximum hydrogen production point (Figure 3.16) and hence, to a decreasing hydrogen

production rate. As a result, fuel utilization rises and drives the system to fuel starvation and instability conditions.

Table 3.10: Comparison of the two configurations

Characteristic	Configuration 1	Configuration 2
Design of integrated system	No pinch - extra energy is required	No pinch - surplus of energy
Open–loop dynamics	Stable (small disturbance) Unstable (large disturbance)	Stable (small disturbance) Stable (large disturbance)
Closed–loop dynamics	Smaller overshoots	Larger overshoots
Operational Range	Broader (bypass saturated for current increase)	Narrower (bypass saturated for current increase and decrease)
Enviromental Impact	No combustion No mixing of SOFC outlet streams (promising for further integration with a CO_2 capture unit)	Combustion unit (potential for NOx) Mixing of SOFC outlet streams

3.7.3 Impact of steam reformer design parameters on closed–loop behavior

Figure 3.20 depicts the closed-loop responses along with the manipulated variables for the large step in the current. It can be observed that there are operational limitations

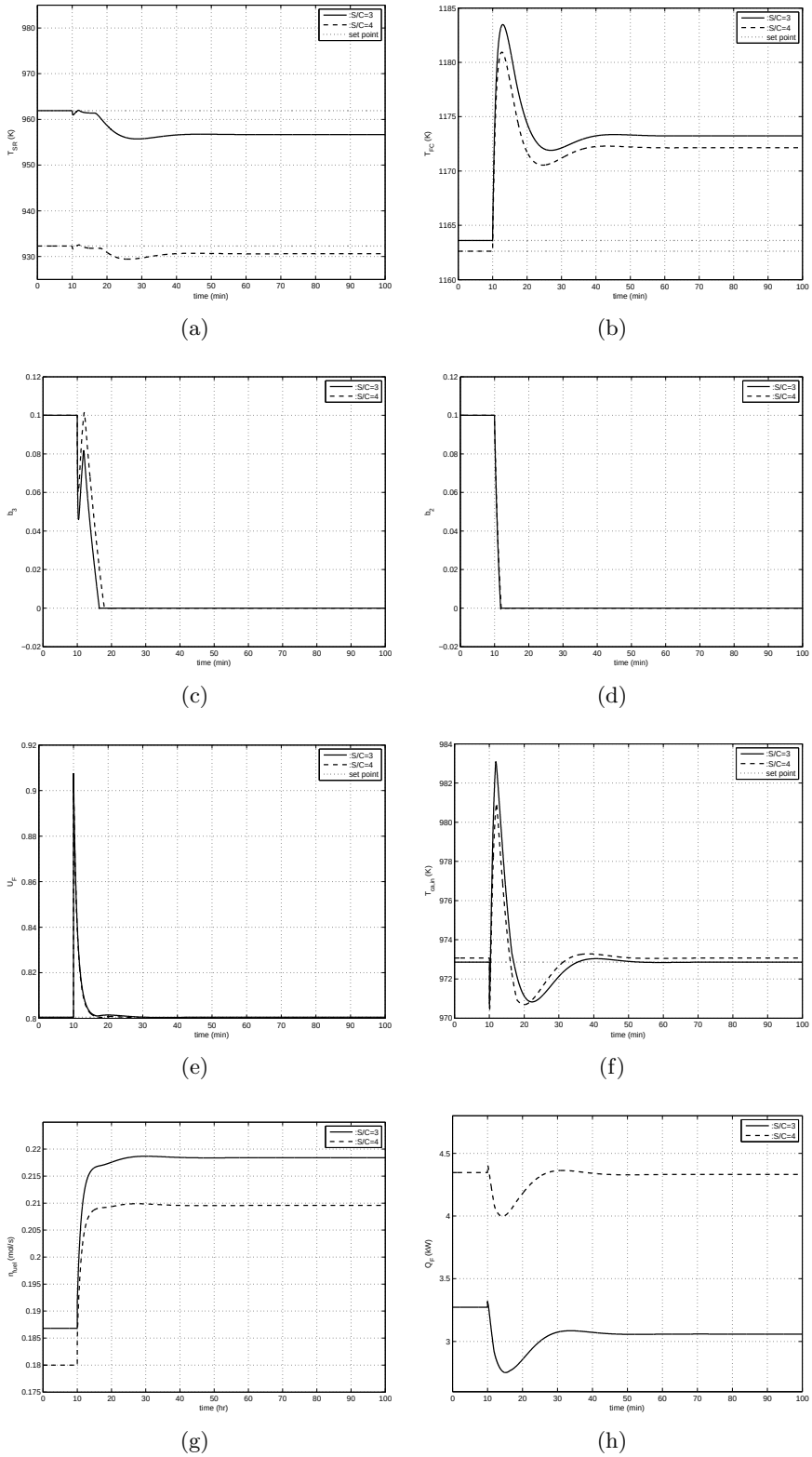

Figure 3.20: Closed–loop behavior under a large step in the current

in both systems due to the saturation of bypasses b_2 and b_3. It should be mentioned that these limitations are due to the system design and not due to the controller tuning.

Furthermore, the closed-loop responses reveal a similar behavior in both cases. This is expected since both systems are designed to operate at the same fuel utilization and hence, the effect of the SOFC in the entire system is similar in both cases leading to almost similar closed-loop responses.

3.8 Discussion

Let us now compile the various similarities and contrasting features exhibited by these two configurations. Table 3.8 summarizes and compares the major characteristics of these configurations.

- *Design of integrated system*: Both configurations do not show a pinch point. Additional energy is required (and supplied via a furnace) in the first configuration while energy is available for further integration in the second configuration. Both configurations use seven process-to-process heat exchangers.

- *Open-loop dynamics*: Both configurations are stable for small disturbances in current. However, the first configuration is driven to instability for a large disturbance in current, whereas the second configuration remains stable.

- *Closed-loop dynamics*: The proposed control scheme is capable of stabilizing the open-loop unstable configuration. Additionally, the first configuration shows smaller overshoots compared to the second configuration (for the same controller parameters).

- *Operational range*: The first configuration has a broader operational range compared to the second configuration. More precisely, the first configuration shows a

limitation (due to bypass saturation) at higher current, while the second configuration shows limitations for both the increase and the decrease in the current.

- *Environmental impact*: The first configuration is less amenable to NOx production (due to the absence of a combustion unit). Moreover, this configuration looks promising for further integration with a carbon dioxide capture unit as the anodic (CH_4, H_2O, CO_2, CO and H_2) stream is not mixed with the cathodic (O_2 and N_2) stream [89].

Nomenclature

Symbol	Definition
Capital letters	
R	Universal gas constant
T	Temperature
F	Faraday constant
V_{FC}	Voltage of single cell
I_o	Exchange apparent current
I	Current
R_i	Resistance of each compartment
I_L	Limiting current
N	Number of cells in the SOFC stack
V	Output voltage
P	Output power
Cp_i	Heat capacity of component
V_i	Volume of each compartment
P_i	Operating pressure of each process
ΔH_i^{rxn}	Heat of reaction
$\dot{Q}_i$	Enthalpy flow
U	Overall heat transfer coefficient
A	Area
ΔT_{LM}	Logarithmic mean temperature difference
U_F	Fuel utilization
L	Length

W	Width
Small letters	
n	Number of transferred electrons
p_i	Partial pressure of each species
$\dot{n}_i$	Molar flow rate
m	Mass
r_i	Reaction rate
Greek letters	
η	Number of transferred electrons
α	Charge transfer coefficient
ρ	Density
ε	Void fraction
τ	Thickness
Subscripts	
FC	Fuel cell
OCV	Open-circuit voltage
act	Activation
ohm	Ohmic
$conc$	Concentration
an	Anode
el	Electrolyte
ca	Cathode
int	Interconnect

$fuel$	Fuel stream
air	Air stream
SR	Steam reformer
cat	Catalyst

CHAPTER 4

Thermal management of Water Gas Shift Membrane Reactors for simultaneous hydrogen production and carbon capture

Overview: This chapter focuses on the thermal management of a hydrogen-selective low temperature water gas shift (WGS) membrane reactor for simultaneous high purity hydrogen production and carbon capture. A mathematical model of the reactor is developed consisting of a set of first–order hyperbolic PDEs. Open–loop simulations under a step change in the syngas inlet composition reveal the existence of large temperature gradients along the reactor. A control strategy is proposed whereby multiple distributed cooling zones are placed across the reaction zone in order to regulate the temperature profile. A nonlinear distributed controller is derived and its performance is evaluated for disturbance rejection and set point tracking case studies.

4.1 Introduction

In Chapter 1 the need for highly efficient power plants, along with carbon capture technologies, was discussed in order to mitigate the environmental impact from the extensive use of fossil fuels for power generation. Typical examples include the Integrated Gasification Combined Cycle (IGCC) plants for clean coal power generation [112, 113, 114, 115] and the Combined Heat and Power (CHP) plants integrated with fuel cells for hydrocarbon-based power generation [116, 117, 24, 118, 119, 120]. Such plants typically involve the production of hydrogen which generates power either through a gas turbine or a fuel cell [82].

Coal-, natural gas-, or biomass-derived syngas produces hydrogen through the moderately exothermic and equilibrium limited water-gas-shift (WGS) reaction (3.15). The equilibrium of the WGS reaction is favored at low temperatures and is unaffected by the operating pressure. In industrial–scale process units, high pressure syngas is upgraded to hydrogen and carbon dioxide in two stages [121]. In the first stage, a high temperature (HT–WGS) packed-bed reactor loaded with iron/chromium (Fe/Cr) catalyst is used to exploit the fast kinetic rates. The outlet stream of the HT–WGS reactor is cooled and fed to a low temperature (LT–WGS) packed-bed reactor loaded with copper/zinc (Cu/Zn) catalyst where the equilibrium is favorable leading to a high CO conversion (see Figure 4.1). The high pressure and concentration of the carbon dioxide at the outlet of the LT–WGS reactor allows for pre-combustion carbon capture, providing advantages in terms of sizing and capital cost of the carbon capture unit [122]. Existing mature technologies available for carbon capture include chemical absorption processes (amine-based and hot carbonate systems) and physical solvent processes (Rectisol^{TM}, Selexol^{TM}) [123]. Although physical solvent processes are more energy efficient than chemical absorption processes [122], both technologies require large energy inputs for solvent regeneration.

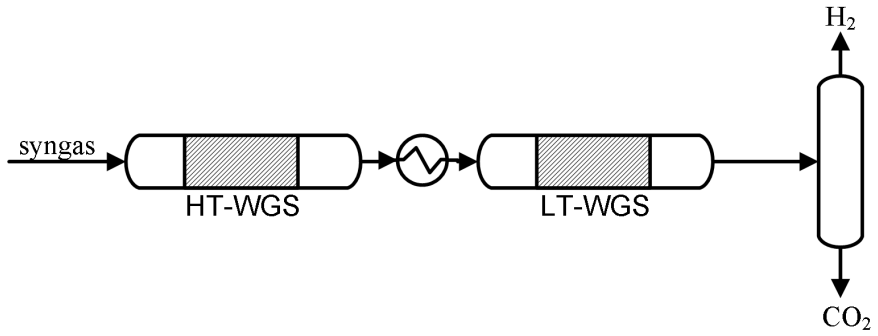

Figure 4.1: Conventional process configuration for high and low temperature packed–bed WGS reactors including carbon capture

An alternative technology, which has attracted a lot of interest [124, 125, 126], allows for process intensification by replacing the conventional packed-bed WGS reactors and its associated carbon capture unit with a WGS membrane reactor.

WGS membrane reactors enable simultaneous high–purity hydrogen production and carbon capture. The combination of production and separation of hydrogen in one unit can result in substantial improvement in both performance and economics of the entire plant. However, several studies have demonstrated the risk associated with hot spot formation which could be detrimental for both the catalyst [121, 127, 128] and the membrane stability [129, 127, 128].

In this study, we focus on the thermal management of a hydrogen–selective (zeolite-based) WGS membrane reactor. A dynamic distributed model is developed based on first principles. A control strategy is proposed and a model–based controller is derived to regulate the temperature profile of the WGS membrane reactor and suppress thermal gradients. A case study demonstrates the performance of the proposed control strategy. In addition, the performance of the model–based controller is compared with that of a classical PI controller.

The chapter is structured as follows: the next section (Section 4.2) includes a comprehensive literature review on modeling and thermal management of WGS membrane reactors. Results associated with our previous work on modeling, optimization and control of WGS membrane reactors are also reported. The mathematical model for the reactor considered is presented in Section 4.3. Open–loop simulations are shown in Section 4.4 with the dynamic behavior of the WGS membrane reactor being analyzed under different operating conditions. The proposed control strategy is presented in Section 4.5 and its performance is evaluated under a case study scenario.

4.2 Background

A membrane reactor typically consists of two concentric cylinders separated by a selective membrane, one of which acts as a reaction zone and the other as a permeation zone. Two different design configurations have been proposed in the literature[130]. In the first design, the reaction takes place in the tube and the membrane is placed at the outer wall of the reaction zone [131, 132, 133] (see Figure 4.2(a)), while in the second design, the reaction zone is in the shell and the membrane placed at the outer wall of the permeation zone [134, 126] (see Figure 4.2(b)). For both designs, syngas is fed to the reaction zone where it is upgraded to hydrogen and carbon dioxide in the presence of steam. Sweep gas (either steam or nitrogen) flows through the permeation zone either co–currently or counter–currently to the reaction zone flow, allowing for the recovery of the permeated hydrogen. In terms of performance, it has been shown that the counter–current flow configuration is more favorable than the corresponding co–current one [134, 135, 136]. This is attributed to the higher partial pressure difference of hydrogen developed across the membrane which results in a higher permeation

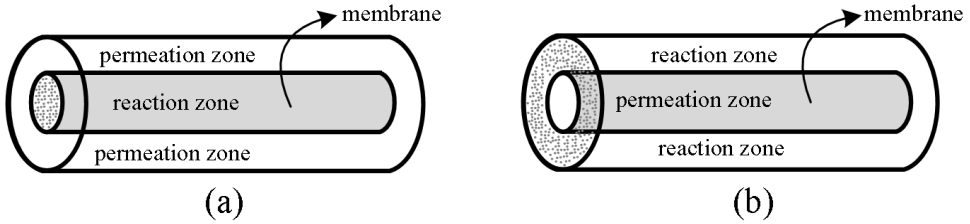

Figure 4.2: Different designs for a membrane reactor: (a) reaction takes place in the tube with the membrane placed at its outer wall (b) reaction takes place in the shell and membrane placed at the outer wall of the permeation zone

rate. The simultaneous reaction/separation in one process unit shifts the equilibrium-limited WGS reaction towards higher conversion and increases the residence time of the reactants across the reaction zone [137], leading to a smaller reactor and less required mass of catalyst for a given CO conversion. Generally, a hydrogen–selective membrane is used in WGS membrane reactors. However, the use of a CO_2–selective membrane might be more beneficial when the concentration of CO_2 is higher at the inlet of the membrane reactor compared to hydrogen [131]. Several types of materials for hydrogen–selective membranes have been proposed [138], with Pd–based membranes considered suitable when high–purity hydrogen is required. Despite their infinite selectivity for hydrogen, major drawbacks of Pd–based membranes include high capital cost and hydrogen embrittlement [139]. A promising alternative involves the use of zeolite–based membranes which show the potential for high fluxes, relatively high selectivities and good hydrothermal stability [136]. More information about different types of hydrogen–selective membranes and their features can be found in the literature [138, 136].

The permeation rate across the membrane is a function of the partial pressure difference between the reaction and permeation zone for the permeating component of interest. Therefore, a high operating pressure in the reaction zone enhances the performance of the reactor. This attribute renders the integration of membrane reactors with coal gasification or steam reforming (SR) units a promising alternative for pre–combustion

carbon capture. Several studies have analyzed the integration of WGS membrane reactors with either IGCC [140, 141, 142] or fuel cell power plants [143, 144, 145].

In terms of modeling, a large variety of mathematical models of different complexity have been developed. The complexity is determined based on the application and the scope of the individual study, and can range from steady–state isothermal one-dimensional to full computational fluid dynamics models. Isothermal operation could be considered a valid assumption for lab–scale modules, however this assumption is insufficient for larger–scale membrane reactors. Furthermore, it has been demonstrated that the assumption of isothermal operation leads to an overestimation of the reactor's performance [127, 146]. In addition to this, several studies have mentioned the existence of large temperature gradients which involve potential risks for both the catalyst and the membrane stability as mentioned above (Section 4.1). Therefore, nonisothermal models are essential for risk assessment and performance prediction. Different strategies have been proposed for thermal management of packed–bed reactors exhibiting large temperature gradients. These alternatives include catalyst dilution with inert pellets [128, 147, 133], side–stream feed [128, 129, 148] and steam injection [127]. Catalyst dilution has been shown to be an effective way to mitigate the hot–spot along the length of the reactor [147, 127] but unable to suppress it completely and enforce an approximately uniform temperature profile. Side–stream feed of a reactant is only applicable in autothermal (e.g. SR) membrane reactors where the flow rate of oxygen controls the fuel oxidation (e.g. methane) and hence, the heat produced by the oxidation reaction. As a result, this strategy is suitable only in autothermal membrane reactors involving highly endothermic reactions (e.g. SR [129] or Methanol Reforming [148]) along with exothermic reactions (e.g. Partial Oxidation). Steam injection constitutes an alternative option for reducing the temperature in the reaction zone. Although this strategy is applicable to WGS membrane reactors, it results in a decreased hydrogen

partial pressure and thus, deteriorates the performance of the reactor. In addition to this, large amounts of steam in the reaction zone could reduce significantly the residence time in the reaction zone leading to a reduced CO conversion [127]. Furthermore, large amount of steam injection could also result in increased operating cost. Although these alternatives could be beneficial in specific applications and operating conditions, they cannot be generalized as thermal management strategies to any membrane reactor application. A general control strategy for thermal management of membrane reactors, which is capable of enforcing an almost uniform temperature profile, would therefore be valuable.

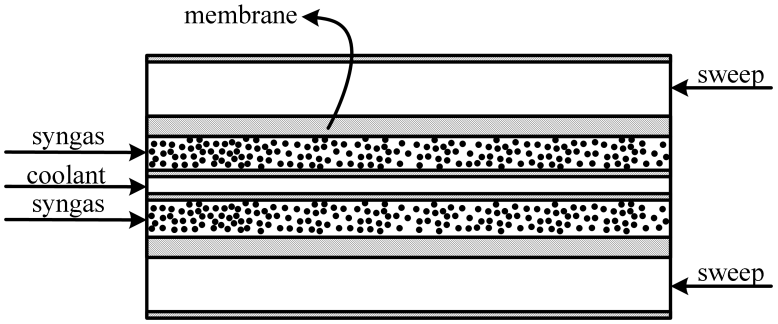

Figure 4.3: Thermal management strategy considered in previous work [6]

In our previous work [6], we proposed a control strategy for suppressing the hot spots and ensure the operational feasibility of a high–temperature WGS membrane reactor of the same design as in Figure 4.2(a). According to this reactor's design, the membrane was placed along the entire length of the reaction zone and an inner cooling zone was used for temperature control (see Figure 4.3). This design however has limited controllability owing to the single control actuation acting at the entrance of the reactor. Also, there have been several studies which propose the use of a pre–shift zone with the membrane reactor [149]. This option results in a lower concentration of reactants at the entrance of the reaction zone reducing the risk for excessively large temperature gradients at the

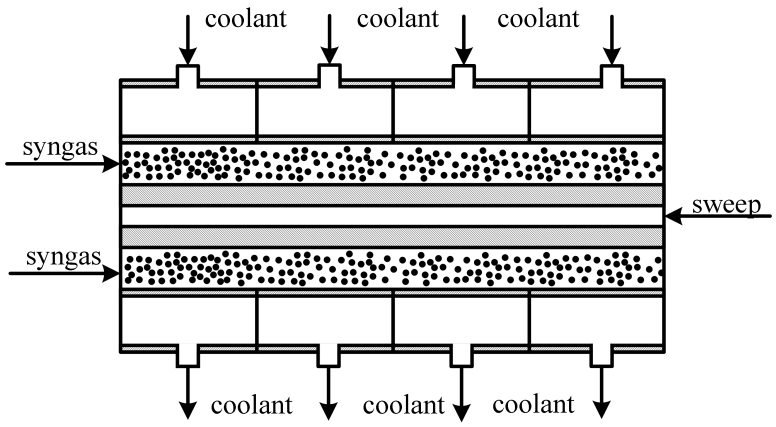

Figure 4.4: Thermal management strategy considered in this work

entrance of the reactor. In addition, the placement of a pre–shift zone upstream of the membrane reactor eliminates any back–permeation of hydrogen at the entrance of the reactor which occurs during counter–current operation [134]. It also leads to a reduced membrane area with significant benefits in capital cost. The latter was demonstrated in our recent study [136] where an optimization problem was formulated based on a one-dimensional steady–state, isothermal model in order to identify the optimal placement of catalyst and membrane along the length of the reactor.

Motivated by this, the process configuration considered here consists of a pre–shift unit followed by a low–temperature membrane reactor. We focus on the thermal management of the low–temperature WGS membrane reactor with the membrane placed at the outer wall of the permeation zone (see Figure 4.2(b)). This design allows for distributed cooling of the reaction zone as in conventional non-adiabatic plug flow reactors [150] (see Figure 4.4).

4.3 Mathematical model

A WGS membrane reactor is a classic reaction–diffusion chemical system which includes flow and reaction in the axial direction and diffusion in the radial direction. Although two-dimensional models are preferred especially in industrial–scale units in order to capture the physical phenomena in both directions, they are quite complex and computationally intensive. Furthermore, one-dimensional models have been shown to be reliable for a overall assessment of the membrane reactor and more computationally efficient [127]. Especially for small–scale (e.g. lab/pilot) membrane reactors with relatively high length to diameter ratio (L/D) it is expected that the variations in the radial direction would not be significant.

In this study, we develop a one-dimensional mathematical model for a WGS membrane reactor with a sufficiently large L/D ratio (> 10). In order to maximize the driving force between the reaction and the permeation zone and hence to enhance the membrane's performance, a counter–current flow is considered for the permeation zone. Steam is used as the sweep gas. Especially in zeolite–based membrane reactors, the use of steam favors the performance of the reactor since it permeates to the reaction zone, shifting the equilibrium further towards higher CO conversion. The developed model includes the following assumptions: a) all gases are considered ideal; b) constant operating pressure is assumed in all compartments; c) axial dispersion is neglected; d) uniform catalyst distribution is assumed with a constant porosity along the entire length of the membrane reactor; and e) velocity dynamics are neglected. According to these, the mass and energy balances in each compartment are described by a set of first order hyperbolic PDEs of the following form:

Species balances in reaction and permeation zones:

$$\frac{\partial C_{jn+i}}{\partial t} = -1^{(j+1)}\left(-\frac{\partial F_{jn+i}}{\partial V_j} + J_i + j{\cdot}R_{wgs}\right) \tag{4.1}$$

$$i = (\mathrm{CO},\ \mathrm{H_2O},\ \mathrm{CO_2},\ \mathrm{H_2},\ \mathrm{N_2})$$

$$j = \begin{cases} 1, \text{ for the reaction zone} \\ 0, \text{ for the permeation zone} \end{cases}$$

$$C_{jn+i} = \frac{F_{jn+i}}{Q_j}$$

$$J_i = \begin{cases} \frac{\pi d_t}{A_s} Q_{m_i}\left(P_{i,s} - P_{i,t}\right) \text{ for j=1} \\ \frac{\pi d_t}{A_t} Q_{m_i}\left(P_{i,s} - P_{i,t}\right) \text{ for j=0} \end{cases}$$

$$R_{wgs} = -\nu_i\ k(T_s)\left(P_s^{(0.5-P_s/500)}\right)\left(y_{s,CO}y_{s,H_2O} - \frac{y_{s,CO_2}y_{s,H_2}}{K_{eq}(T_s)}\right)\left(\frac{m_{cat}}{V_s}\right) \tag{4.2}$$

$$k_{wgs}(T_s) = 82.2\ \exp\left(\frac{-47400}{RT_s}\right)$$

$$K_{eq}(T_s) = \exp\left(\frac{4577.8}{T_s} - 4.33\right)$$

where C, F, T, V and Q refer to the concentration (mol/m^3), molar flowrate (mol/s), temperature (K), volume (m^3) and volumetric flowrate (m^3/s) respectively. J corresponds to the molar flux across the membrane (mol/m^3/s), R is the universal gas constant (J/mol/K), A is the cross–sectional area of its compartment (m^2) and R_{wgs} represents the WGS reaction rate (mol/m^3/s) with k_{wgs} and K_{eq} its associated kinetic and equilibrium constants. In the molar flux expression, the variables Q_m and P_i refer to the species permeance through the membrane (mol/s/m^2/atm) and the species partial pressures (atm). The subscripts i, n, s, and t denote the species components, the total number of species components, the reaction zone and the permeation zone.

The binary parameter j determines the compartment of the membrane reactor. In the reaction rate expression (equation 4.2), m_{cat} is the mass of the catalyst (kg), ν_i is the stoichiometric coefficient for each individual species and the term $P^{(0.5-P/500)}$ refers to a correction factor for high pressure operating conditions [121].

Energy balances for both reaction and permeation zones:

$$\frac{\partial H_j}{\partial t} = -1^{(j+1)} \left(-\frac{\partial \left(F_j \bar{M}w_j \tilde{H}_j \right)}{\partial V_j} - \frac{\dot{Q}_{diff}}{A_j} - \frac{\dot{Q}_{mem}}{V_j} \right) - j \cdot \frac{\dot{Q}_{cool,z}}{V_j} \tag{4.3}$$

where H, $\bar{M}w$, $\tilde{H}$ denote the enthalpy (J), the mixture molecular weight (kg/mol) and the mass specific enthalpy (J/kg). The energy flows due to the diffusion and the heat conduction through the membrane are calculated based on the following equations:

$$\dot{Q}_{diff} = \left(\sum_{i=1}^{n} J_i M w_i \right) \tilde{H}_j$$

$$\dot{Q}_{mem} = U_{mem} A_t (T_s(z) - T_t(z))$$

The mass specific enthalpy $\tilde{H}_j$ and enthalpy H_j are evaluated based on the following equations:

$$\tilde{H}_j = \sum_{i=1}^{n} w_i \left(\Delta H^{\circ}_{f,i} + \int_{T_{ref}}^{T} C_{pi}(\tilde{T}) d\tilde{T} \right)$$

$$H_j = \bar{\rho}_j \cdot \tilde{H}_j$$

where $\Delta H^{\circ}_{f,i}$ refers to the standard enthalpy of formation of each component (J/kg), $\bar{\rho}$ is the density of the mixture (kg/m^3), w_i corresponds to the mass fraction of each component and $C_{pi}(T)$ denotes the heat capacity of each component (J/kg/K) as a

function of the temperature of the following form:

$$C_{pi}(T) = \alpha_{o,i} + \alpha_{1,i}T^{-1} + \alpha_{2,i}T + \alpha_{3,i}\ln T \tag{4.4}$$

All physical properties are calculated using the IPPFO property package which is included in gPROMS Modelbuilder [151].

The distributed cooling zones were modeled assuming well–mixed zones of constant volume [152] described by a set of ODEs of the following form:

$$\frac{dH_{cool,z}}{dt} = \left(F^{in}_{cool,z} Mw^{in}_{cool,z} \tilde{H}^{in}_{cool,z} - F_{cool,z} Mw_{cool,z} \tilde{H}_{cool,z}\right) + \dot{Q}_{cool,z} \tag{4.5}$$

where the subscript z refers to each cooling zone and the heat transfer flow associated with each cooling zone is evaluated using the following equation:

$$\dot{Q}_{cool,z} = U_{cool,z}\pi d_s \int_{l_{i,z}}^{l_{f,z}} (T_s(z) - T_{cool,z})dz$$

where $l_{i,z}$ and $l_{f,z}$ refer to the initial and final length of each individual cooling zone respectively.

The following boundary and initial conditions are considered for the reaction and permeation zones:

$$C_{s,i}(0,t) = C^{in}_{s,i} \quad \forall\ t,\ C_{s,i}(z,0) = C^{0}_{s,i} \quad \forall\ z$$
$$C_{t,i}(L,t) = C^{in}_{t,i} \quad \forall\ t,\ C_{t,i}(z,0) = C^{0}_{t,i} \quad \forall\ z$$
$$T_{s}(0,t) = T^{in}_{s} \quad \forall\ t,\ T_{s}(z,0) = T^{0}_{s} \quad \forall\ z$$
$$T_{t}(0,t) = T^{in}_{t} \quad \forall\ t,\ T_{t}(z,0) = T^{0}_{t} \quad \forall\ z$$

For the cooling zone, the mathematical model consists of a set of ODEs, and therefore

only initial conditions are considered:

$$T_{cool,z}(0) = T^{0}_{cool,z}$$

The developed mathematical model was simulated using the gPROMS Modelbuilder v3.6 simulation platform using the method of lines to approximate the spatial derivatives. Specifically, the backward finite difference method was used in the reaction and cooling zones and the forward finite difference method was used in the permeation zone. A uniform mesh of 100 grid points was used in each compartment. The time integration of the discretized set of PDEs was performed using the SRADAU solver which is a variable step numerical method suitable for discretized PDAE systems. All simulations were performed in a 64–bit Windows 7 CPU equipped with a i7 processor at 2.67 GHz and 8GB of RAM.

4.4 Open–loop simulations

As mentioned above, a configuration including a pre–shift zone followed by a low temperature membrane reactor has been identified as the optimal design in terms of membrane capital cost [136]. According to this design, a typical syngas stream is fed to the pre–shift zone where it is assumed that 80% carbon monoxide conversion is achieved. Afterwards, the pre–shifted stream enters the low temperature WGS membrane reactor where a high carbon monoxide conversion is achieved ($> 98\%$) and high purity hydrogen is produced. The composition for both the syngas and the pre–shifted streams is shown in the following table (Table 4.1).

In order to account for the large amount of heat released at the inlet of the reactor, instead of placing equi-spaced cooling zones along the reactor (see Figure 4.4) we placed three cooling zones spaced as follows: 0–0.05 m, 0.05–0.10 m and 0.10–0.20 m (see Figure

4.5) to ensure high rate of heat removal closer to the reactor entrance.

No cooling zone was placed at the last part of the reactor since the reaction rate is much lower in this part and we expect that the small cooling contribution from the permeation zone will be sufficient to prevent any temperature increase in this section. This was indeed verified by the simulations (see Figure 4.7). The nominal values

Table 4.1: Composition of syngas and pre–shifted streams

Stream	**Compositions (%)**				
	CO	**H_2O**	**CO_2**	**H_2**	**N_2**
Syngas[136]	24.43	48.86	5.68	19.33	1.70
Pre-shifted Syngas	4.89	29.32	25.22	38.87	1.70

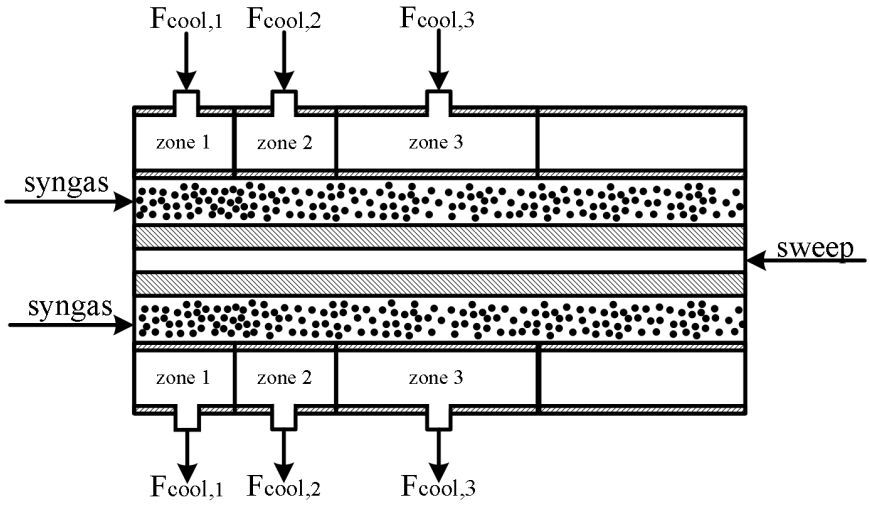

Figure 4.5: Distributed cooling zone placement for increased heat removal from the reaction zone

for the cooling zone flowrates were chosen to obtain an almost uniform temperature distribution which has been shown to be beneficial both in terms of performance and safety aspects. The parameters and inlet conditions used in the simulations are given in Tables 4.2 and 4.3.

We proceed to examine the open–loop behavior of the WGS membrane reactor under

Table 4.2: Inlet Conditions used in simulations

Variable	**Value**	**Variable**	**Value**
F_s (cm^3/min)	400	P_s (atm)	47.6
F_t (cm^3/min)	800	P_t (atm)	25.8
F_{c_1} (cm^3/min)	275	P_c (atm)	10 (for each zone)
F_{c_2} (cm^3/min)	90	$T_{s_{in}}$ (K)	500
F_{c_3} (cm^3/min)	60	$T_{t_{in}}$ (K)	500
		$T_{c_{in}}$ (K)	298 (for each zone)

Table 4.3: Parameters used in simulations

Parameter	**Value**	**Parameter**	**Value**
d_s (10^{-2} m)	2.88	U_c (W/m^2)	30 (for each zone)
d_t (10^{-2} m)	2.28	$Q_{m_{H_2}}$ ($mol/s/m^2/atm$)	$2{\cdot}10^{-2}$
d_c (10^{-2} m)	4.00 (for each zone)	$\alpha_{H_2/\text{all}}$ (–)	10^4
L (10^{-2} m)	30	α_{H_2/H_2O} (–)	100
U_{mem} (W/m^2)	6		

changes in the syngas inlet composition. This is a typical upstream disturbance which could be attributed to changes in the performance of the pre–shift zone, caused for example by changes in throughput. Specifically, we apply a step decrease (10%) in the carbon monoxide conversion in the pre–shift zone (from 80% to 70%). Figure 4.6 shows the open–loop responses of the reaction zone temperature at various positions across the reaction zone, while Figure 4.7 depicts the temperature distribution at both the nominal and the new attained steady–state.

As can be seen in Figure 4.6, the temperature rises across the length of the reaction zone. As the performance of the pre–shift zone drops, the concentration of the reactants increases at the inlet of the membrane reactor leading to a higher reaction rate. As a result, most of the heat is released at the inlet of the reactor which leads to steeper temperature gradients when compared to the remaining part of the reactor. The entrance of the reaction zone is therefore very important in terms of thermal management.

Furthermore, spatial gradients develop along the reactor which persist, leading to

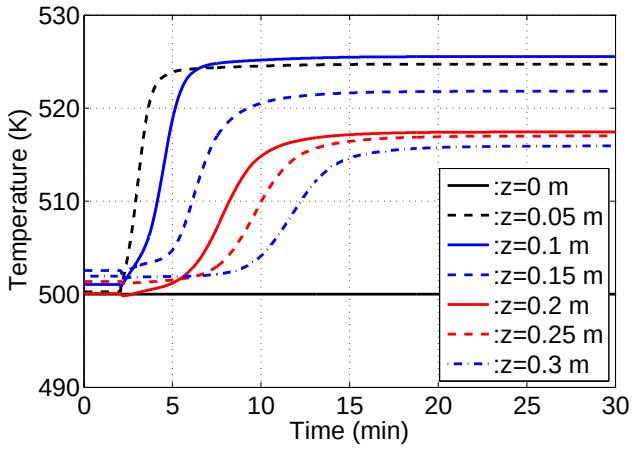

Figure 4.6: Reaction zone temperature response at various positions across the axial dimension

the new steady state with the hot spot shown in Figure 4.7. This open–loop behavior of the reactor motivates the need for a control strategy able to suppress the temperature gradients and maintain a uniform temperature profile in the presence of disturbances.

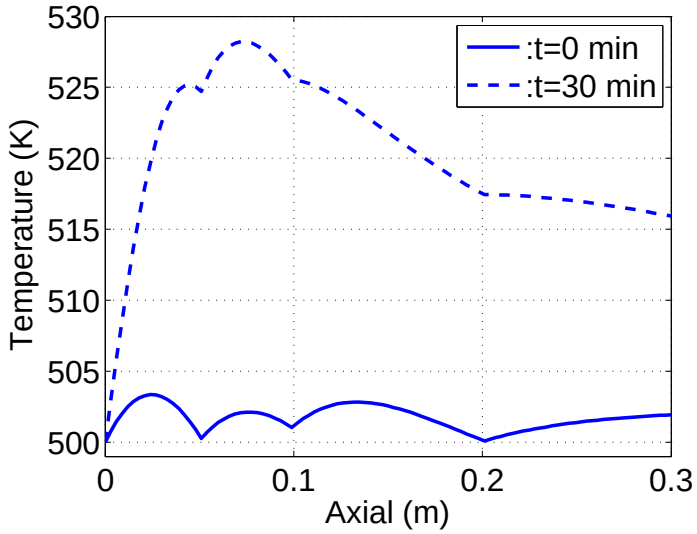

Figure 4.7: Reaction zone temperature distribution at different operating points

4.5 Controller design and closed–loop simulations

The control of the temperature in the reaction zone is achieved by manipulating the coolant (air) inlet flowrate. The process configuration considered provides three degrees of freedom resulting in a multiple–input–multiple–output (MIMO) controller. Given the distributed nature of the temperature in the reaction zone, we select the average temperature across a specified section of the reaction zone as the controlled variable:

$$y(t) =< T_t(z,t) >= \frac{1}{z_f - z_0} \int_{z_0}^{z_f} T_t(z,t)dz \tag{4.6}$$

where the limits z_f and z_0 denote to the initial and final position over which the controlled variable is evaluated. Specifically, the controlled variables for the three cooling sections are:

$$y_1(t) = 20 \int_0^{0.05} T_t(z,t)dz$$
$$y_2(t) = 20 \int_{0.05}^{0.1} T_t(z,t)dz$$
$$y_3(t) = 10 \int_{0.1}^{0.2} T_t(z,t)dz$$

4.5.1 Nonlinear controller design

A nonlinear output–feedback controller was derived on the basis of the PDE model of the reactor following the direct synthesis approach for hyperbolic PDEs in [152]. The controller corresponds to a distributed analogue of the nonlinear inversion–based geometric control methods for nonlinear ODEs. The characteristic index [152] (which is the analogue of the relative degree) between the controlled and manipulated inputs

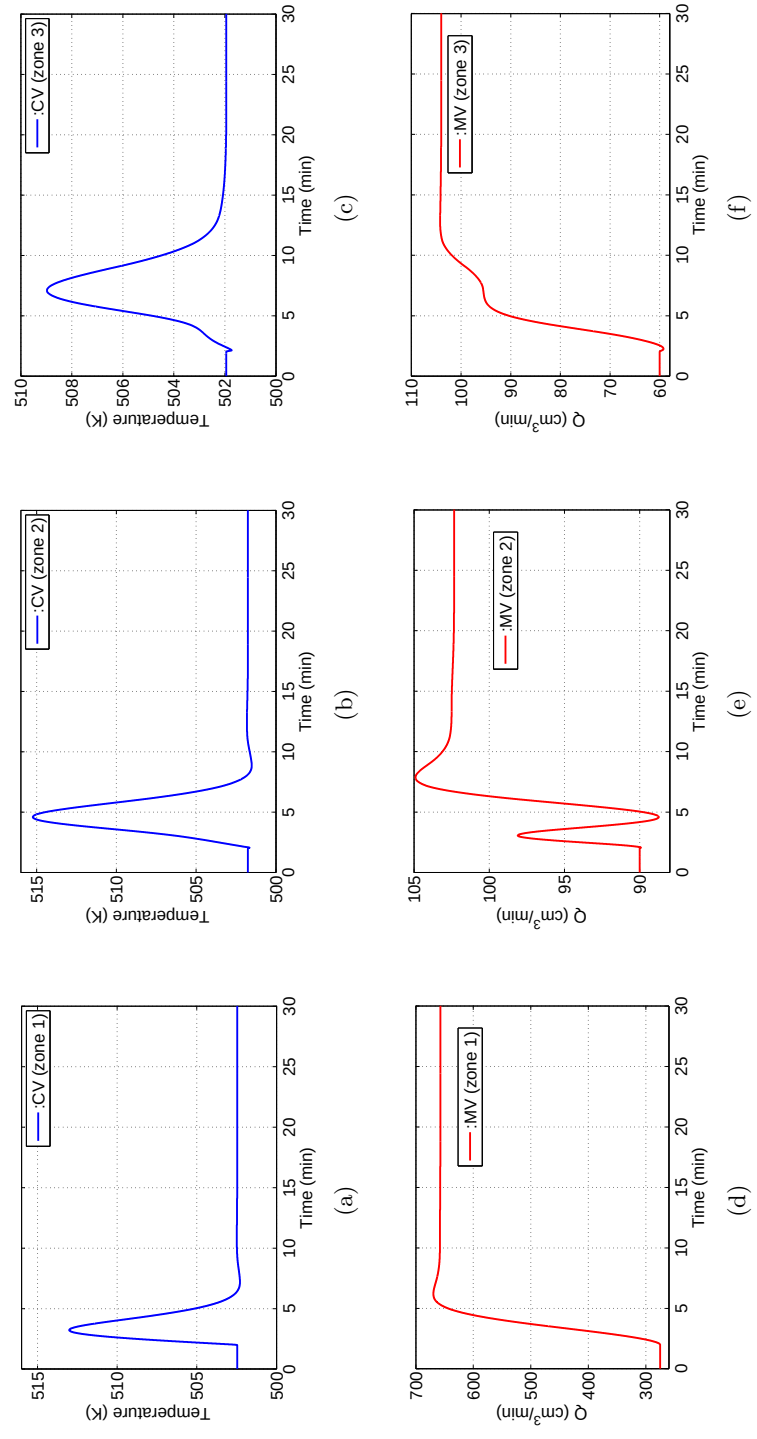

Figure 4.8: Closed–loop simulation under a 10% decrease in the pre–shift carbon monoxide conversion : (a)–(c) controlled variables and (d)–(f) manipulated variables

was calculated to be equal to 2. As a result, a decoupled second–order response was postulated, of the form:

$$\beta_{2,w}\frac{d^2y_w(t)}{dt^2} + \beta_{1,w}\frac{dy_w(t)}{dt} + y_w(t) = \upsilon_w(t) \tag{4.7}$$

where w denotes the control loop, υ_w refers to a reference input, and $\beta_{1,w}$, $\beta_{2,w}$ are adjustable parameters.

The process model developed in Section 4.3 can be reformulated in a state–space representation:

$$\begin{aligned} \frac{\partial x}{\partial t} &= \underline{\underline{A}}(x)\frac{\partial x}{\partial z} + \underline{f}(x) + \underline{\underline{g}}(x)\cdot u \\ y &= \underline{h}(x) \end{aligned} \tag{4.8}$$

where $x = [x_1(z,t)\cdots x_{15}(z,t)]^T$ refers to the state variables, $u = [u_1(t), u_2(t), u_3(t)]^T$ denotes the vector of the manipulated inputs, and $y = [y_1(t), y_2(t), y_3(t)]^T$ is the vector of the controlled variables. $\underline{\underline{A}}(x)^{[15\times15]}$ and $\underline{f}(x)^{[15\times1]}$, $\underline{\underline{g}}(x)^{[15\times3]}$, $\underline{h}(x)^{[3\times1]}$ are matrices and vectors of nonlinear functions. A simplified version of the above process model was used for the controller synthesis where the heat capacities and the enthalpy of reaction were assumed constant with respect to temperature and evaluated at the inlet conditions. In addition, a 10% modeling error was imposed in both the heat transfer coefficients and the membrane permeation rate. The controller is a combination of a distributed state–feedback controller derived to induce the postulated closed-loop responses and a distributed open-loop state–observer.

In order to compensate for the modeling errors, an external proportional–integral

(PI) controller was placed around each (υ_w, y_w) loop :

$$\upsilon_w(t) = \upsilon_{w,nom}(t) + K_c^w \left(e_w(t) + \frac{1}{\tau_I^w} \int_0^t e_w(\tilde{t}) d\tilde{t} \right) \tag{4.9}$$

$$\text{where: } e_w(t) = y_{sp,w}(t) - y_w(t)$$

where K_c (dimensionless) and τ_I (min) refer to the proportional gain and the time constant of the PI controller respectively.

4.5.2 Disturbance rejection

The controller performance was initially evaluated under the same disturbance scenario considered in the open–loop simulations. For all simulations the values of the adjustable parameters were $\beta_{1,w} = 0.83$ (min) and $\beta_{2,w} = 0.174$ (min^2) while the PI controller parameters were $K_c = 0.25$ and $\tau_I = 0.42$ (min), to achieve an overall critically dumped second–order response with a time constant of 0.83 min (in the absence of disturbances and modeling errors). Figure 4.8 shows the closed–loop responses for both the controlled

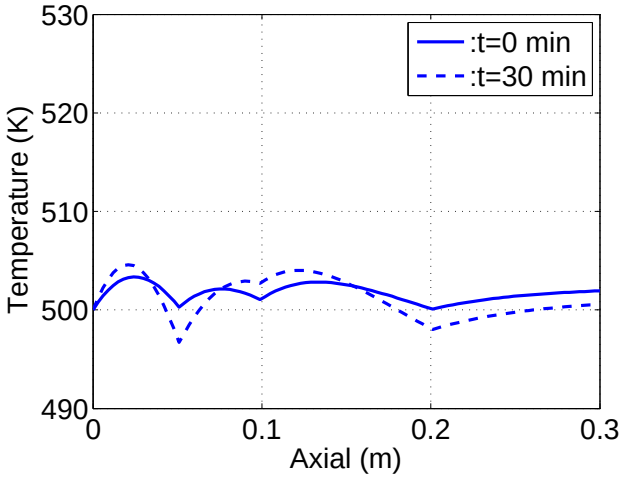

Figure 4.9: Temperature distribution before and after the imposed disturbance

and manipulated variables in each control loop. The controller is successful in regulating the controlled variables at their set points under the imposed disturbance, despite the modeling errors considered. Furthermore, an almost uniform temperature profile is maintained as shown in Figure 4.9.

4.5.3 Set point tracking

We next considered a case study where a set point change from the nominal value to 480 K is imposed. This is a typical scenario when the CO conversion has decreased and a lower operating temperature is required in order to shift the equilibrium conversion back to the desired level. Figure 4.10 depicts the response of the model–based controller, compared also to two representative PI controllers (other PI controllers were also used but resulted in generally worse performance and are not shown here).

The model–based controller smoothly brings the controlled outputs to the requested new operating temperature. The PI controllers with the tighter tuning (blue curves) show very aggressive behavior leading to control actions which are physically unrealizable given the dimensions of the reactor. The PI controllers with the less aggressive tuning parameters (red curves) lead to closed–loop responses showing large undershoots which in some regions are almost 50% of the imposed set point change. Given that the controlled variables represent average temperatures along the reactor, large undershoots could result in large temperature gradients which can affect negatively the operation of the reactor. The above observations document the superiority of the model-based controller over the PI controllers in enforcing set point changes.

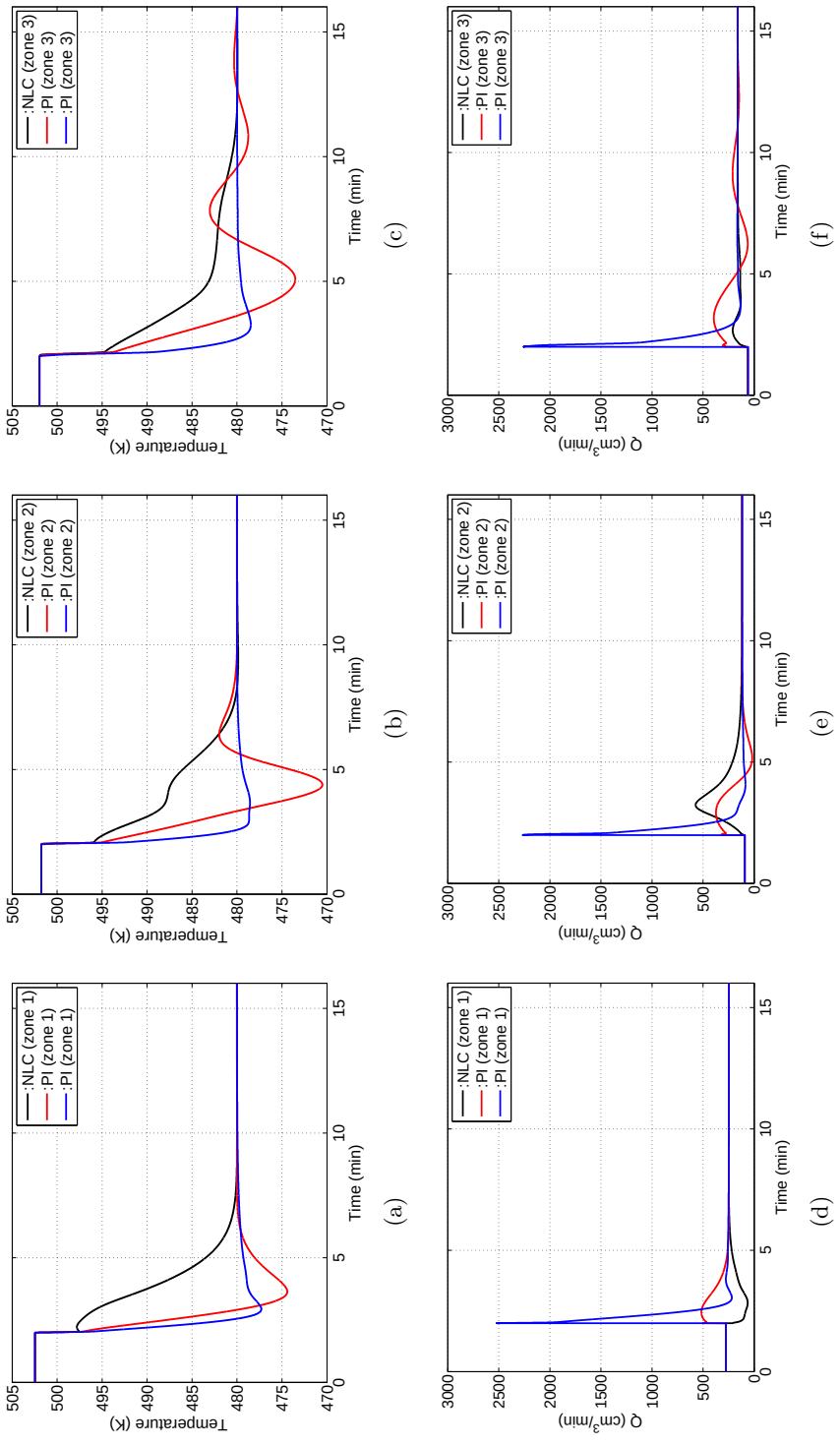

Figure 4.10: Comparison between model–based and PI controller for a setpoint change to 480 K. PI tuning parameters used in this simulation: $K_c = 10$ (cm^3/min/K) and $\tau_I = 0.42$ (min) (red curves) and $K_c = 100$ (cm^3/min/K) and $\tau_I = 0.83$ (min) (blue curves)

CHAPTER 5

Optimal Designs in Combined Heat and Power Solid Oxide Fuel Cell Systems

Overview: Combined heat and power SOFC systems, a promising candidate for distributed generation, face design challenges due to the volatile demand for heat and power. This chapter analyzes the design flexibility of combined heat and power SOFC systems using multiple recycle streams. A direct internal reforming SOFC along with a pre–reforming unit are considered the main heat and power generation unit. A mathematical model is developed consisting of a set of differential algebraic equations. A contrained nonlinear optimization problem is formulated employing recycle ratios, SOFC and pre–reforming operating conditions and specific stream temperatures as decision variables. Optimal designs for maximum system's electrical efficiency and heat–to–power ratio are obtained. The results reveal the ability of stream

recycling for improved design flexibility and a successful response to different operating objectives.

5.1 Introduction

Combined heat and power (CHP) SOFC systems show the potential for simultaneous highly efficient power generation and high–grade heat generation making them a promising option for distributed energy generation. CHP SOFC systems are an emerging energy alternative for residential, commercial and industrial applications [42, 48, 49, 153]. Their use in marine applications [154] and integration with renewable energy technologies (e.g. solar [50, 92, 155]) has been also analyzed. Besides providing electricity, high–grade heat can be used for either heating or cooling purposes or both [92, 156, 157] leading to the so called *tri–generation energy systems* [158].

Typical analysis in CHP systems has focused on performance aspects in terms of either electrical efficiency or cost of electricity [54, 56, 55, 159]. However, fluctuations in heat and power demand impose design and operational challenges. As a result, design flexibility of SOFC systems for CHP applications under varying heat and power demands is essential [53]. To this end, the heat–to–power ratio has been considered a key design factor in CHP systems [53].

Material and energy recycles are a promising option for increased design and operational flexibility despite the higher complexity of the resulting process schemes. Several studies have analyzed the effect of either anode or cathode gas recycle to the performance and process safety of the plant [49, 55, 159, 160, 161, 73, 162, 163, 164, 54, 165, 166]. However, an overall systems level analysis involving multiple recycle loops and different operating modes, would provide a broader picture on the level of design flexibility.

In this chapter, the design flexibility is analyzed under different operating modes

by formulating a constrained nonlinear optimization problem. The CHP SOFC system consists of three major process units: a natural gas–fed SOFC stack (direct internal reforming SOFC), a pre–reforming unit and a catalytic burner. Three recycles are considered: a) anode off–gas recycle to the anode inlet of the SOFC b) anode off–gas recycle to the inlet of the pre–reforming unit and c) cathode off–gas recycle to the cathode inlet of the SOFC. Optimal designs for maximized system's electrical efficiency and heat–to–power ratio are obtained and their features are discussed and compared.

Section 5.2 provides a description of the CHP SOFC configuration involving multiple recycle loops. In section 5.3 the mathematical model is presented and the optimization problem is formulated. The decision variables and the constraints for each operating mode are discussed in Section 5.4. The optimal designs and their main features are also discussed in Section 5.4.

5.2 Description of the CHP SOFC system

In this analysis, an intermediate temperature anode–supported planar SOFC is considered employing direct internal reforming of natural gas within the anode. The hydrogen is assumed to be the only electrochemically active species while the carbon monoxide is assumed to participate only in the WGS reaction producing more hydrogen and carbon dioxide. A pre–reforming unit is placed before the SOFC in order to prevent risks associated with pure methane at the entrance of the SOFC [167]. Steam reforming and water gas shift reactions are considered in the pre–reforming unit. The features of the remaining processes have been discussed in Chapter 3.

A typical process configuration for a CHP SOFC system involving stream recycling is shown in Figure 5.1. According to Figure 5.1, unreacted fuels leaving the anode can be recycled back to the inlet of the pre–reforming unit and to the SOFC anode inlet

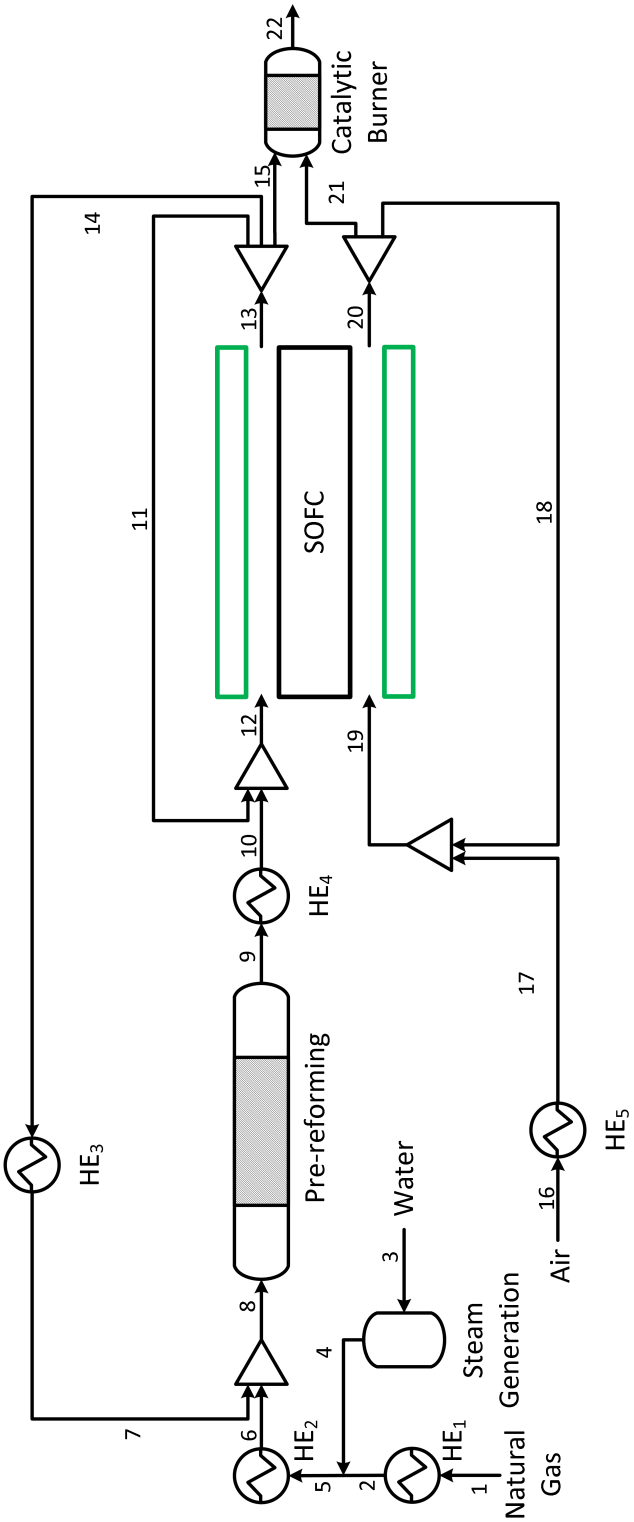

Figure 5.1: Process configuration for base case scenario

respectively. In addition, typical high air ratios, used for cooling of the fuel cell, allow for cathode recycling. Hence, the option of stream recycling increases the degrees of freedom for process design and hence the design flexibility.

5.3 Mathematical Problem Formulation

5.3.1 Mathematical models

The mathematical model consists of a set of differential–algebraic equations (DAEs), developed based on first principles (e.g. mass and energy balances) at steady–state. Natural gas is assumed to be 100% methane and the operating pressure for the entire CHP plant is fixed to atmospheric pressure. Given the low operating pressure, the use of fluid transferring process units (e.g. fans, pumps) has been omitted in this analysis. Other assumptions considered during the modeling of the CHP plant include: ideal gas behavior, plug flow condition and complete conversion of unreacted fuels in the catalytic burner. In addition, the SOFC stack consists of a number of single cells with a uniform voltage distribution. A uniform temperature distribution has been assumed in the pre–reforming unit imposed through distributed heating elements.

Pre–reformer:

The mass balances in the pre–reforming unit are:

$$\frac{\partial F_i}{\partial \bar{z}} = \sum_j \nu_{i,j} R_j \tag{5.1}$$

where $i = (CH_4, H_2O, CO, CO_2, H_2)$, $j = \{\text{smr,wgs}\}$, $\nu_{i,j}$ is the stoichiometric coefficient matrix and R_j refers to the reaction rates for the steam methane reforming and water gas shift reactions [108]. Furthermore, F is the molar flowrate (mol/s) and

$\bar{z}$ is the dimensionless length ($\bar{z} = z/L_R$) where L_R corresponds to the length of the pre–reforming unit. The methane conversion is determined using the following equation:

$$x_{CH_4} = 1 - \frac{F_{CH_4}(1)}{F_{CH_4}(0)} \tag{5.2}$$

Solid Oxide Fuel Cell:

The mathematical model for an anode–supported intermediate temperature SOFC with direct internal reforming has been adopted from [168]. In their work [168], the authors developed a distributed mathematical model including mass balances in anode and cathode channel and energy balances in each compartment of the SOFC (e.g. fuel/air channels, electrodes/electrolyte, interconnect). For simplicity in this analysis, we assume a uniform temperature across all compartments of the SOFC, therefore a single energy balance is used for the entire SOFC. The mass and energy balances used in this analysis are:

$$\frac{\partial F_i}{\partial \bar{z}} = \sum_k \nu_{i,k} R_k \tag{5.3}$$

$$\frac{\partial}{\partial \bar{z}} \left(\sum_i F_i M w_i \tilde{H}_i \right) + A_{elec} V_{sofc} J = 0 \tag{5.4}$$

where $k =$ (elec, smr, wgs), A_{elec} denotes the electrochemically active area of the fuel cell (m^2), V_{sofc} is the voltage of the SOFC (V) and J refers to the current density (A/m^2). $\tilde{H}_i$ represents the mass specific enthalpy (J/kg) of each component calculated from the following equation:

$$\tilde{H}_i = \Delta H^{\circ}_{f,i} + \int_{T_{ref}}^{T} C_{pi}(\tilde{T}) d\tilde{T}$$

with the heat capacity C_{pi} (J/kg/K) of each component evaluated using the equation 4.4. In addition, the voltage of the SOFC is calculated using the equation 3.2 with the expressions for its individual terms given in [168].

The remaining process units are modeled using lumped models (see Chapter 3) and their heat duties are calculated through their enthalpy change ($Q = \Delta H$) between the inlet and the outlet of each corresponding process.

5.3.2 Optimization problem formulation

A constrained nonlinear optimization is formulated of the following form:

$$\begin{aligned} &\max\ f(\boldsymbol{x}) \\ &\text{s.t}\ \boldsymbol{h}(\boldsymbol{x}) = 0 \\ &\boldsymbol{g}(\boldsymbol{x}) \leq \boldsymbol{c} \\ &\boldsymbol{x} \in \boldsymbol{X} \subset \mathbb{R}^n \end{aligned} \tag{5.5}$$

where $\boldsymbol{h}(\boldsymbol{x})$ and $\boldsymbol{g}(\boldsymbol{x})$ are nonlinear functions acting as equality and inequality constraints and $\boldsymbol{x}$ denotes the decision variables. Two individual case studies are analyzed reflecting different operating modes of the CHP system. In the first case study, the electrical efficiency of the entire CHP plant is maximized while in the second case study the heat–to–power ratio is maximized. The developed optimization problem was simulated using the gPROMS Modelbuilder v3.6 simulation platform using the SRQPD solver which uses the SQP method for NLP problems [169]. All simulations were performed in a 64–bit Windows 7 CPU equipped with a i7 processor at 2.67 GHz and 8GB of RAM.

In the next section, a base case and the optimization studies are presented. The objective function, decision variables and constraints are discussed for each optimization study.

5.4 Simulations

5.4.1 Base case study

A base case study simulation (see Figure 5.1) is performed where no stream recycling is considered. The operating conditions used in this simulation are shown in the following table, where λ_{air} is the air ratio defined in [168], S/C is the steam–to–carbon ratio at

Table 5.1: Operating conditions for base case scenario

Variable	**Value**	**Variable**	**Value**
U_F (%)	85	$T_{ca,in}$ (K)	1023
V_{sofc} (V)	0.67	$T_{an,in}$ (K)	1023
$\bar{P}$ (W/cm^2)	0.4	$\dot{m}_{CH_4^{in}}$ (kg/h)	42.2
x_{CH_4} (%)	10	λ_{air}	8.5
T_R (K)	615	S/C	2
T_{CB} (K)	1176	N_{cell}	10^4

the inlet of the pre–reformer and N_{cell} denotes the number of cells in the SOFC stack. Figures 5.2 and 5.3 depict the species mole fractions and the temperature distribution across the SOFC axial dimension. According to Figures 5.2 and 5.3, the high reaction rates of the internal reforming reactions at the inlet of the anode lead to an increased hydrogen concentration and a decreased temperature. However, there is a point (∼0.24) where the internal reforming rate becomes equal to the hydrogen electrochemical reaction rate. After that point, the hydrogen electrochemical reaction dominates consuming hydrogen and releasing heat. This behavior results in an uneven temperature profile as shown in the Figure 5.3.

5.4.2 Case study 1: Optimal design for maximized electrical efficiency

The electrical efficiency for the entire CHP plant is defined as ratio of the generated power to the total chemical energy entering the plant calculated using the Lower Heating

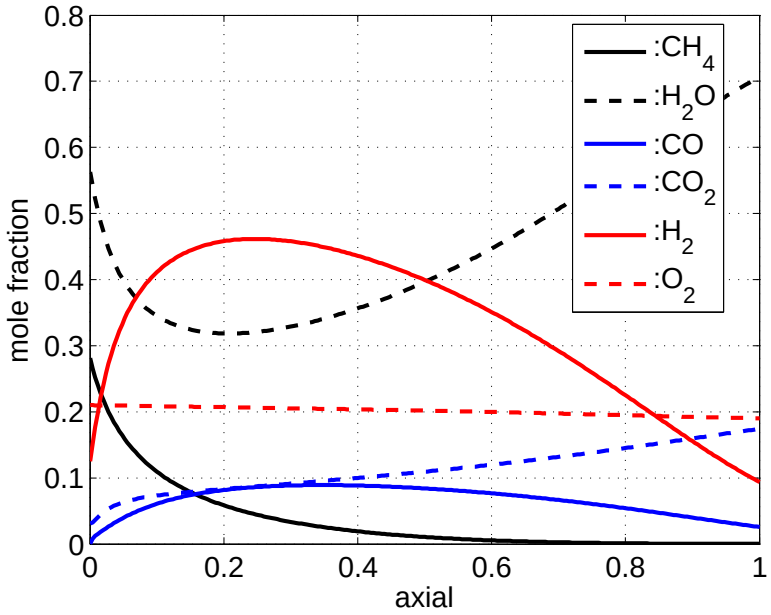

Figure 5.2: Species mole fraction distribution in anode and cathode of the SOFC

Value (LHV) of the fuel (e.g. methane):

$$f(\boldsymbol{x}) \;=\; \frac{A_{elec} V_{stack} J}{F^{in}_{CH_4}\; LHV_{CH_4}} \tag{5.6}$$

Typically, AC power is used in the system's electrical efficiency calculation [170], however this study does not consider any integration of power electronics (e.g. DC/AC converter) downstream to the SOFC hence the DC power generated from the SOFC is used. The following recycle ratios are defined:

$$\text{anode: } \boldsymbol{ASR} \;=\; \frac{\dot{m}_i}{\dot{m}_{13}} \quad \text{where: } i \;=\; 11, 14, 15 \tag{5.7}$$

$$\text{cathode: } \boldsymbol{CSR} \;=\; \frac{\dot{m}_j}{\dot{m}_{20}} \quad \text{where: } j \;=\; 18, 21 \tag{5.8}$$

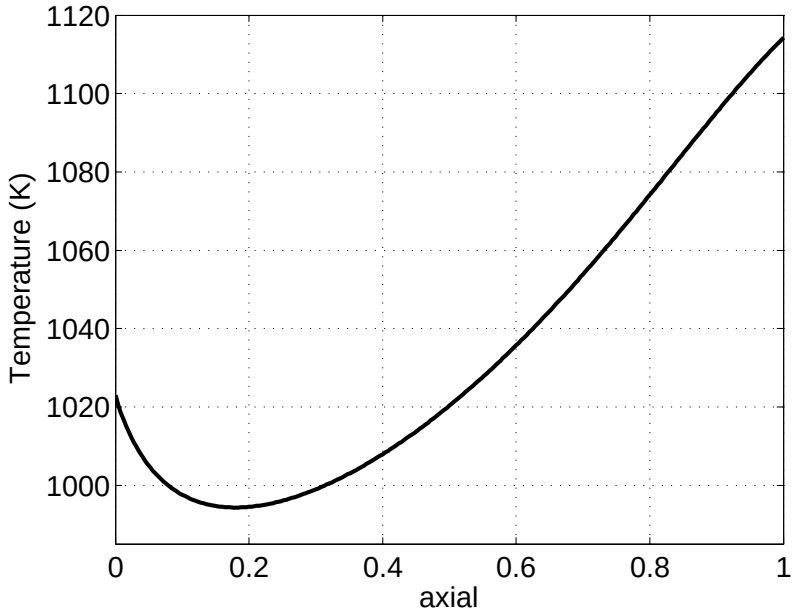

Figure 5.3: SOFC temperature distribution

where ASR and CSR refer to anode and cathode stream ratio respectively, $\dot{m}$ denotes the mass flowrate (kg/s) and the subscripts refer to the streams in Figure 5.1.

The decision variables used in this simulation are the following:

$$\boldsymbol{x} = \begin{bmatrix} ASR_1 & ASR_2 & ASR_3 & CSR_1 & CSR_2 & T_6 & T_7 & x_{CH_4} & U_F & V_{sofc} & T_{12} & T_{19} \end{bmatrix}^{\boldsymbol{T}} \tag{5.9}$$

where ASR_3 $\in$[0.05,1] to ensure a minimum feed of unreacted fuel to the catalytic burner and the remaining recycle ratios $\in$[0,1]. x_{CH_4} $\in$[0.05,1] in order to prevent any feed of pure methane to the SOFC anode. U_F $\in$[75,85] in order to maintain a sufficient level of fuel utilization and avoid fuel starvation conditions. V_{sofc} $\in$[0.6,0.7] since we would like to operate the SOFC in a common voltage range for direct internal reforming SOFC. T_{12} $\in$[973,1073] and T_{19} $\in$[973,1073] to ensure an appropriate SOFC operating temperature. T_7 is lower bounded by 298 K to avoid excessive cooling while T_6 is lower

bounded by 373 K in order to prevent any cooling below the water bubble point.

In addition to the mathematical model of the CHP plant, which acts as equality constraint in the optimization problem, the following equality and inequality constraints are included:

- $\sum_{i=1}^{3} ASR_i = 1$: The sum of all recycle ratios at the anode should always be equal to unity
- $\sum_{j=1}^{2} CSR_j = 1$: The sum of all recycle ratios at the cathode should always be equal to unity
- $F^{in}_{O_2,cb} > 0$ mol/s: Maintain oxygen supply to the catalytic burner
- $F^{in}_{H_2O,feed} \geq 0$ mol/s: Prevent negative inlet water flowrates
- $T_{sofc}(1) \leq 1173$ K: Limit the SOFC outlet temperature to 1173 K
- $T_{17} \geq 298$ K: Prevent any cooling of air below ambient conditions
- 0.35 W/cm$^2 \leq P_{sofc} \leq 1$ W/cm^2: Ensure an operation under reasonable power densities
- 0 K$\leq \Delta T_{R,max} \leq 50$ K: Maintain a small temperature difference in pre–reforming unit
- 0 K$\leq \Delta T_{sofc,max} \leq 150$ K: Prevent large temperature gradients across the SOFC

The optimal solution corresponds to a system electrical efficiency of 64.5%. The optimal values for the decision variables are shown in Table 5.2 and the optimal design is depicted in Figure 5.4. The main findings of this simulation include the large contribution of the anode recycles and the elimination of the steam generation unit. More than half of the stream leaving the anode is recycled back to the pre–reforming unit where a

Table 5.2: Case study 1: optimal values for the decision variables

Variable	**Value**	**Variable**	**Value**
ASR_1	0.23	T_7 (K)	956.72
ASR_2	0.53	x_{CH_4} (%)	37.7
ASR_3	0.24	U_F (%)	85
CSR_1	1	V_{sofc} (V)	0.7
CSR_2	0	T_{12} (K)	1073
T_6 (K)	376.15	T_{19} (K)	1073

methane conversion of 37.7% is achieved. This recycle satisfies the required S/C ratio at the inlet of the pre–reforming unit allowing for a sustainable operation in terms of steam generation. In addition, 24% of the anode outlet stream is recycled back to the anode in order to improve the system electrical efficiency. The optimal operating conditions of the SOFC show the attempt of the system to maximize the electrical efficiency since the SOFC operates at the upper bounds of the fuel utilization and the operating voltage which potentially leads to a higher power density. In addition to this, both the anode and cathode inlet temperatures reach their upper bounds trying to increase the SOFC operating temperature in order to increase the electronic conductivity of the electrolyte and hence the SOFC performance. However, it should be mentioned that this increase of the cathode temperature compared to the base case, results in a higher air pre–heating duty which dominates the energy demand for pre–heating. Considering also its high temperature, energy integration could be challenging.

5.4.3 Case study 2: Maximizing the heat–to–power ratio

The heat–to–power ratio is defined as the net heat to the generated power. The net heat of the CHP plant is calculated as the difference of the total available heat generated and

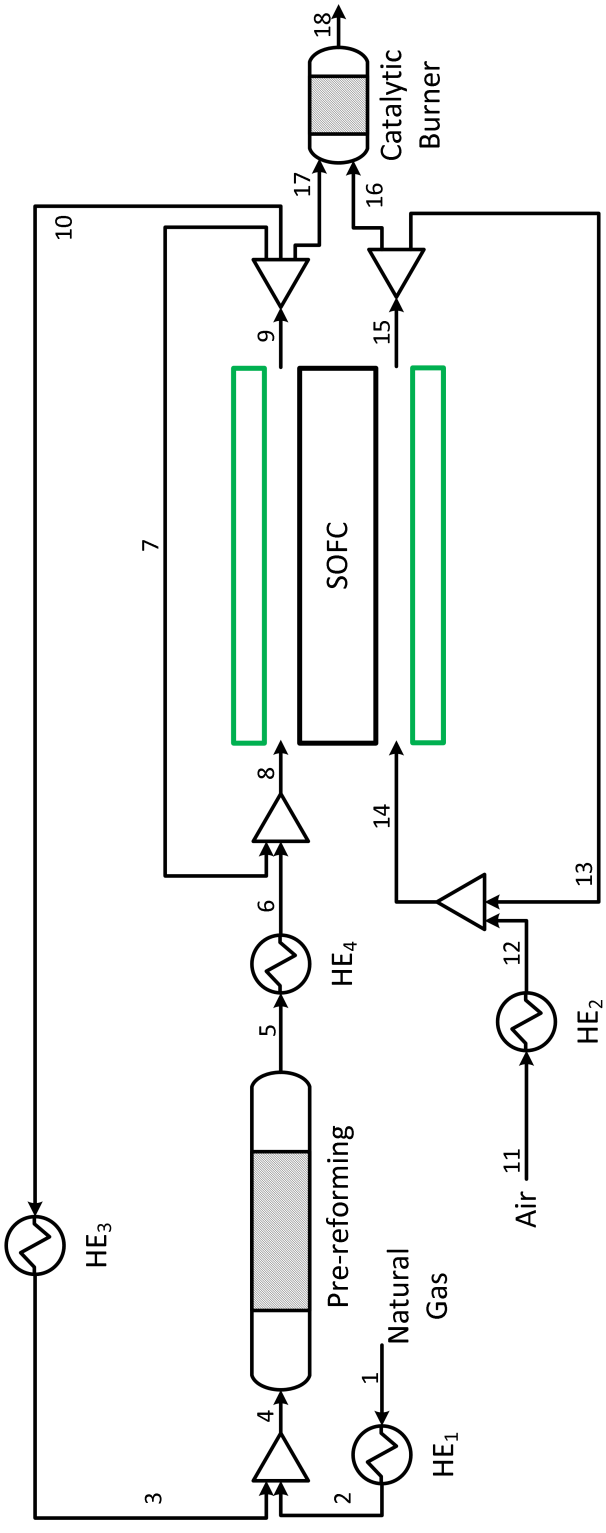

Figure 5.4: Optimal design for maximized electrical efficiency

the heating loads for the streams pre–heating and the pre–reformer heating requirement:

$$f(\boldsymbol{x}) \;=\; \frac{Q_{total} \;-\; Q_{heating}}{A_{elec} V_{stack} J} \tag{5.10}$$

The decision variables used in this simulation are shown below in vector form:

$$\boldsymbol{x} \;=\; \begin{bmatrix} ASR_1 & ASR_2 & ASR_3 & CSR_1 & CSR_2 & T_7 & x_{CH_4} & U_F & V_{sofc} & T_{12} & T_{19} \end{bmatrix}^{\boldsymbol{T}} \tag{5.11}$$

The same bounds as in the previous case study are considered. In terms of constraints, most of the previous constraints hold while a constraint considered above is changed. In addition to this, two new constraints are imposed. The additional constraints are:

- $F^{in}_{H_2O,feed}$=0 mol/s: Maintain a self–sustained operation in terms of steam generation
- 0 kW$\leq P_{stack} \leq$300 kW: Ensure a comparable output power with the previous case studies
- 50 %$\leq \eta_{electrical} \leq$100 %: Retain a highly efficient operation

The optimal solution is attained for a heat–to–power ratio equal to 0.92. The values of the decision variables at the optimal solution are presented in Table 5.3 and the optimal design is shown in Figure 5.5. According to the results, the main features of

Table 5.3: Case study 2: optimal values for the decision variables

Variable	**Value**	**Variable**	**Value**
ASR_1	0.43	T_7 (K)	947
ASR_2	0.53	x_{CH_4} (%)	35.9
ASR_3	0.04	U_F (%)	75
CSR_1	0.07	V_{sofc} (V)	0.6
CSR_2	0.93	T_{12} (K)	973
		T_{19} (K)	999

the CHP plant include its attempt to reduce the heating loads and maintain a large supply of unreacted fuels to the catalytic burner for increased heat generation. In order to ensure a sustainable operation in terms of steam generation, 53% of the anode outlet stream is recycled back to the pre–reforming unit. In addition, the anode recycle ratio has been decreased from 24% in the previous study to 4% in order to satisfy the constraint on the system's electrical efficiency. On the other hand, the cathode recycle ratio has increased from 0% to 97% eliminating the need for air pre–heating since the required cathode inlet temperature is achieved by mixing the recycling stream with fresh air. The SOFC operates at a lower fuel utilization in order to allow for more heat generation in the catalytic burner. Furthermore, the anode and cathode inlet temperatures have been decreased leading to lower heating loads while satisfying the SOFC operating constraints.

5.4.4 Comparison of SOFC temperature distribution

Figure 5.6 depicts the normalized SOFC temperature distributions for each case study. Since both optimal designs are obtained with a pre–reforming conversion higher than the base case scenario (37.7% and 35.9% to 10%), it is expected that they exhibit a smoother temperature profile than the base case scenario as shown in Figure 5.6. Apart from the effect of the higher pre–reforming conversion, the anode recycle influences the shape of the temperature distributions leading to lower temperature gradients across the SOFC. Higher concentrations of hydrogen at the inlet of the anode channel result in more energy released due to the electrochemical reactions. Considering also the reduced concentration of methane at the inlet of the anode channel the temperature gradient is decreased.

According to Figure 5.6, the temperature distribution associated with the optimal design of the second case study shows a smoother temperature distribution compared to

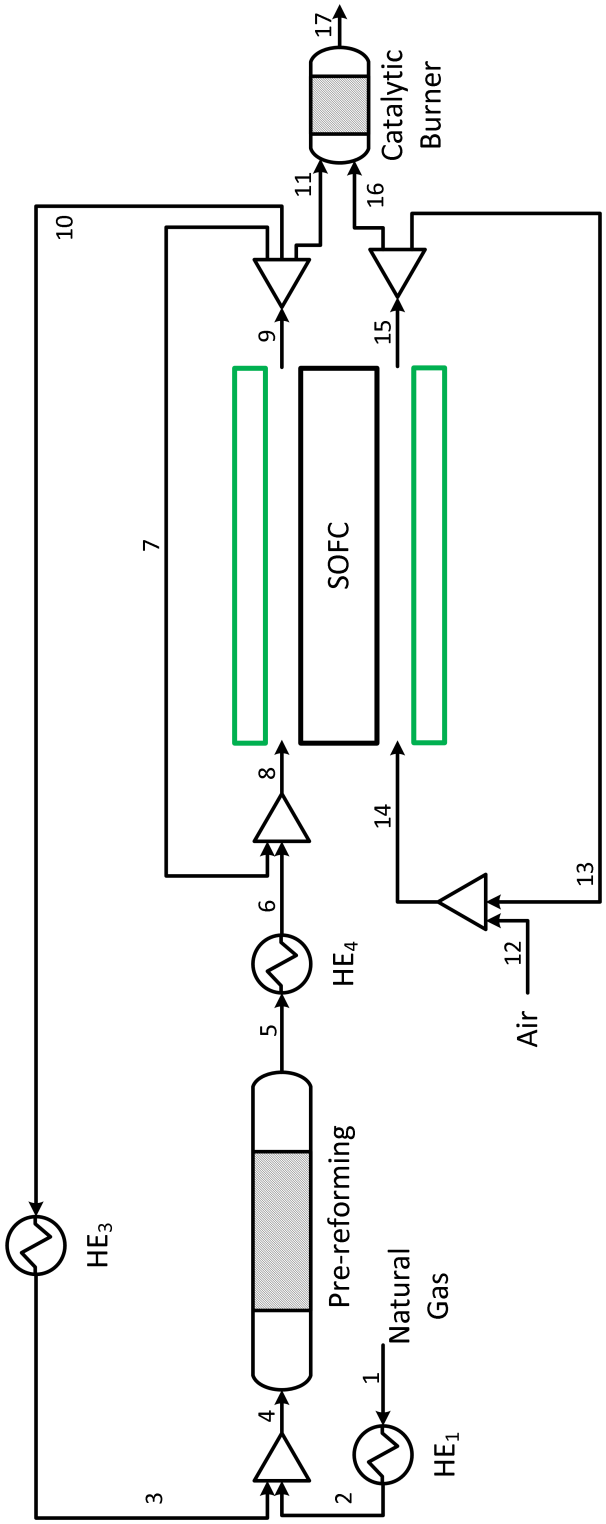

Figure 5.5: Optimal design for maximized heat–to–power ratio

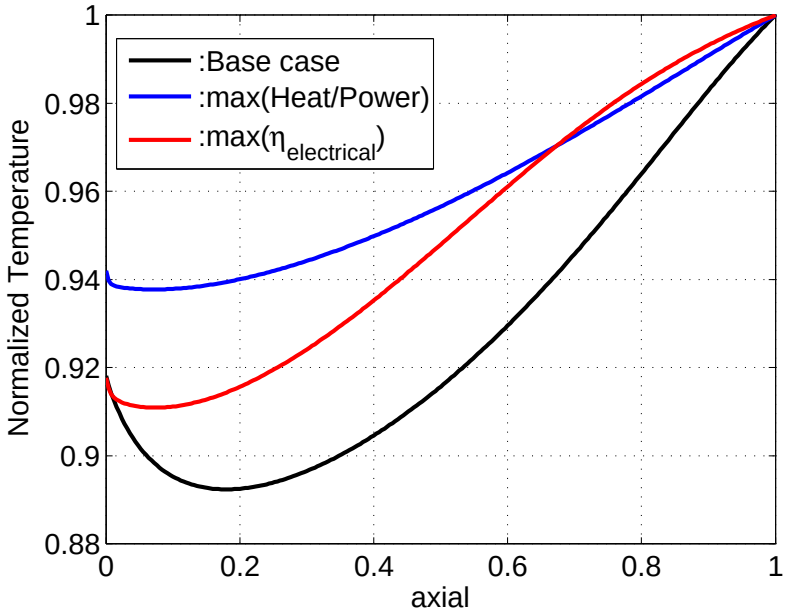

Figure 5.6: Comparison of SOFC temperature distribution for each case study

the other cases. Although a lower pre–reforming conversion is achieved compared to the first case study, the lower SOFC inlet temperatures lead to slower internal reforming reaction kinetics. In addition to this, the lower fuel utilization prevents any sharp increase in the temperature compared to the other two cases.

CHAPTER 6

Summary and Future Directions

Motivated by the need for highly efficient and environmentally friendly power generation, this dissertation focuses on the design and control of integrated systems for hydrogen production and power generation. Two integration strategies, energy integration and process intensification, were considered since they have shown a great potential for increased energy efficiency. In addition, SOFC systems were designed employing the above integration strategies and challenges in terms of design, operation and control were identified and solutions were proposed.

In the first part of the thesis, two energy integrated configurations were analyzed comprising a SOFC, a methane steam reformer and energy transfer units. In the first configuration, the SOFC outlet streams were used directly for energy integration, while in the second, these streams were fed to a catalytic burner for more energy recovery and recycle. The first configuration was shown to become unstable for large changes in

current. This was attributed to a positive energy feedback loop which results in high temperatures and fuel starvation. A linear multi-loop control strategy was developed for the entire integrated system. The proposed control strategy was shown to be successful in suppressing the instability in the first configuration and to provide satisfactory closed-loop responses for a broad range of positive and negative changes in the current.

The use of process intensification for simultaneous hydrogen generation and carbon capture has brought water gas shift (WGS) membrane reactors to the forefront as an emerging technology. Thermal management in these type of reactors is essential for maintaining the reactor's performance at desired conditions. In the second part of the thesis, a dynamic model for a hydrogen–selective WGS membrane reactor for the production of high-purity hydrogen was developed and a distributed control strategy was proposed for regulating the temperature along the reactor. The strategy involved distributed actuation with cooling zones placed judiciously along the reactor and a model-based output feedback controller derived on the basis of the distributed process model. The controller was shown to be successful in suppressing hot spots that can be detrimental to the reactor performance, in the presence of disturbances and set point changes. A comparison with classical PI controllers demonstrated the benefit of using model-based control even in the presence of modeling errors.

The ability of SOFCs for combined heat and power (CHP) generation has attracted a lot of attention as a promising option for distributed generation. Design flexibility of CHP SOFC systems is essential in order to ensure a continuous and reliable source of energy under a volatile energy market. The CHP SOFC system considered in the thesis includes a direct internal reforming SOFC along with a pre–reforming unit before the SOFC. The option for multiple recycle loops in the CHP configuration has been a key factor in design flexibility. A nonlinear optimization problem was formulated and optimal designs were obtained for different operating modes. The preliminary results

showed that a systems level optimization formulation including recycle ratios as decision variables can successfully evaluate optimal operating conditions for different operational objectives.

In addition to the previous study in CHP SOFC, further design objectives should be considered in order to allow for broader insights. Therefore, the previous design analysis should include energy integration by reformulating the optimization problem. It is expected that this reformulation would transform the previously developed nonlinear program (NLP) to a mixed–integer nonlinear program (MINLP). Optimal bypass placement in the new attained energy integrated configuration would allow for control studies. Developing a real time optimizer (RTO) as a supervisory controller would allow for an optimal operation based on either economical or environmental objectives. Optional integration of the CHP SOFC system with renewable energy resources would allow for a lower environmental impact. Additional integration with power and thermal storage units would further increase the flexibility of the CHP SOFC system.

In terms of large–scale power plants, system's level analysis for integration of SOFCs with conventional power plants (e.g IGCC, NGCC) and options for additional integration with biomass are expected to attract a lot of attention. Improving operability and ensuring a robust system's response under various disturbances would lead to attractive solutions for future power generation systems.

Bibliography

[1] NETL. *Fuel Cell Handbook 7th Edition*. U.S. Department of Energy, 2004.

[2] Comparison of Fuel Cell Technologies. http://www1.eere.energy.gov/hydrogenandfuelcells/fuelcells/pdfs/fc_comparison_chart.pdf. Accessed: 10-21-2013.

[3] National Energy Technology Laboratory. Cost and performance baseline for fossil energy plants volume 1: Bituminous coal and natural gas to electricity. Technical Report 2010/1397, DOE NETL, USA, November 2010.

[4] SECA A Primer on SOFC Technology. http://www.netl.doe.gov/technologies/coalpower/fuelcells/seca/primer/cell.html. Accessed: 11-11-2013.

[5] http://mech-server.mech.kyoto-u.ac.jp/lab/yoshida/b4intro/nishino/tubularE4.jpg. Accessed: 11-11-2013.

[6] Dimitrios Georgis, Fernando V Lima, Ali Almansoori, and Prodromos Daoutidis. Modeling and control of a water gas shift membrane reactor for hydrogen production. In *American Control Conference (ACC), 2012*, pages 4287–4292. IEEE, 2012.

[7] Core Writing Team, Pachauri, R.K. and Reisinger, A. (Eds.). Climate change 2007: Synthesis report. Technical report, IPCC, Geneva, Switzerland, November 2007.

[8] U.S Environmental Protecting Agency. Inventory of u.s greenhouse gas emissions and sinks: 1990–2010. Technical Report 430–R–12–001, EPA, Washington, DC, April 2012.

[9] OECD Stat. Exacts. http://stats.oecd.org/Index.aspx?DataSetCode=AIR_GHG. Accessed: 10-17-2013.

[10] OECD. Environmental outlook to 2030. Technical report, OECD, Paris, France, 2008.

[11] WEC. World energy insight 2012. Technical report, WEC, London, UK, 2012.

[12] BP. Energy outlook 2030. Technical report, BP, London, UK, 2013.

[13] International Energy Agency. Key world energy statistics. Technical report, OECD/IEA, Paris, 2013.

[14] U.S Energy Information Administration. http://www.eia.gov/tools/faqs/faq.cfm?id=105&t=3. Accessed: 10-03-2013.

[15] Coal Industry Advisory Board. Power generation from coal: Measuring and reporting efficiency performance and co_2 emissions. Technical report, OECD IEA, France, 2010.

[16] U.S Fuel Economy Information. http://www.fueleconomy.gov/feg/atv.shtml. Accessed: 10-03-2013.

[17] Ram Ramachandran and Raghu K. Menon. An overview of industrial uses of hydrogen. *International Journal of Hydrogen Energy*, 23(7):593–598, 1998.

[18] John A. Turner. Sustainable hydrogen production. *Science*, 305(5686):972–974, 2004.

[19] Committee on Alternatives, Strategies for Future Hydrogen Production, and National Academy of Engineering Use, National Research Council. *The Hydrogen Economy: Opportunities, Costs, Barriers, and R&D Needs*. The National Academies Press, 2004.

[20] Magdalena Momirlan and T. Nejat Veziroglu. The properties of hydrogen as fuel tomorrow in sustainable energy system for a cleaner planet. *International Journal of Hydrogen Energy*, 30(7):795–802, 2005.

[21] Fuel Cell Vehicles. http://www.fuelcells.org/uploads/carchart.pdf. Accessed: 10-12-2013.

[22] Steven G. Chalk, James F. Miller, and Fred W. Wagner. Challenges for fuel cells in transport applications. *Journal of Power Sources*, 86(1):40–51, 2000.

[23] Panini Krishna Kolavennu. *Analysis and control of an in situ hydrogen generation and fuel cell power system for automotive applications*. PhD thesis, Florida State University, December 2005.

[24] Dimitrios Georgis, Sujit S Jogwar, Ali Almansoori, and Prodromos Daoutidis. Design and control of energy integrated SOFC systems for in–situ hydrogen production and power generation. *Computers & Chemical Engineering*, 35(9):1691–1704, 2011.

[25] Peter P. Edwards, Vladimir L. Kuznetsov, William I.F. David, and Nigel P. Brandon. Hydrogen and fuel cells: towards a sustainable energy future. *Energy Policy*, 36(12):4356–4362, 2008.

[26] S. Litster and G. McLean. PEM fuel cell electrodes. *Journal of Power Sources*, 130(1):61–76, 2004.

[27] Chunshan Song. Fuel processing for low–temperature and high-temperature fuel cells: Challenges, and opportunities for sustainable development in the 21st century. *Catalysis Today*, 77(1):17–49, 2002.

[28] Yuyan Shao, Geping Yin, Zhenbo Wang, and Yunzhi Gao. Proton exchange membrane fuel cell from low temperature to high temperature: material challenges. *Journal of Power Sources*, 167(2):235–242, 2007.

[29] Jianlu Zhang, Zhong Xie, Jiujun Zhang, Yanghua Tang, Chaojie Song, Titichai Navessin, Zhiqing Shi, Datong Song, Haijiang Wang, David P Wilkinson, Zhong-Sheng Liu, and Steven Holdcroft. High temperature PEM fuel cells. *Journal of Power Sources*, 160(2):872–891, 2006.

[30] Brian C.H. Steele and Angelika Heinzel. Materials for fuel-cell technologies. *Nature*, 414(6861):345–352, 2001.

[31] K.D. Kreuer. On the development of proton conducting polymer membranes for hydrogen and methanol fuel cells. *Journal of Membrane Science*, 185(1):29–39, 2001.

[32] Subhash Singhal and Kevin Kendall. *High–temperature Solid Oxide Fuel Cells: Fundamentals, Design and Applications: Fundamentals, Design and Applications*. Elsevier, 2003.

[33] X. Li. *Principles of Fuel Cells*. Taylor & Francis Group, 2006.

[34] Nurettin Demirdöven and John Deutch. Hybrid cars now, fuel cell cars later. *Science*, 305(5686):974–976, 2004.

[35] Patrick Linke, Antonis Kokossis, and Alberto Alva-Argaez. Process intensification. *Computer Aided Process and Product Engineering (CAPE)*, 1, 2007.

[36] Andrzej Stankiewicz and Jacob A. Moulijn. Process intensification: transforming chemical engineering. *Chemical Engineering Progress*, pages 22–34, 2000.

[37] Andrzej Stankiewicz and Jacob A. Moulijn. Process intensification. *Industrial & Engineering Chemistry Research*, 41(8):1920–1924, 2002.

[38] David Reay, Colin Ramshaw, and Adam Harvey. *Process Intensification: Engineering for efficiency, sustainability and flexibility*. Butterworth-Heinemann, 2013.

[39] Nikola M. Nikačević, Adrie E.M. Huesman, Paul M.J. Van den Hof, and Andrzej I. Stankiewicz. Opportunities and challenges for process control in process intensification. *Chemical Engineering and Processing: Process Intensification*, 52:1–15, 2012.

[40] Jacob A Moulijn, Andrzej Stankiewicz, Johan Grievink, and Andrzej Górak. Process intensification and process systems engineering: a friendly symbiosis. *Computers & Chemical Engineering*, 32(1):3–11, 2008.

[41] Kari Alanne and Arto Saari. Sustainable small-scale CHP technologies for buildings: the basis for multi-perspective decision-making. *Renewable and Sustainable Energy Reviews*, 8(5):401–431, 2004.

[42] H.I. Onovwiona and V.I. Ugursal. Residential cogeneration systems: review of the current technology. *Renewable and Sustainable Energy Reviews*, 10(5):389–431, 2006.

[43] Reinhard Madlener and Christiane Schmid. Combined heat and power generation in liberalised markets and a carbon-constrained world. *GAIA-Ecological Perspectives for Science and Society*, 12(2):114–120, 2003.

[44] Pilar Lisbona, Alessandro Corradetti, Roberto Bove, and Piero Lunghi. Analysis of a solid oxide fuel cell system for combined heat and power applications under non-nominal conditions. *Electrochimica Acta*, 53(4):1920–1930, 2007.

[45] D.W. Wu and R.Z. Wang. Combined cooling, heating and power: A review. *Progress in Energy and Combustion Science*, 32(5):459–495, 2006.

[46] Guido Pepermans, Johan Driesen, Dries Haeseldonckx, Ronnie Belmans, and William Dhaeseleer. Distributed generation: definition, benefits and issues. *Energy Policy*, 33(6):787–798, 2005.

[47] Anne Hampson. Combined heat and power: Enabling resilient energy infrastructure for critical facilities. Technical Report ORNL/TM–2013/100, Oak Ridge National Laboratory (ORNL), March 2013.

[48] A.D. Hawkes, P. Aguiar, B. Croxford, M.A. Leach, C.S. Adjiman, and N.P. Brandon. Solid oxide fuel cell micro combined heat and power system operating strategy: Options for provision of residential space and water heating. *Journal of Power Sources*, 164(1):260–271, 2007.

[49] Erkko Fontell, Timo Kivisaari, N. Christiansen, J-B Hansen, and J. Pålsson. Conceptual study of a 250kW planar SOFC system for CHP application. *Journal of Power Sources*, 131(1):49–56, 2004.

[50] Gianfranco Chicco and Pierluigi Mancarella. Distributed multi-generation: a comprehensive view. *Renewable and Sustainable Energy Reviews*, 13(3):535–551, 2009.

[51] Residential Energy Consumption Survey U.S. Energy Information Administration. Heating and cooling no longer majority of U.S home energy use. http://www.eia.gov/todayinenergy/detail.cfm?id=10271&src=%E2%80%B9%20Consumption%20%20%20%20%20%20Residential%20Energy%20Consumption%20Survey%20(RECS)-b1. Accessed: 10-26-2013.

[52] Whitney Colella. Implications of electricity liberalization for combined heat and power (CHP) fuel cell systems (FCS): a case study of the United Kingdom. *Journal of Power Sources*, 106(1):397–404, 2002.

[53] Whitney Colella. Design options for achieving a rapidly variable heat-to-power ratio in a combined heat and power (CHP) fuel cell system (FCS). *Journal of Power Sources*, 106(1):388–396, 2002.

[54] Ernst Riensche, Josefin Meusinger, Ulrich Stimming, and Guido Unverzagt. Optimization of a 200 kW SOFC cogeneration power plant. part II: variation of the flowsheet. *Journal of Power Sources*, 71(1):306–314, 1998.

[55] R.J. Braun, S.A. Klein, and D.T. Reindl. Evaluation of system configurations for solid oxide fuel cell-based micro-combined heat and power generators in residential applications. *Journal of Power Sources*, 158(2):1290–1305, 2006.

[56] Tae Seok Lee, J.N. Chung, and Yen-Cho Chen. Design and optimization of a combined fuel reforming and solid oxide fuel cell system with anode off-gas recycling. *Energy Conversion and Management*, 52(10):3214–3226, 2011.

[57] Shiying Lin, Michiaki Harada, Yoshizo Suzuki, and Hiroyuki Hatano. Hydrogen production from coal by separating carbon dioxide during gasification. *Fuel*, 81(16):2079–2085, 2002.

[58] Jens R Rostrup-Nielsen. Production of synthesis gas. *Catalysis today*, 18(4):305–324, 1993.

[59] A. Boudghene Stambouli and E. Traversa. Solid oxide fuel cells (SOFCs): a review of an environmentally clean and efficient source of energy. *Renewable and Sustainable Energy Reviews*, 6(5):433–455, 2002.

[60] Andrew L. Dicks. Hydrogen generation from natural gas for the fuel cell systems of tomorrow. *Journal of Power Sources*, 61(1):113–124, 1996.

[61] P. Aguiar, D. Chadwick, and L. Kershenbaum. Modelling of an indirect internal reforming solid oxide fuel cell. *Chemical Engineering Science*, 57(10):1665–1677, 2002.

[62] Khaliq Ahmed and Karl Foger. Kinetics of internal steam reforming of methane on ni/ysz-based anodes for solid oxide fuel cells. *Catalysis Today*, 63(2):479–487, 2000.

[63] Caine M. Finnerty, Neil J. Coe, Robert H. Cunningham, and R. Mark Ormerod. Carbon formation on and deactivation of nickel-based/zirconia anodes in solid oxide fuel cells running on methane. *Catalysis Today*, 46(2):137–145, 1998.

[64] Vinod M. Janardhanan and Olaf Deutschmann. CFD analysis of a solid oxide fuel cell with internal reforming: Coupled interactions of transport, heterogeneous catalysis and electrochemical processes. *Journal of Power Sources*, 162(2):1192–1202, 2006.

[65] S. Campanari and P. Iora. Definition and sensitivity analysis of a finite volume SOFC model for a tubular cell geometry. *Journal of Power Sources*, 132(1):113–126, 2004.

[66] Mona Bavarian and Masoud Soroush. Steady–state multiplicity in a solid oxide fuel cell: Practical considerations. *Chemical Engineering Science*, 67(1):2–14, 2012.

[67] W. Lehnert, J. Meusinger, and F. Thom. Modelling of gas transport phenomena in SOFC anodes. *Journal of Power Sources*, 87(1):57–63, 2000.

[68] Thinh X. Ho, Pawel Kosinski, Alex C. Hoffmann, and Arild Vik. Numerical analysis of a planar anode-supported SOFC with composite electrodes. *International Journal of Hydrogen Energy*, 34(8):3488–3499, 2009.

[69] Ryan P O'Hayre, Suk-Won Cha, Whitney Colella, and Fritz B Prinz. *Fuel cell fundamentals*. John Wiley & Sons New York, 2006.

[70] Zuo Chendong, Liu Mingfei, and Liu Meilin. Chapter 2: Solid oxide fuel cells. In Mario Aparicio, Andrei Jitianu, and Lisa C Klein, editors, *Sol-Gel processing for conventional and alternative energy*, Advances in Sol-Gel Derived Materials and Technologies, pages 7–35. Springer, 2012.

[71] JPP Huijsmans, FPF Van Berkel, and GM Christie. Intermediate temperature SOFC–a promise for the 21st century. *Journal of Power Sources*, 71(1):107–110, 1998.

[72] R Mark Ormerod. Solid oxide fuel cells. *Chemical Society Reviews*, 32(1):17–28, 2003.

[73] Vincenzo Liso, Anders Christian Olesen, Mads Pagh Nielsen, and Søren Knudsen Kær. Performance comparison between partial oxidation and methane steam reforming processes for solid oxide fuel cell (SOFC) micro combined heat and power (CHP) system. *Energy*, 36(7):4216–4226, 2011.

[74] Michael Baldea and Prodromos Daoutidis. Dynamics and control of autothermal reactors for the production of hydrogen. *Chemical Engineering Science*, 62(12):3218–3230, 2007.

[75] Seungdoo Park, John M Vohs, and Raymond J Gorte. Direct oxidation of hydrocarbons in a solid-oxide fuel cell. *Nature*, 404(6775):265–267, 2000.

[76] S McIntosh, JM Vohs, and RJ Gorte. Role of hydrocarbon deposits in the enhanced performance of direct-oxidation SOFCs. *Journal of The Electrochemical Society*, 150(4):470–476, 2003.

[77] E Perry Murray, T Tsai, and SA Barnett. A direct-methane fuel cell with a ceria-based anode. *Nature*, 400(6745):649–651, 1999.

[78] Steven McIntosh and Raymond J Gorte. Direct hydrocarbon solid oxide fuel cells. *Chemical Reviews*, 104(10):4845–4866, 2004.

[79] Alan Atkinson, S Barnett, Raymond J Gorte, JTS Irvine, Augustin J McEvoy, Mogens Mogensen, Subhash C Singhal, and J Vohs. Advanced anodes for high-temperature fuel cells. *Nature materials*, 3(1):17–27, 2004.

[80] Dimitrios Georgis, Sujit S Jogwar, Ali S Almansoori, and Prodromos Daoutidis. Impact of steam reformer on the design and control of an energy integrated solid oxide fuel cell system. In *19th Mediterranean Conference on Control & Automation (MED)*, pages 576–581. IEEE, 2011.

[81] Subbarao Varigonda and Mithun Kamat. Control of stationary and transportation fuel cell systems: Progress and opportunities. *Computers & Chemical Engineering*, 30(10-12):1735–1748, 2006.

[82] Jay T. Pukrushpan, Anna G. Stefanopoulou, and Huei Peng. *Control of fuel cell power systems: principles, modeling, analysis, and feedback design*. Springer Verlag, 2004.

[83] D.L. Cresswell and I.S. Metcalfe. Energy integration strategies for solid oxide fuel cell systems. *Solid State Ionics*, 177(19-25):1905–1910, 2006.

[84] R.J. Kee, H. Zhu, A.M. Sukeshini, and G.S. Jackson. Solid oxide fuel cells: Operating principles, current challenges, and the role of syngas. *Combustion Science and Technology*, 180(6):1207–1244, 2008.

[85] Debangsu Bhattacharyya and Raghunathan Rengaswamy. A review of solid oxide fuel cell (SOFC) dynamic models. *Industrial & Engineering Chemistry Research*, 48(13):6068–6086, 2009.

[86] Mona Bavarian, Masoud Soroush, Ioannis G. Kevrekidis, and Jay B. Benziger. Mathematical Modeling, Steady-State and Dynamic Behavior, and Control of Fuel Cells: A Review. *Industrial & Engineering Chemistry Research*, 49(17):7922–7950, 2010.

[87] A. Chaisantikulwat, C. Diaz-Goano, and E.S. Meadows. Dynamic modelling and control of planar anode-supported solid oxide fuel cell. *Computers & Chemical Engineering*, 32(10):2365–2381, 2008.

[88] A.K.M. Murshed, Biao Huang, and Kumar Nandakumar. Control relevant modeling of planer solid oxide fuel cell system. *Journal of Power Sources*, 163(2):830–845, 2007.

[89] Thomas A. Adams II and Paul I. Barton. High-efficiency power production from natural gas with carbon capture. *Journal of Power Sources*, 195(7):1971–1983, 2010.

[90] Fabian Mueller, Faryar Jabbari, Robert Gaynor, and Jacob Brouwer. Novel solid oxide fuel cell system controller for rapid load following. *Journal of Power Sources*, 172(1):308–323, 2007.

[91] Ayman M. Al-Qattan and Donald J. Chmielewski. Distributed feed design for SOFCs with internal reforming. *Journal of the Electrochemical Society*, 151:A1891, 2004.

[92] Xiongwen Zhang, S.H. Chan, Guojun Li, H.K. Ho, Jun Li, and Zhenping Feng. A review of integration strategies for solid oxide fuel cells. *Journal of Power Sources*, 195(3):685–702, 2010.

[93] S.H. Chan, H.K. Ho, and Y. Tian. Modelling of simple hybrid solid oxide fuel cell and gas turbine power plant. *Journal of Power Sources*, 109(1):111–120, 2002.

[94] Xiongwen Zhang, Jun Li, Guojun Li, and Zhenping Feng. Dynamic modeling of a hybrid system of the solid oxide fuel cell and recuperative gas turbine. *Journal of Power Sources*, 163(1):523–531, 2006.

[95] M. Cali, M.G.L. Santarelli, and P. Leone. Computer experimental analysis of the CHP performance of a 100 kWe SOFC Field Unit by a factorial design. *Journal of Power Sources*, 156(2):400–413, 2006.

[96] Yaofan Yi, Ashok D. Rao, Jacob Brouwer, and G. Scott Samuelsen. Fuel flexibility study of an integrated 25kW SOFC reformer system. *Journal of power sources*, 144(1):67–76, 2005.

[97] R. Kandepu, L. Imsland, B.A. Foss, C. Stiller, B. Thorud, and O. Bolland. Modeling and control of a SOFC-GT-based autonomous power system. *Energy*, 32(4):406–417, 2007.

[98] Fabian Mueller, Robert Gaynor, Allie E. Auld, Jacob Brouwer, Faryar Jabbari, and G. Scott Samuelsen. Synergistic integration of a gas turbine and solid oxide fuel cell for improved transient capability. *Journal of Power Sources*, 176(1):229–239, 2008.

[99] S.R. Oh and J. Sun. Optimization and load-following characteristics of 5kw-class tubular solid oxide fuel cell/gas turbine hybrid systems. In *American Control Conference (ACC), 2010*, pages 417–422. IEEE, 2010.

[100] P. Varbanov and J. Klemes. Analysis and integration of fuel cell combined cycles for development of low-carbon energy technologies. *Energy*, 33(10):1508–1517, 2008.

[101] Jhuma Sadhukhan, Yingru Zhao, Matthew Leach, Nigel P Brandon, and Nilay Shah. Energy integration and analysis of solid oxide fuel cell based microcombined heat and power systems and other renewable systems using biomass waste derived syngas. *Industrial & Engineering Chemistry Research*, 49(22):11506–11516, 2010.

[102] D.J. Bents. High temperature solid oxide regenerative fuel cell for solar photovoltaic energy storage. In *Proceedings of the 22nd Intersociety Energy Conversion Engineering Conference*, pages 808–817. AIAA, 1987.

[103] C.H. Hamann, A. Hamnett, and W. Vielstich. *Electrochemistry*. Weinheim: Wiley-VCH, 2007.

[104] C. Wang and M.H. Nehrir. A physically based dynamic model for solid oxide fuel cells. *IEEE Transactions on Energy Conversion*, 22(4):887–897, 2007.

[105] J.R. Ferguson, J.M. Fiard, and R. Herbin. Three-dimensional numerical simulation for various geometries of solid oxide fuel cells. *Journal of Power Sources*, 58(2):109–122, 1996.

[106] Handa Xi, Subbarao Varigonda, and Buyun Jing. Dynamic modeling of a Solid Oxide Fuel Cell system for control design. In *American Control Conference (ACC), 2010*, pages 423–428. IEEE, 2010.

[107] M. Sorrentino, C. Pianese, and Y.G. Guezennec. A hierarchical modeling approach to the simulation and control of planar solid oxide fuel cells. *Journal of Power Sources*, 180(1):380–392, 2008.

[108] J. Xu and G.F. Froment. Methane steam reforming, methanation and water-gas shift: I. Intrinsic kinetics. *AIChE Journal*, 35(1):88–96, 1989.

[109] B. Linnhoff and E. Hindmarsh. The pinch design method for heat exchanger networks. *Chemical Engineering Science*, 38(5):745–763, 1983.

[110] Ian C. Kemp. *Pinch analysis and process integration: a user guide on process integration for the efficient use of energy*. Butterworth-Heinemann, 2007.

[111] William L. Luyben. *Process modeling, simulation, and control for chemical engineers*. McGraw-Hill New York, 1990.

[112] Reyyan Koc, Nikolaos K. Kazantzis, William J. Nuttall, and Yi Hua Ma. Economic assessment of inherently safe membrane reactor technology options integrated into IGCC power plants . *Process Safety and Environmental Protection*, 90(5):436 – 450, 2012.

[113] C. Descamps, C. Bouallou, and M. Kanniche. Efficiency of an integrated gasification combined cycle (IGCC) power plant including CO_2 removal. *Energy*, 33(6):874 – 881, 2008.

[114] Kendell R. Jillson, Vishnu Chapalamadugu, and B. Erik Ydstie. Inventory and flow control of the IGCC process with CO_2 recycles. *Journal of Process Control*, 19(9):1470 – 1485, 2009.

[115] F. Emun, M. Gadalla, T. Majozi, and D. Boer. Integrated gasification combined cycle (IGCC) process simulation and optimization. *Computers & Chemical Engineering*, 34(3):331–338, 2010.

[116] Thomas A Adams II and Paul I Barton. High-efficiency power production from natural gas with carbon capture. *Journal of Power Sources*, 195(7):1971–1983, 2010.

[117] Fabian Mueller, Faryar Jabbari, and Jacob Brouwer. On the intrinsic transient capability and limitations of solid oxide fuel cell systems. *Journal of Power Sources*, 187(2):452–460, 2009.

[118] W.L. Becker, R.J. Braun, M. Penev, and M. Melaina. Design and technoeconomic performance analysis of a 1MW solid oxide fuel cell polygeneration system for combined production of heat, hydrogen, and power. *Journal of Power Sources*, 200(0):34 – 44, 2012.

[119] Thomas A Adams II and Paul I Barton. Combining coal gasification, natural gas reforming, and solid oxide fuel cells for efficient polygeneration with CO_2 capture and sequestration. *Fuel Processing Technology*, 92(10):2105 – 2115, 2011.

[120] Mu Li, Jacob Brouwer, Ashok D Rao, and G Scott Samuelsen. Application of a detailed dimensional solid oxide fuel cell model in integrated gasification fuel cell system design and analysis. *Journal of Power Sources*, 196(14):5903–5912, 2011.

[121] Thomas A Adams II and Paul I Barton. A dynamic two–dimensional heterogeneous model for water gas shift reactors. *International Journal of Hydrogen Energy*, 34(21):8877–8891, 2009.

[122] Jose D. Figueroa, Timothy Fout, Sean Plasynski, Howard McIlvried, and Rameshwar D. Srivastava. Advances in CO_2 capture technology–the U.S. Department of Energy's Carbon Sequestration Program. *International Journal of Greenhouse Gas Control*, 2(1):9 – 20, 2008.

[123] TE Rufford, S Smart, GCY Watson, BF Graham, J Boxall, JC Diniz da Costa, and EF May. The removal of CO_2 and N_2 from natural gas: A review of conventional and emerging process technologies. *Journal of Petroleum Science and Engineering*, 94–95(0):123–154, 2012.

[124] M. De Falco, L. Di Paola, L. Marrelli, and P. Nardella. Simulation of large-scale membrane reformers by a two-dimensional model. *Chemical Engineering Journal*, 128(2):115–125, 2007.

[125] Rune Bredesen, Kristin Jordal, and Olav Bolland. High-temperature membranes in power generation with co_2 capture. *Chemical Engineering and Processing: Process Intensification*, 43(9):1129–1158, 2004.

[126] Mitra Abdollahi, Jiang Yu, Paul K.T. Liu, Richard Ciora, Muhammad Sahimi, and Theodore T. Tsotsis. Ultra-pure hydrogen production from reformate mixtures using a palladium membrane reactor system. *Journal of Membrane Science*, 390:32–42, 2012.

[127] Reyyan Koc, Nikolaos K Kazantzis, and Yi Hua Ma. Process safety aspects in water-gas-shift (WGS) membrane reactors used for pure hydrogen production. *Journal of Loss Prevention in the Process Industries*, 24(6):852–869, 2011.

[128] Sungwon Hwang and Robin Smith. Heterogeneous catalytic reactor design with optimum temperature profile I: application of catalyst dilution and side-stream distribution. *Chemical Engineering Science*, 59(20):4229–4243, 2004.

[129] T.P. Tiemersma, C.S. Patil, M van Sint Annaland, and J.A.M Kuipers. Modelling of packed bed membrane reactors for autothermal production of ultrapure hydrogen. *Chemical Engineering Science*, 61(5):1602–1616, 2006.

[130] Fausto Gallucci, Ekain Fernandez, Pablo Corengia, and Martin van Sint Annaland. Recent advances on membranes and membrane reactors for hydrogen production. *Chemical Engineering Science*, 92(0):40–66, 2013.

[131] Panagiotis Boutikos and Vladimiros Nikolakis. A simulation study of the effect of operating and design parameters on the performance of a water gas shift membrane reactor. *Journal of Membrane Science*, 350(1):378–386, 2010.

[132] Krzysztof Gosiewski and Marek Tańczyk. Applicability of membrane reactor for WGS coal derived gas processing: Simulation–based analysis. *Catalysis Today*, 176(1):373–382, 2011.

[133] Giovanni Chiappetta, Gabriele Clarizia, and Enrico Drioli. Theoretical analysis of the effect of catalyst mass distribution and operation parameters on the performance of a Pd–based membrane reactor for water–gas shift reaction. *Chemical Engineering Journal*, 136(2):373–382, 2008.

[134] Vincenzo Piemonte, Marcello De Falco, Barbara Favetta, and Angelo Basile. Counter-current membrane reactor for WGS process: Membrane design. *International Journal of Hydrogen Energy*, 35(22):12609–12617, 2010.

[135] María E Adrover, Eduardo López, Daniel O Borio, and Marisa N Pedernera. Theoretical study of a membrane reactor for the water gas shift reaction under nonisothermal conditions. *AIChE Journal*, 55(12):3206–3213, 2009.

[136] Fernando V Lima, Prodromos Daoutidis, Michael Tsapatsis, and John J Marano. Modeling and optimization of membrane reactors for carbon capture in integrated gasification combined cycle units. *Industrial & Engineering Chemistry Research*, 51(15):5480–5489, 2012.

[137] Adele Brunetti, Enrico Drioli, and Giuseppe Barbieri. Medium/high temperature water gas shift reaction in a Pd–Ag membrane reactor: an experimental investigation. *RSC Advances*, 2(1):226–233, 2012.

[138] Nathan W. Ockwig and Tina M. Nenoff. Membranes for hydrogen separation. *Chemical Reviews*, 107(10):4078–4110, 2007.

[139] Shengchun Yan, Hideaki Maeda, Katsuki Kusakabe, and Shigeharu Morooka. Thin palladium membrane formed in support pores by metal–organic chemical vapor deposition method and application to hydrogen separation. *Industrial & Engineering Chemistry Research*, 33(3):616–622, 1994.

[140] Mario Amelio, Pietropaolo Morrone, Fausto Gallucci, and Angelo Basile. Integrated gasification gas combined cycle plant with membrane reactors: Technological and economical analysis. *Energy Conversion and Management*, 48(10):2680–2693, 2007.

[141] M Bracht, PT Alderliesten, R Kloster, R Pruschek, G Haupt, E Xue, JRH Ross, MK Koukou, and N Papayannakos. Water gas shift membrane reactor for CO_2 control in IGCC systems: techno–economic feasibility study. *Energy Conversion and Management*, 38:S159–S164, 1997.

[142] Sina Rezvani, Ye Huang, David McIlveen-Wright, Neil Hewitt, and Jayanta Deb Mondol. Comparative assessment of coal fired igcc systems with CO_2 capture using physical absorption, membrane reactors and chemical looping. *Fuel*, 88(12):2463–2472, 2009.

[143] P Piroonlerkgul, W Kiatkittipong, A Arpornwichanop, A Soottitantawat, W Wiyaratn, N Laosiripojana, AA Adesina, and S Assabumrungrat. Integration of solid oxide fuel cell and palladium membrane reactor: Technical and economic analysis. *International Journal of Hydrogen Energy*, 34(9):3894–3907, 2009.

[144] K. Babita, S. Sridhar, and K.V. Raghavan. Membrane reactors for fuel cell quality hydrogen through WGSR–Review of their status, challenges and opportunities. *International Journal of Hydrogen Energy*, 36(11):6671–6688, 2011.

[145] James R Lattner and Michael P Harold. Comparison of conventional and membrane reactor fuel processors for hydrocarbon–based PEM fuel cell systems. *International Journal of Hydrogen Energy*, 29(4):393–417, 2004.

[146] W Yu, T Ohmori, T Yamamoto, A Endo, M Nakaiwa, T Hayakawa, and N Itoh. Simulation of a porous ceramic membrane reactor for hydrogen production. *International Journal of Hydrogen Energy*, 30(10):1071–1079, 2005.

[147] Alessio Caravella, Francesco Paolo Di Maio, and Alberto Di Renzo. Optimization of membrane area and catalyst distribution in a permeative–stage membrane reactor for methane steam reforming. *Journal of Membrane Science*, 321(2):209–221, 2008.

[148] James R. Lattner and Michael P. Harold. Autothermal reforming of methanol: experiments and modeling. *Catalysis Today*, 120(1):78–89, 2007.

[149] A. Brunetti, A. Caravella, G. Barbieri, and E. Drioli. Simulation study of water gas shift reaction in a membrane reactor. *Journal of Membrane Science*, 306(1):329–340, 2007.

[150] Iasson Karafyllis and Prodromos Daoutidis. Control of hot spots in plug flow reactors. *Computers & Chemical Engineering*, 26(7):1087–1094, 2002.

[151] PSE. *IPPFO–Ideal Physical Properties Foreign Object*, 3.6 edition, October 2012.

[152] Panagiotis D Christofides and Prodromos Daoutidis. Feedback control of hyperbolic PDE systems. *AIChE Journal*, 42(11):3063–3086, 1996.

[153] Eric D Wachsman, Craig A Marlowe, and Kang Taek Lee. Role of solid oxide fuel cells in a balanced energy strategy. *Energy & Environmental Science*, 5(2):5498–5509, 2012.

[154] Lawrence Kar Chung Tse, Steven Wilkins, Niall McGlashan, Bernhard Urban, and Ricardo Martinez-Botas. Solid oxide fuel cell/gas turbine trigeneration system for marine applications. *Journal of Power Sources*, 196(6):3149–3162, 2011.

[155] Mehdi Hosseini, Ibrahim Dincer, and Marc A. Rosen. Hybrid solarfuel cell combined heat and power systems for residential applications: Energy and exergy analyses. *Journal of Power Sources*, 221(0):372 – 380, 2013.

[156] J Deng, RZ Wang, and GY Han. A review of thermally activated cooling technologies for combined cooling, heating and power systems. *Progress in Energy and Combustion Science*, 37(2):172–203, 2011.

[157] Zeting Yu, Jitian Han, Xianqi Cao, Wei Chen, and Bin Zhang. Analysis of total energy system based on solid oxide fuel cell for combined cooling and power applications. *International Journal of Hydrogen Energy*, 35(7):2703–2707, 2010.

[158] Zeting Yu, Jitian Han, and Xianqi Cao. Investigation on performance of an integrated solid oxide fuel cell and absorption chiller tri-generation system. *International Journal of Hydrogen Energy*, 36(19):12561–12573, 2011.

[159] Robert Joseph Braun. *Optimal design and operation of solid oxide fuel cell systems for small-scale stationary applications*. PhD thesis, University of Wisconsin–Madison, 2002.

[160] Junxi Jia, Qiang Li, Ming Luo, Liming Wei, and Abuliti Abudula. Effects of gas recycle on performance of solid oxide fuel cell power systems. *Energy*, 36(2):1068–1075, 2011.

[161] Mike Powell, Kerry Meinhardt, Vince Sprenkle, Larry Chick, and Gary McVay. Demonstration of a highly efficient solid oxide fuel cell power system using adiabatic steam reforming and anode gas recirculation. *Journal of Power Sources*, 205:377–384, 2012.

[162] Kasra Nikooyeh, Ayodeji A Jeje, and Josephine M Hill. 3D modeling of anode-supported planar SOFC with internal reforming of methane. *Journal of Power Sources*, 171(2):601–609, 2007.

[163] Timo Kivisaari, Pehr Björnbom, Christopher Sylwan, Bernard Jacquinot, Daniel Jansen, and Arend de Groot. The feasibility of a coal gasifier combined with a high-temperature fuel cell. *Chemical Engineering Journal*, 100(1):167–180, 2004.

[164] Valérie Eveloy. Numerical analysis of an internal methane reforming solid oxide fuel cell with fuel recycling. *Applied Energy*, 93:107–115, 2012.

[165] Ralph-Uwe Dietrich, Jana Oelze, Andreas Lindermeir, Christian Spitta, Michael Steffen, Torben Küster, Shaofei Chen, Christian Schlitzberger, and Reinhard Leithner. Efficiency gain of solid oxide fuel cell systems by using anode offgas recycle–Results for a small scale propane driven unit. *Journal of Power Sources*, 196(17):7152–7160, 2011.

[166] Richard Fellows. A novel configuration for direct internal reforming stacks. *Journal of Power Sources*, 71(1-2):281–287, 1998.

[167] AL Dicks. Advances in catalysts for internal reforming in high temperature fuel cells. *Journal of power Sources*, 71(1-2):111–122, 1998.

[168] Patricia Aguiar, CS Adjiman, and Nigel P Brandon. Anode-supported intermediate temperature direct internal reforming solid oxide fuel cell. I: model-based steady-state performance. *Journal of Power Sources*, 138(1):120–136, 2004.

[169] PSE. *Optimization Guide*, 3.6 edition, October 2012.

[170] Robert J. Braun, Tyrone L. Vincent, Huayang Zhu, and Robert J. Kee. Chapter 7: Analysis, optimization, and control of solid-oxide fuel cell systems. In Kai Sundmacher, editor, *Fuel Cell Engineering*, volume 41 of *Advances in Chemical Engineering*, pages 383–446. Academic Press, 2012.